

Microfluidic and micromechanical in vivo studies of *Caenorhabditis elegans*

Thèse N° 7237

Présentée le 31 juillet 2019

à la Faculté des sciences et techniques de l'ingénieur
Laboratoire de microsystemes 2
Programme doctoral en microsystemes et microélectronique

pour l'obtention du grade de Docteur ès Sciences

par

Roger Philippe KRENGER

Acceptée sur proposition du jury

Dr G. Boero, président du jury
Prof. M. Gijs, Dr T. Lehnert, directeurs de thèse
Prof. B. Nelson, rapporteur
Prof. C. Ewald, rapporteur
Prof. D. Pioletti, rapporteur

2019

Acknowledgements

I would like to express my sincere gratitude to everyone who has contributed to my thesis. This work would not have been possible without any of you.

First and foremost, I would like to show my appreciation for Martin Gijs, my thesis supervisor and mentor, for giving me the opportunity to do research in his group. Martin never doubted my abilities to finish this project, and he was always available if I needed help or guidance. He always listened very carefully to what I had to say and did everything in his power to support my journey, while always treating me with great respect. He is an expert thesis director, knowing exactly when to leave me freedom to pursue my own ideas and when to bring me back on track if I deviate too much from the thesis objectives. I enjoyed this freedom a lot, and working independently allowed me to grow as a person. Martin, thank you very much.

In the same way, I would like to thank my thesis co-advisor Thomas Lehnert, who always was available for discussions and advice that would bring clarity in what I needed to do next. His thorough revision of my manuscripts and suggestions for improvement enhanced the quality of my work tremendously.

I am grateful to Collin Ewald, Dominique Pioletti and Bradley Nelson for evaluating my thesis and their precious feedbacks, and to Giovanni Boero for accepting the duty as jury president. Danke vielmol Melis and merci beaucoup Lucie for your help with administrative issues and your support from the first day.

Moreover, I appreciated the technical support I received from the EPFL Center of MicroNanoTechnology and the EPFL Atelier de l'Institut de microtechnique. The specialists of both organisations were always available to give trainings, to offer advice or to provide practical help on very short notice. I could not have designed my devices without their input.

One of the richest aspects in my time as a PhD student was the possibility to exchange with people from every corner of the planet. Within our research group, I was able to find the most extraordinary group of friends I ever had and to learn about cultures previously unknown to me. Due to the nature of PhD studies, the people I met in the group at my arrival eventually all finished their projects before me and eventually left the group: Gergely, thank you for showing me around EPFL, inviting me to lunch on my first day (and then $\approx 1000\times$ more over the years), and for being the most trustworthy officemate I could imagine. Contrary to your belief, I consider you my friend for a long time already. Rima, thank you for your help when I started my PhD and you ended yours. Thank you Cristina for brightening up my days in tough

Acknowledgements

times. Axel, I am glad that you brought a little bit of Basel to LMIS2. Li, thanks for the most extraordinary tour of Washington, D.C. I could have never planned myself. Raphaël, thank you for your scientific input and for your quiet aura that calmed me down in a way that I cannot phrase. Tuan, the brilliant and confused genius always brought a smile on my face. I still own the mini-skateboard you left for me here. I will gift it forward soon.

Matteo, Xiaopeng and Jalil were the constants during my time at LMIS2. I am glad to see Nagibio grow, and Xiaopeng getting closer to his ambitious goals. I was always glad to teach under Jalil's supervision, thanks for giving me a challenging but fun opportunity.

On the other side, for every departure, there was an arrival bringing something new to the group: Muaz and Farzad, I wish you only the best for your PhD studies. Vittorio, the end of the tunnel is near. Keep rocking. Yang, I thank you for your input and the tricks you taught me to make life easier around the lab, and for valuable discussions in our joined project. I thank Fabien, the expert for Swiss precision engineering, for all advice he gave me. Thanks to Maël and Alix, the most recent bunch of smart and curious students for rich, fun exchanges during work and chill times. Thanks Daniel, it was a blast sharing the office with you, even though I will probably never beat your (incredibly lucky) office-basketball scoring streak. And of course Baris, my anchor in the group and much more than just chill-break buddy, thank you for everything.

A gigantic thank you also to Jan, my friend for more than 10 years and my favourite collaborator I ever had. This foolish idea we once had to poke microscopic worms turned into a nice study after all. Thank you for your friendship and help, not just during our collaborations.

Albert and Hermeto, I am glad that you introduced me to running. This has changed my life. Thank you for all the longruns and climbing sessions together, in good and bad weather, many of them followed by a drink to directly negate the healthy benefit of the activity. Awesome. I will never forget the marathon we ran together. I'd rather forget the Delirium, though.

Most importantly, I am endlessly grateful for my now suddenly very large family. Thank you to my parents Carmen and Fredy, to my sister Simone and to my grandparents for your constant support and for constantly believing in me. Thank you Ali and Gina for providing shelter in Lausanne and your infinite generosity. You made my stay in Lausanne truly enjoyable. Thanks to my young swarm of nephews Kendal, Toni and Colin and my niece Leonora for hours of laughter and already surprisingly exhausting football matches. You have a bright future ahead and I am looking forward to see you grow.

Jenny, I owe you my deepest gratitude. You were always there for me whenever I needed help, a boost of motivation or companionship. I admire your enthusiasm, optimistic attitude towards everything and your frequent little history lessons, even at the most peculiar times. You even organized my personal fan club to help me go through the last stages of my PhD! Wow. I cannot describe how much you mean to me.

Lausanne, July 2019

Roger Krenger

Abstract

Caenorhabditis elegans (*C. elegans*) is one of the most attractive model organisms in biomedical research for understanding human diseases and for drug testing at a whole-organism level, since many biological pathways and genes have been conserved between itself and humans. The nematode is sufficiently complex so that complex biological questions can be addressed, yet the organism is still simple enough to be used in high-content *in vivo* assays. In this work, we present new microfluidic and MEMS-based tools enabling the characterization of *C. elegans* worms and embryos *in vivo*. Since mitochondrial dysfunction is related to many diseases including metabolic disorders and aging-related conditions, our main focus was on metabolic assays of *C. elegans* worms in larval and adult stages. Mitochondrial functioning can be quantified by means of metabolic heat production and oxygen uptake, two key phenotypes for assessing mitochondrial respiration. The *C. elegans* embryo may be used for interesting biological studies too, *e.g.* developmental assays. In the frame of this work, we investigated the mechanical properties of the *C. elegans* embryonic eggshell.

In a first part of this thesis, we measured the metabolic heat production of small *C. elegans* larval populations. Heat production, which can be measured by direct calorimetry, is a phenotype that allows assessing the metabolic activity of living organisms. We developed a nanocalorimetric system that is based on microfabricated thermopile sensors which are integrated with poly(dimethylsiloxane) (PDMS) microfluidic chips. In addition to versatile fluidic manipulation of samples on-chip, our microfluidic approach allows confining worm populations close to the Si sensor surface, thus enabling high sensitivity of the assays. Our results indicate an increase of the heat production per worm body volume from the L2 to the L3 larval stages, and a significant decrease from the L3 to the L4 stages. Additionally, we investigated the metabolic heat production of the larval populations during maximal respiratory capacity, *i.e.* after inducing *uncoupled respiration* by on-chip treatment with a mitochondrial uncoupling agent. Depending on the larval stage, inducing *uncoupled respiration* causes an increase of the metabolic heat production ranging from 55% up to 95% with respect to untreated worms. Our experiments demonstrated that nanocalorimetry is a direct and highly-sensitive technique that can be combined with other analytical methods to open the way to a more holistic understanding of fundamental biological processes.

Abstract

In a second study, we present a new microfluidic worm culture system with integrated luminescence-based sensing of the on-chip oxygen concentration for measuring the oxygen uptake of *C. elegans* worms. The microfluidic chip was fabricated in off-stoichiometry dual-cure thiol-ene-epoxy (OSTE+) to allow reliable measurement of the dissolved oxygen and the fabrication of high-resolution microstructures down to the μm -range. Our microfluidic approach allows confining a single nematode from the L4 stage in a culture chamber over a time span of up to 7 days. An automated protocol for feeding and for performing oxygen consumption rate (OCR) measurements during the worm development was applied. We found an increase of OCR values from the L4 stage to the adult worm, and a continuous decrease as the worm ages. In addition, we performed a *C. elegans* metabolic assay using a mitochondrial uncoupling agent, which increased OCR by a factor of ≈ 2 when compared to basal respiration rates. Treatment with sodium azide inhibited mitochondrial respiration and returned OCR values to zero.

In a third study, we developed a new method to study the mechanical properties of the *C. elegans* embryonic eggshell. During embryogenesis, assays focusing on emerging biological phenomena in an animal's life can be performed. However, while the *C. elegans* embryo has been extensively studied, its biomechanical properties are largely unknown. This is surprising, since one of the most important functions of the embryonic eggshell is to physically support and to protect the developing embryo from external cues. In our work, we use cellular force microscopy (CFM), a technique that combines micro-indentation with high-resolution force sensing approaching that of atomic force microscopy, in order to quantitatively study the mechanical properties of the eggshell of living *C. elegans* embryos. In addition, we demonstrate the capability of the system to detect alterations of mechanical shell parameters and shell defects upon chemical treatment, *i.e.* exposure to sodium hypochlorite and/or chitinase solutions, which selectively modify the multilayer eggshell structure. By this means, we evaluate the impact of the different layers on the mechanical integrity of the embryo. Finite element method simulations based on a simple embryo model were used to extract characteristic eggshell parameters from the experimental micro-indentation force-displacement curves. We found a strong correlation between the severity of the chemical treatment and the rigidity of the shell. Furthermore, our results showed, in contrast to previous assumptions, that short bleach treatments not only selectively remove the outermost vitelline layer of the eggshell, but also significantly deteriorate the underlying chitin layer, which is primarily responsible for the mechanical stability of the egg. Accurate sensing of changes in the embryo's mechanical integrity possibly enables more advanced embryo assays in view of correlating mechanical properties with other phenotypic or genetic parameters.

Keywords: *Caenorhabditis elegans*, embryo, larvae, microfluidic culture chips, nanocalorimetry, metabolic rate, metabolic heat production, oxygen consumption rate, mitochondrial uncoupling, microfluidics, microfabrication, cellular force microscopy, embryonic eggshell, mechanical properties.

Zusammenfassung

Caenorhabditis elegans (*C. elegans*) ist einer der attraktivsten Modellorganismen der Biochemie für die Erforschung von menschlichen Erkrankungen und für das Entdecken von Wirkstoffen für deren Bekämpfung. Viele Wirkungsmechanismen von Krankheiten und sonstige biologische Signalwege stimmen zwischen ihm und dem Menschen überein. Der Nematode ist komplex genug, sodass komplexe biologische Fragestellungen beantwortet werden können, und trotzdem simpel genug für effiziente Analysen am gesamten Organismus. Im Rahmen dieser Arbeit präsentieren wir neue Mikrosysteme für die Charakterisierung von lebenden *C. elegans* Nematoden und Embryos. Weil mitochondriale Störungen mit vielen metabolischen Erkrankungen und altersbedingten Symptomen zusammenhängen lag unser Schwerpunkt auf metabolischen Studien an Larven und ausgewachsenen Nematoden. Mitochondriale Funktion kann anhand von zwei typischen Phänotypen der mitochondrialen Atmung quantifiziert werden: der stoffwechselbedingten Wärmeerzeugung oder der Sauerstoffaufnahme. Der *C. elegans* Embryo kann ebenfalls für interessante biologische Studien verwendet werden. In dieser Arbeit untersuchten wir die mechanischen Eigenschaften seiner embryonalen Eierschale.

In einem ersten Teil dieser These analysierten wir die Erzeugung von Körperwärme einer kleinen Zahl von *C. elegans* Larven. Metabolische Wärmeerzeugung kann mit Hilfe von direkter Kalorimetrie gemessen werden und erlaubt das Untersuchen der Stoffwechselaktivität lebender Organismen. Wir entwickelten ein auf Thermosäulen basierendes kalorimetrisches System mit integrierten Polydimethylsiloxan (PDMS) mikrofluidischen Chips. Unser mikrofluidischer Ansatz erlaubt die vielseitige Handhabung der Samples on-chip und die gleichzeitige Einschliessung von Nematoden in der Nähe der Sensormembran, was zu hoher Messgenauigkeit führt. Unsere Resultate deuten auf einen Anstieg der volumenspezifischen Wärmeerzeugung vom Larvenstadium L2 zu L3, und eine Verringerung von L3 zu L4. Darüber hinaus untersuchten wir die maximale Wärmeerzeugung der Nematoden während *entkoppelter Atmung*, nach Behandlung mit dem mitochondrialen Entkoppler FCCP. Je nach Larvenstadium stieg die Wärmeerzeugung zwischen 55 % bis zu 95 % an. Unser kalorimetrisches System kann mit anderen analytischen Methoden kombiniert werden und ermöglicht somit ein ganzheitliches Verstehen fundamentaler biologischer Prozesse.

Zusammenfassung

In einer zweiten Studie präsentieren wir ein mikrofluidisches System für die Kultur von Nematoden mit integrierten optischen Sauerstoffsensoren zur Messung ihrer Sauerstoffverbrauchsrate. Die Chips wurden mit off-stoichiometry dual-cure thiol-ene-epoxy (OSTE+) Polymer hergestellt, was zuverlässige Messung der on-chip Sauerstoffkonzentration und die Fertigung von hochauflösenden Mikrostrukturen im μm -Bereich ermöglichte. Unser mikrofluidischer Ansatz ermöglicht das Einsperren eines einzelnen Nematoden ab dem L4 Stadium über einen Zeitraum von 7 Tagen. Ein automatisiertes Protokoll erlaubt die Kultur und die gleichzeitige Messung des Sauerstoffverbrauchs. Wir fanden einen Anstieg des Sauerstoffverbrauchs vom Larvenstadium L4 zum Erwachsenenalter, und eine kontinuierliche Verringerung mit dem Älterwerden. Behandlung mit dem mitochondrialen Entkoppler FCCP führte zu einem Anstieg des Sauerstoffverbrauchs um einen Faktor ≈ 2 im Vergleich zu basalen Bedingungen. Nach Behandlung mit dem Hemmstoff Natriumazid messen wir Sauerstoffverbrauchsrate von ungefähr null.

Ein drittes Projekt befasste sich mit der Entwicklung einer neuen Methode für die Studie der mechanischen Eigenschaften der embryonalen Eierschale von *C. elegans*. Untersuchungen während der Embryogenese können fundamentale Fragen der Entwicklungsbiologie beantworten. Der *C. elegans* Embryo ist umfangreich erforscht, dennoch fehlen bisher Analysen seiner biomechanischen Eigenschaften. Das ist überraschend, da der Schutz von externen Einflüssen eine der wichtigsten Funktionen der Eierschale ist. In dieser Arbeit benutzten wir CFM, eine Technik für die Mikroindentation von biologischen Samples mit Kraftmesspräzision nahe der von Rasterkraftmikroskopie, für die Analyse von lebenden Embryos. Zudem bewiesen wir die Fähigkeit der Technik, Veränderungen in der Zusammensetzung der mehrschichtigen Schale nach (bio)chemischen Modifikationen zu erkennen. Wir untersuchten ebenfalls den Einfluss der verschiedenen Behandlungen auf die mechanische Unversehrtheit des Embryos. Numerische Simulationen an einem einfachen 3D Modell erlaubten die Bestimmung von charakteristischen mechanischen Kennzahlen der Eierschale aus experimentellen Indentationskurven. Die Schwere der Behandlungen hatte dabei einen starken Einfluss auf die Stabilität der Schale. Darüber hinaus und entgegen bisheriger Annahmen zeigten unsere Resultate, dass kurze Behandlungen mit Bleichmittel nicht nur die äußerste Vitellinmembran entfernen, sondern auch die darunterliegende Chitinmembran attackiert. Genaues Abfühlen von Änderungen in der Zusammensetzung der embryonalen Eierschale ermöglicht weitere, fortgeschrittene Untersuchungen am Embryo im Hinblick auf die Korrelation von mechanischen Eigenschaften mit anderen Phenotypen oder genetischen Einflüssen.

Stichwörter: *Caenorhabditis elegans*, Embryos, Larven, mikrofluidische Kultur, Stoffwechsel, Wärmezeugung, Nanokalorimetrie, Sauerstoffverbrauch, mitochondriale Entkopplung, Mikrofabrikation, Cellular Force Microscopy, embryonale Eierschale, mechanische Eigenschaften.

Résumé

Caenorhabditis elegans (*C. elegans*) est l'un des organismes modèles les plus attrayants dans la recherche biomédicale pour comprendre les maladies humaines et pour tester les médicaments au niveau de l'organisme entier, puisque de nombreux gènes et voies biologiques ont été conservés entre lui et les humains. Le nématode est suffisamment complexe pour que des questions biologiques complexes puissent être abordées, pourtant l'organisme est encore assez simple pour être utilisé dans des tests *in vivo* à haut débit. À travers ce travail, nous présenterons de nouveaux outils basés sur la microfluidique et les capteurs MEMS, qui permettent la caractérisation de vers et des embryons de *C. elegans*, *in vivo*. Étant donné que le dysfonctionnement mitochondrial est présent dans de nombreuses maladies, y compris les troubles métaboliques et les affections liées au vieillissement, nous nous sommes concentrés sur la caractérisation du métabolisme de *C. elegans* aux stades larvaire et adulte. Le fonctionnement mitochondrial peut être quantifié par la production de chaleur métabolique et l'absorption d'oxygène, deux phénotypes clés pour évaluer la respiration mitochondriale. L'embryon de *C. elegans* peut également être utilisé pour des études biologiques, par exemple des expériences sur le développement. Dans le cadre de ce travail, nous avons enquêté les propriétés mécaniques de la coquille d'œuf de l'embryon de *C. elegans in vivo*.

Dans une première partie de cette thèse, nous présenterons nos mesures de la production de chaleur métabolique de petites populations larvaires de *C. elegans*. La production de chaleur, qui peut être mesurée par calorimétrie directe, est un phénotype qui permet d'évaluer l'activité métabolique des organismes vivants. Nous avons développé un système nanocalorimétrique basé sur des capteurs thermopiles microfabriqués qui sont intégrés à des puces microfluidiques. En plus de la polyvalence de la manipulation fluide des échantillons sur la puce, notre approche permet de confiner les populations de vers près de la surface du capteur Si, permettant ainsi une grande sensibilité des analyses. Nos résultats indiquent une augmentation de la production de chaleur par volume corporel des stades larvaires L2 à L3, et une diminution significative des stades L3 à L4. De plus, après traitement avec un agent de découplage mitochondrial induisant une respiration maximale, directement sur la puce, nous avons étudié la production de chaleur métabolique des populations larvaires. L'induction d'une respiration découplée entraîne une augmentation de la production de chaleur métabolique d'un facteur de ≈ 1.5 à 2 par rapport aux vers non traités. Nos expériences ont

Résumé

démontré que la nanocalorimétrie est une technique à la fois directe et très sensible qui peut être combinée à d'autres méthodes analytiques pour ouvrir la voie à une compréhension plus holistique des processus biologiques fondamentaux.

Ensuite, nous introduirons un nouveau système microfluidique d'élevage de vers avec détection intégrée de la concentration d'oxygène au sein de la puce, pour mesurer l'absorption d'oxygène des vers *C. elegans*. La puce microfluidique a été fabriquée en OSTe+ pour permettre une mesure fiable de l'oxygène dissous et la fabrication de structures à l'échelle du μm . Notre approche microfluidique permet de confiner un seul nématode du stade L4 dans une chambre de culture sur une période pouvant atteindre 7 jours. Nous avons appliqué un protocole automatisé de nutrition et de mesure du taux de consommation d'oxygène (OCR) pendant le développement du ver. Nous avons constaté une augmentation des valeurs d'OCR entre le stade et le ver adulte, et une diminution continue lorsque le ver vieillit. De plus, nous avons effectué une expérience sur le métabolisme de *C. elegans* à l'aide d'un agent de découplage mitochondrial, qui a augmenté l'OCR d'un facteur de ≈ 2 par rapport aux taux de respiration basal. Le traitement à l'azoture de sodium a inhibé la respiration mitochondriale et ramené les valeurs d'OCR à zéro.

Dans une troisième étude, nous avons développé une nouvelle méthode pour étudier les propriétés mécaniques de la coquille d'œuf de *C. elegans*. Au cours de l'embryogenèse, il est possible d'effectuer des tests axés sur les phénomènes biologiques émergents dans la vie de l'animal. Cependant, bien que l'embryon de *C. elegans* ait été largement étudié, ses propriétés biomécaniques sont peu connues. Cela est surprenant, car l'une des fonctions les plus importantes de la coquille d'œuf est de soutenir physiquement l'embryon durant son développement et de le protéger des stimuli externes. Nous utilisons la microscopie à force cellulaire (CFM), une technique qui combine la micro-indentation avec la détection de force à haute résolution, afin d'étudier quantitativement les propriétés mécaniques de cette coquille. De plus, nous démontrons la capacité du système à détecter les changements des paramètres mécaniques de la coquille et les dommages causés par des traitements chimiques qui modifient sélectivement la structure multicouche de la coquille. Par ce moyen, nous évaluons le rôle des différentes couches sur l'intégrité mécanique de l'embryon. Nous avons ensuite extrait les paramètres caractéristiques de la coquille d'œuf grâce aux courbes force-déplacement des expériences de micro-indentation, avec la méthode des éléments finis simulés sur un modèle d'embryon. Nous avons trouvé une forte corrélation entre le traitement chimique et la rigidité de la coque. La détection précise des changements dans l'intégrité mécanique de l'embryon permet éventuellement de réaliser des tests plus avancés sur les embryons en vue de corréler les propriétés mécaniques avec d'autres paramètres phénotypiques ou génétiques.

Mots-clés : *Caenorhabditis elegans*, embryons, larves, culture microfluidique, métabolisme, production de chaleur, nanocalorimétrie, consommation d'oxygène, découplage mitochondrial, microfabrication, microscopie à force cellulaire, coquille embryonnaire, propriétés mécaniques.

Contents

Acknowledgements	iii
Abstract (English/Deutsch/Français)	v
List of figures	xiv
List of tables	xvii
1 Introduction	1
1.1 <i>Caenorhabditis elegans</i> - Nature's Gift to Science	1
1.2 Metabolism	4
1.3 Microfluidics for <i>C. elegans</i> research	7
1.3.1 Basics of microfluidics and lab-on-a-chip	7
1.3.2 Microfluidic systems for <i>C. elegans</i> studies	9
1.4 Thesis outline	11
2 Direct calorimetry of <i>Caenorhabditis elegans</i> larvae	13
2.1 Introduction	14
2.2 State-of-the-art	15
2.2.1 Commercial isothermal microcalorimetry for biology	15
2.2.2 Isothermal microcalorimetry for <i>C. elegans</i>	19
2.2.3 Chip calorimetry for biological applications	20
2.3 Theoretical principals of heat conduction calorimeters	21
2.4 Microfluidic chip fabrication	23
2.4.1 Mask fabrication	23
2.4.2 SU-8 master fabrication	23
2.4.3 Chip assembly	25
2.5 Microfluidic nanocalorimetry system	27
2.5.1 Description of the nanocalorimetric system	27
2.5.2 Sensor calibration	30
2.5.3 Worm chip design	32
2.6 Experimental	33
2.6.1 <i>C. elegans</i> age-synchronization	33
2.6.2 Metabolic heat measurement protocol	33

Contents

2.6.3	Quantification of a worm population	36
2.7	Results	37
2.8	Discussion	41
2.9	Conclusions	44
3	Indirect calorimetry of <i>Caenorhabditis elegans</i> worms	45
3.1	Introduction	46
3.2	Current approaches for OCR measurements	47
3.2.1	Small-scale systems based on electrochemical detection	47
3.2.2	Miniaturized systems using luminescence-based oxygen sensors	47
3.2.3	Commercial OCR equipment	49
3.3	OCR measurements of <i>C. elegans</i>	51
3.4	Microfluidic approach for oxygen sensing	53
3.4.1	Considerations for on-chip culture and OCR measurements	53
3.4.2	Integration of the oxygen sensor	55
3.4.3	Microfabrication	56
3.5	Experimental	59
3.5.1	Experimental setup	59
3.5.2	Worm chip design and worm loading	61
3.5.3	Sensor calibration	62
3.5.4	Materials for metabolic assays and on-chip worm culture	62
3.5.5	Assay protocols	63
3.5.6	On-chip OCR measurement protocol	65
3.6	Results	67
3.6.1	Optimization of OSTe+ fabrication	67
3.6.2	On-chip metabolic assay of <i>C. elegans</i>	68
3.6.3	OCR measurements during long term culture of <i>C. elegans</i> on-chip	70
3.7	Discussion	73
3.8	Conclusion	75
4	Force microscopy of <i>Caenorhabditis elegans</i> embryos	77
4.1	Introduction	78
4.2	Cellular force microscopy setup	79
4.2.1	MEMS capacitive force sensors	79
4.2.2	CFM system	81
4.3	Experimental	83
4.3.1	Age-synchronized <i>C. elegans</i> culture and embryo harvesting	83
4.3.2	Eggshell treatment protocols	83
4.3.3	CFM micro-indentation protocol	84
4.4	Results	85
4.4.1	Structural and morphological changes upon indentation for different shell treatments	85
4.4.2	Experimental indentation curve analysis	88

4.4.3	Viscoelastic behavior	90
4.4.4	Model for FEM simulations of embryo indentation	92
4.4.5	Determination of the eggshell Young's moduli	95
4.4.6	Summary of the results	99
4.5	Discussion	101
4.6	Conclusion	103
5	Conclusion and outlook	105
A	Appendix	109
	Bibliography	111
	Acronyms	125
	Constants & Symbols	129
	Curriculum Vitae	133

List of Figures

1.1	Bright-field microscope image of an adult <i>C. elegans</i> .	2
1.2	Schematic of the <i>C. elegans</i> life cycle	3
1.3	Intermediary metabolism of <i>C. elegans</i> .	4
1.4	<i>Coupled</i> and <i>uncoupled respiration</i> .	6
1.5	Assay of mitochondrial function.	7
1.6	High-content phenotyping of <i>C. elegans</i> using microfluidics.	10
2.1	Commercial IMC device for heat flow measurements.	16
2.2	Commercial parallelized IMC device.	18
2.3	Metabolic heat of large <i>C. elegans</i> adult populations measured by IMC.	19
2.4	Age-dependent metabolic heat of <i>C. elegans</i> populations measured by IMC.	20
2.5	Thermopile principle of operation.	22
2.6	Mask fabrication process	23
2.7	Mold fabrication process	24
2.8	Full wafer scale PDMS microfluidic chip fabrication and assembly process.	26
2.9	Photograph of the final chip on a glass slide.	27
2.10	Xensor NCM9924 thermopile sensors	28
2.11	3D model of the nanocalorimetric system.	29
2.12	Schematic cross-sectional view of the calorimetric system.	29
2.13	Fluidic chip for the calibration of the thermopile sensor.	30
2.14	Calibration of the thermopile sensor based on mixing enthalpy measurements.	31
2.15	Microfluidic chip for <i>C. elegans</i> nanocalorimetric assays.	32
2.16	Worm loading and oscillatory loading for metabolic assays of <i>C. elegans</i> larval populations	34
2.17	Metabolic heat measurement flow protocol for worms treated with the uncoupling agent FCCP.	35
2.18	Image processing for counting on-chip worm populations.	36
2.19	Quantification of metabolic heat power of on-chip worm populations.	37
2.20	Control measurements for metabolic assays.	39
2.21	Overview and analysis of the metabolic heat data comparing <i>coupled</i> and <i>uncoupled respiration</i> of <i>C. elegans</i> at different larval stages.	40

List of Figures

3.1	Illustration of the sensing principle of luminescence lifetime-based oxygen concentration measurements.	48
3.2	Commercial Seahorse XF respirometers.	50
3.3	Microchamber-based approaches for OCR sensing on <i>C. elegans</i>	52
3.4	Single worm respiration rates of <i>C. elegans</i> in basal and uncoupled conditions obtained in a Seahorse XF96 respirometer.	53
3.5	On-chip luminescence-based oxygen sensing method.	56
3.6	Illustration of the OSTE+ replica molding process.	57
3.7	Illustration of the OSTE+ chip assembly process.	58
3.8	Photographs of the final OSTE+ chip and chip assembly.	58
3.9	Setup for microfluidic culture of <i>C. elegans</i> worms and OCR experiments.	60
3.10	Microfluidic culture chamber with integrated luminescence-based oxygen sensing for the culture of <i>C. elegans</i> worms.	61
3.11	Flow protocol for on-chip culture of L4 and adult worms	64
3.12	On-chip OCR control measurements and representative single-worm experimental oxygen concentration curves.	65
3.13	Optimization of OSTE+ microfluidic chip fabrication.	67
3.14	Metabolic assay of L4 worms using FCCP and sodium azide.	69
3.15	Bright-field microscopy images during single worm culture on-chip.	71
3.16	Single worm long term measurements of OCR on-chip.	72
4.1	MEMS-based capacitive force sensor.	80
4.2	System for micro-indentation measurements on <i>C. elegans</i> embryos.	82
4.3	Illustration of the eggshell treatment protocol.	83
4.4	Schematics of eggshell indentation.	84
4.5	Structural changes of the eggshell upon chemical treatment.	85
4.6	Morphological changes of the eggshell upon chemical treatment and indentation.	86
4.7	Morphological changes as derived from microscopy images upon indentation.	87
4.8	Force-displacement measurements of <i>C. elegans</i> embryos.	88
4.9	Effective stiffness of <i>C. elegans</i> embryos.	90
4.10	Hysteresis area of the force indentation loading cycles	91
4.11	FEM model of <i>C. elegans</i> embryo indentation experiments.	93
4.12	FEM simulation of the embryo deformation.	94
4.13	FEM simulation of the internal pressure and force on the indenter.	95
4.14	Evaluation of specific mechanical properties of <i>C. elegans</i> embryos.	96
4.15	Results of the evaluation of the mechanical properties of <i>C. elegans</i> embryos.	97
4.16	Simulated E_{shell} values as a function of the eggshell thickness t	98
4.17	Clustergram representation of force-indentation results.	99
5.1	Microtemplates for confining <i>C. elegans</i> embryos and worms.	107

List of Tables

2.1	Basal heat production rates of living organisms.	15
2.2	List of metabolic assays performed on larval <i>C. elegans</i>	38
2.3	Volumetric data of larval <i>C. elegans</i>	41
2.4	Statistical analysis of metabolic assays.	41
3.1	Overview of relevant materials for microfluidic chip fabrication with integrated oxygen sensors.	54
4.1	Linear regression of E_{visco} as a function of F_z^{max}	92
4.2	Experimental results of all force-indentation measurements.	100

1 Introduction

1.1 *Caenorhabditis elegans* - Nature's Gift to Science

Significance and milestones

In 1963, Sydney Brenner first suggested the use of the nematode *Caenorhabditis elegans* (*C. elegans*) to study developmental biology - a proposal which eventually led him, together with John Sulston and Robert Horvitz, to win the Nobel prize in Physiology or Medicine in 2002, the acceptance speech of which he titled "Nature's Gift to Science" [1]. He began researching "how genes might specify the complex structures found in higher organisms" by using the simple roundworm. By 1974, the animal is established as a major model organism in biology [2]. It has become evident why he called the organism a "Gift to Science": it is a multicellular entity and much simpler than mammals, but still elaborate enough to study complex biological questions that cannot be addressed in unicellular organisms, *e.g.* cell differentiation or organ development. Research based on *C. elegans* has brought about another Nobel Prize in Physiology or Medicine in 2006 by Andrew Fire and Craig Mello, for their discovery of "RNA interference - gene silencing by double-stranded RNA". *C. elegans* was also involved in a Nobel Prize in Chemistry in 2008 by Osamu Shimomura, Martin Chalfie, and Roger Tsien for the discovery and development of the green fluorescent protein (GFP) [3, 4]. In one of his first experiments, Chalfie stained individual cells in the transparent nematode with GFP. In 1998, the worm was the first multicellular organism to have its whole 97-mega base pair genome sequenced [5]. Moreover, it is currently the only organism with a complete wiring diagram of its 302 neurons [6, 7], which possibly gives insight in understanding behavioral patterns derived from neuronal links.

Today, the worm has significant importance in a multitude of biomedical research areas, including molecular-, developmental- and neurobiology, genetics, aging, and the research of human diseases. Many molecular pathways, including genes linked to human diseases, are conserved between the nematode and humans [2, 8]. Actually, humans share approximately 40 % matching genes[5], and an estimated 65 % matching disease genes with the nematode [9]. Disease genes that are commonly associated with neurodegenerative diseases such as

Chapter 1. Introduction

Alzheimer's, Parkinson's, Huntington's, and amyotrophic lateral sclerosis or metabolic diseases such as diabetes mellitus, cardiovascular disease and obesity. Many other diseases have been found to have orthologs in the *C. elegans* genome, which makes the worm a perfect candidate to model these disorders [8, 10, 11]. Mitochondrial dysfunction has been shown to be linked to these disorders as well [12, 13, 14, 15, 16, 17, 18]. Even if the small worm may not perfectly simulate disease pathways in humans, use of the organism allows to gain more insight in the functioning of the diseases *in vivo*. More recently, the worm is emerging as a candidate for automated high-throughput and high-content drug screening, for testing potential compounds on a whole-organism level [19, 20, 21].

Using *C. elegans* in studies *in vivo* opens the way to evaluate responses on a whole-organism level. In contrast to cell or tissue models for example, the worm enables to assess resulting phenotypes such as life span, feeding, behaviour, reproduction, and the interaction with chemicals in a simple way, where vertebrate animals might be too complex to understand fundamental causes. It might be envisioned that nematode assays greatly reduce or eliminate the need for experimentation with vertebrate animals.

Description of the organism

C. elegans is a ≈ 1 mm-sized transparent soil nematode that consists of 959 somatic cells of which 302 are neurons. Fig. 1.1 shows a bright-field microscopy image of an adult worm.



Figure 1.1 – Bright-field microscope image of an adult *C. elegans*.

In the laboratory, *C. elegans* is a very convenient organism that can be cultured at low cost. *C. elegans* is usually maintained at room temperature on special nematode growth medium (NGM) agar plates, which contain a lawn of *Escherichia coli* (*E. coli*) OP50 bacteria as food source [2, 22]. The culture is very robust, as the worm can grow at temperatures ranging from 16 °C to 24 °C and the offspring can survive for weeks without food. The short 3-day life cycle (at a temperature of 22 °C) from embryo to the egg-laying adult nematode is shown in Fig. 1.2 [23]. After fertilization of the eggs, the embryos develop for about 2.5 h *in utero*. Eggs are laid at the gastrula stage, where the embryo consists of about 30 cells. During the 9 h *ex utero* development phase, the embryo transforms into a twitching larval worm, which hatches by penetrating the eggshell upon completion of the embryo development. Provided that the freshly hatched larval stage 1 (L1) worms have food available, they develop during ≈ 56 h into adult worms that are capable of egg laying. In case of unfavorable environmental conditions, L1 larvae enter a developmental stage called 'dauer', which is a state where the

1.1. *Caenorhabditis elegans* - Nature's Gift to Science

worms almost stop aging and can survive many times their normal life span (up to 4 months). The dauer stage allows the larval nematode to overcome a lack of food, crowding or high temperatures. The adult hermaphrodites are highly prolific, spawning around 300 embryos per animal. The large number of offsprings in combination with the worms short life cycle facilitates studies even over multiple generations. *C. elegans* is predominantly hermaphroditic, but a natural population also contains a small ratio of male worms (0.1% to 0.2%) [24]. Age-synchronized populations can be easily obtained by isolating embryos from a mixed worm population and starting a culture from the isolate. Even more precisely synchronized populations can be obtained when isolated embryos are kept in buffer solution without any food source. The embryos will hatch from the eggs and undergo L1 arrest. From this isolate a synchronized population can be started. Larval developmental stages (L1 to L4) can be easily identified by specific morphological features, their age and/or the length/width of the worms. Embryonic developmental stages can also be easily classified into gastrulation, bean (comma) and twitching (3-fold) stages by morphological features. *C. elegans* worms do not possess a specialized respiratory system [25]. Instead, the animals rely solely on diffusion of molecular oxygen through the tissue into the mitochondria.

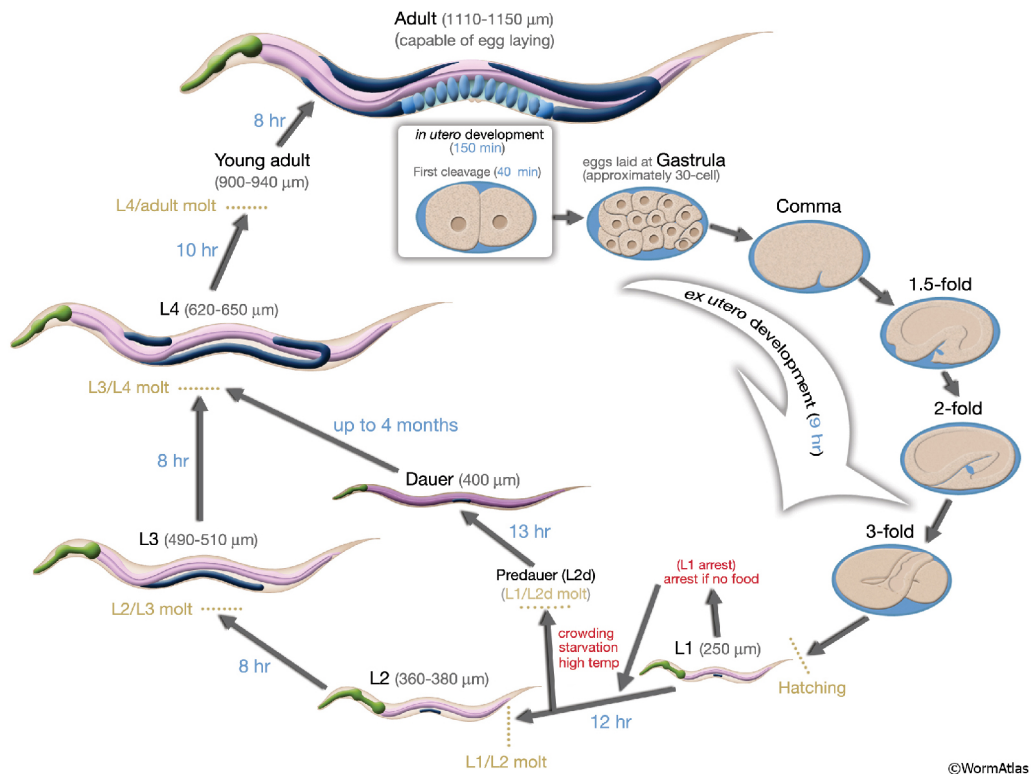


Figure 1.2 – Schematic of the *C. elegans* life cycle. Reproduced with permission from [23].

1.2 Metabolism

Metabolism is defined as the set of vital chemical reactions in an organism that is responsible for the maintenance of life. These reactions comprise the conversion of food to energy to sustain cellular processes, the production of biomolecules as building blocks of the body, and the disposal of waste products that arise from these reactions. These functions enable a living organism to develop, maintain its body structure, reproduce, and adapt to its surroundings. Heterotroph organisms, *i.e.* all animals, fungi and most bacteria, are not able to produce their own food and therefore rely on carbon-based food sources to fuel their metabolic pathways. In heterotroph organisms including *C. elegans*, the major metabolic pathways are well conserved between species [26]. In Fig. 1.3, the major metabolic pathways in the cells of *C. elegans* and other eukaryotes are depicted [27].

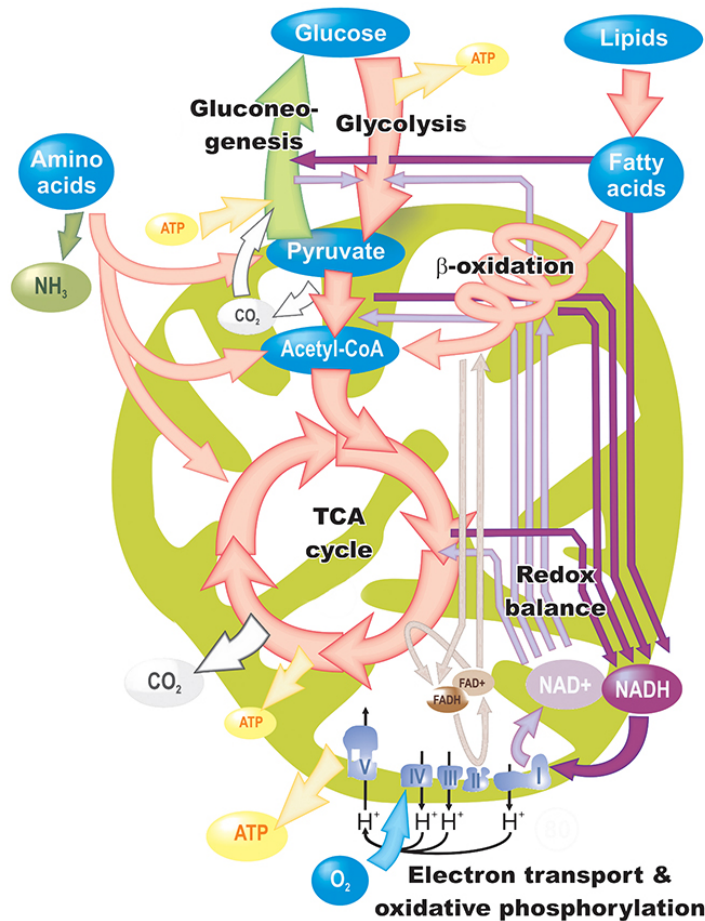


Figure 1.3 – Intermediary metabolism of *C. elegans*. These major metabolic pathways are conserved among most bacteria, all fungi and all animals. Modified with permission from [27], based on [28].

It is common to distinguish between anabolism and catabolism, *i.e.* the synthesis and the breakdown of biomolecules, respectively. Generally, anabolic processes consume energy and catabolic reactions release energy. Metabolic reactions are usually enzyme-mediated, enabling the fast reaction rates required for sustaining the life of an organism [29]. In order to keep metabolic pathways working, homeostasis, *i.e.* an equilibrium condition in which metabolic processes function most efficiently, is required. Such conditions include for example an optimal temperature range or fluid balance, which the organism maintains by reacting to its environment *via* negative feedback loops with the input being responses from sensory systems. In homeothermic species such as humans, for example, the body temperature is regulated at approximately 37 °C, at which the enzyme activity is highest.

Metabolism is closely related to mitochondrial functioning, since the majority of the intermediary metabolism (*i.e.* metabolic pathways related to generation and storage of energy) occurs in the mitochondria. In the following paragraphs, the intermediary metabolism of *C. elegans* is described in more detail.

Aerobic cellular respiration

In aerobic conditions (*i.e.* in the presence of molecular oxygen in a cell), in a chain of coupled processes called aerobic cellular respiration, the cell consumes oxygen to convert carbohydrates, proteins and fats into adenosine triphosphate (ATP). ATP is a molecule that provides energy to fuel the exertion of mechanical work, the transport of molecules or the synthesis of biomolecules, for instance. The simplified chemical reaction for aerobic respiration reads as follows:



The respiratory chain can be loosely separated in three separate stages: acetyl coenzyme A (acetyl-CoA) production, acetyl-CoA oxidation, and oxidative phosphorylation (OXPHOS). The stages are shown in Fig. 1.3. Acetyl-CoA is produced by pyruvate decarboxylation, which on its part is the product of the breakdown of carbohydrates in glycolysis. Glycolysis is a process with 10 individual steps that occurs outside the mitochondria in the cytosol, during which a total of 2 ATP molecules and 2 pyruvate molecules are produced from 1 molecule of glucose. On the other hand, acetyl-CoA is synthesized through the breakdown of amino acids (proteins) or the breakdown of lipids through β -oxidation. In the second stage, the tricarboxylic acid (TCA) cycle (or Krebs cycle), acetyl-CoA is oxidized to produce 2 molecules of ATP, 2 molecules of CO₂, 3 molecules of nicotinamide adenine dinucleotide (NADH) and 1 molecule of flavin adenine dinucleotide (FADH₂).

The third stage of aerobic respiration process is the most energetically rewarding and the most interesting stage for in the scope of this work. During OXPHOS, the electron carrier molecules NADH and FADH₂, which are products of the TCA-cycle in their reduced states, are

Chapter 1. Introduction

used as oxidizers in energy-releasing redox reactions in the presence of oxygen. At the end of the respiratory chain, released energy is used to build up a proton gradient across the inner mitochondrial membrane by powering the proton pumping membrane protein complexes *I*, *III* and *IV* (illustrated in Fig. 1.4). The proton gradient stores potential energy that is used in presence of oxygen to generate ATP from adenosine diphosphate (ADP) by the membrane protein ATP synthase in a process called *coupled respiration*. The naming comes from the fact that the rate of protons that are used for the production of ATP is linked very closely to the rate of the electron transport across the inner mitochondrial membrane, which occurs at the end of the cellular respiration chain. This close link can also be uncoupled by induction of proton leaks through the inner membrane, either by uncoupling membrane proteins (in fat tissue of mammals) or artificially by uncoupling agents, which mediate the transport of protons through the inner membrane. This process is called *uncoupled respiration*. Both cases of proton leaks releasing energy in the form of metabolic heat.

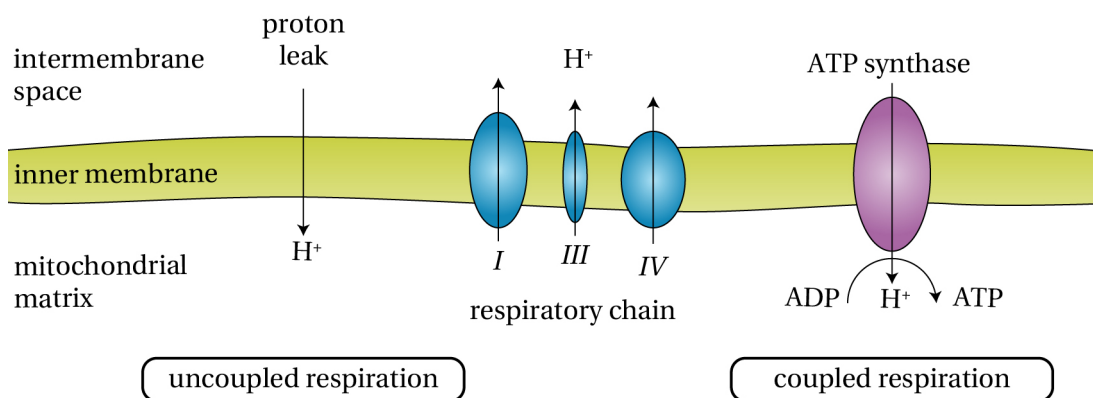


Figure 1.4 – *Coupled and uncoupled respiration*. Based on [30].

Oxygen is the most common electron acceptor throughout the redox reactions occurring in the aerobic respiration chain. It is the key molecule in oxidative phosphorylation, the last and most energetically rewarding stage during the conversion of nutrients into energy. The rate of oxygen uptake hereby mirrors directly the metabolic rate of an organism and proper functioning of its mitochondria.

Metabolic assay

Assessment of mitochondrial health with metabolic assays is crucial to diagnose and treat the wide range of diseases that are associated with mitochondrial dysfunction. Both metabolic heat production and oxygen consumption rate (OCR) can be used to assess mitochondrial function during basal and uncoupled respiration. Usually, a standard test is performed to determine basal respiration, proton leak, ATP turnover, spare respiratory capacity and non-mitochondrial respiration [31]. In Fig. 1.5, a metabolic heat or OCR profile during a mitochondrial assay is shown. The basal respiration rate is measured during regular culture in

medium. ATP production is assayed by the injection of oligomycin into the sample chamber. Oligomycin inhibits ATP synthase by blocking proton influx through the enzyme, which causes the electron transport chain to stop. Injection of an uncoupling agent (*e.g.* carbonyl cyanide 4-(trifluoromethoxy)phenylhydrazone (FCCP)), a molecule that carries protons across the inner mitochondrial membrane, causes the uncoupling of electron transport and phosphorylation (discussed in more detail in the previous subsection). As a result, mitochondrial proton pumps operate at maximal activity, leading to an increased OCR. However during *uncoupled respiration*, pumped protons are immediately transported back across the membrane, dissipating heat. Therefore both metabolic heat production and OCR increase during *uncoupled respiration*. Finally, injection of azide (N_3^-) inhibits mitochondrial respiration completely by preventing the formation of a proton gradient across the inner mitochondrial membrane.

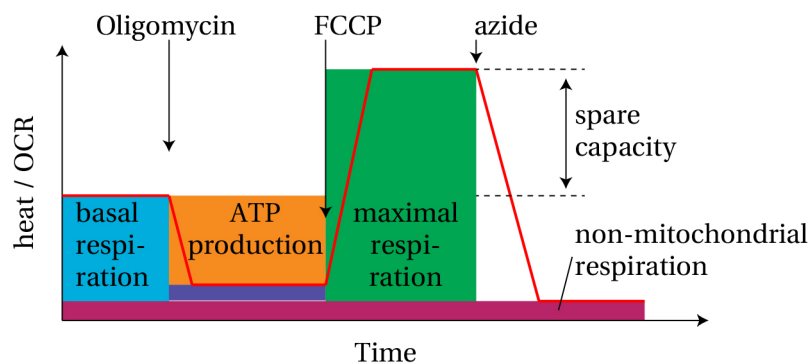


Figure 1.5 – Assay of mitochondrial function. Standard mitochondrial assay protocol in direct and indirect calorimetry to determine the basal respiration, ATP production, maximal respiration, spare capacity as well as non-mitochondrial respiration. Based on [31].

1.3 Microfluidics for *C. elegans* research

The use of microtechnology opens many new possibilities for more accurate and complex assays of *C. elegans* nematodes. With feature sizes down to $1\ \mu\text{m}$, it covers the relevant range required for manipulation, confinement and characterization of the worms in microfluidic and micromechanical applications.

1.3.1 Basics of microfluidics and lab-on-a-chip

The development of lab-on-a-chip (LOC) systems enabled to shrink large-scale laboratories within the boundaries of a single chip using microfluidics. A common definition of microfluidics is the manipulation of small amounts of liquids ranging from 10^{-9} l to 10^{-18} l in channels with dimensions ranging from tens to hundreds of μm in small microfabricated devices [32, 33]. In LOC systems, analytical protocols can be implemented in a highly parallelized manner with minute sample volumes, on short time scales and potentially at low cost [34, 35].

Chapter 1. Introduction

The dynamics, *i.e.* the flow velocity field \vec{v} of a viscous fluid, is described by the Navier-Stokes equation:

$$\rho(\delta_t \vec{v} + (\vec{v} \cdot \nabla) \vec{v}) = -\nabla p + \eta \nabla^2 \vec{v}, \quad (1.2)$$

with the pressure p , dynamic viscosity η and the mass density ρ . The equation is essentially the application of Newton's second law to fluid motion: its left side describes changes of momentum in a fluid, the right side is the sum of forces acting on the fluid. In the microfluidic regime, body forces such as gravity can often be neglected. However, surface forces such as viscous forces become very important. In this limit, fluidic effects such as diffusion, capillary forces and laminar flow in particular dominate macro-scale effects caused by inertial forces, for example turbulence. The corresponding flow regime to a specific fluidic system can be easily characterized by means of the Reynold's number Re :

$$Re = \frac{\rho V_0 L_0}{\eta}, \quad (1.3)$$

where V_0 and L_0 are characteristic mean flow velocity and dimensions of the system. Re is the ratio of inertial forces to viscous forces, which helps to predict whether flows are turbulent or laminar. For low $Re \ll 100$, flows in a system are very predictable and allow delicate fluidic manipulation of biological organisms, for example. The Navier-Stokes equation then reduces to the Stokes equation:

$$0 = -\nabla p + \eta \nabla^2 \vec{v}, \quad (1.4)$$

for either low flow velocities, small channel dimensions or high viscosities. Diffusion of particles in a concentration gradient *via* Brownian motion is often relevant in the microfluidic regime. The Stokes-Einstein equation allows to calculate the diffusion coefficient D of a spherical particle in a fluid:

$$D = \frac{k_B T}{6\pi r \eta}, \quad (1.5)$$

where r is the particle radius, T is the temperature and k_B is the Boltzmann constant. If D is known, the root mean square distance l travelled by the particle in time t in the one-dimensional case can be calculated using:

$$l = \sqrt{2Dt} \quad (1.6)$$

1.3.2 Microfluidic systems for *C. elegans* studies

Microfluidics has emerged as a powerful tool for *C. elegans* studies, providing the opportunity to physically manipulate, confine and phenotype individual worms and populations of worms in an automated and high-throughput manner [36, 37, 38, 39]. Such LOC systems are especially suitable for testing compounds in physiological conditions at a whole-organism level with single organism resolution and allowing versatile and more precise assays beyond the capabilities of traditional techniques involving the culture of worm populations on agar plates [40]. For example, a microfluidic system developed by Letizia *et al.* allows isolating and monitoring 16 individual *C. elegans* worms during their full life-cycle including embryo development [41]. Their chip is shown in Fig. 1.6a. Freshly laid eggs from the parent culture chamber (left side) are transferred to the progeny culture arrays (right side). Single embryos are hydrodynamically trapped in an embryo incubator adjacent to each culture chamber, allowing parallel time-lapse embryo imaging. The design of the embryo incubators corresponds to a design first presented by Cornaglia *et al.* (Fig. 1.6b) [42]. After embryos hatch, L1 worms are transferred into the culture chamber, where the worms were monitored individually. The platform was used to phenotype the worms in control conditions as well as in treated conditions, where mitochondrial stress was induced by the drug doxycycline and quantified using fluorescence microscopy on mutant *hsp-6p::gfp* worms. A different microfluidic platform by Atakan *et al.* offers automated high-content phenotyping from larval stage L1 until early adulthood in a parallelized approach [43]. Their chip design is illustrated in Fig. 1.6c. 8 separate fluidic lanes each divided in 4 individual chambers with tapered channels for worm immobilization allow multiplexed phenotyping in different physiological conditions side-by-side in each individual lane. Here, automated fluidic manipulations and imaging allowed performing the experiments without human intervention. With a custom worm tracking and image/video processing algorithm, the authors were able to extract 19 phenotypes, and study for instance the food dependence of *e.g.* worm length, body volume, motility and mitochondrial stress.

Other approaches to handle worms using microfluidics have been presented before. For example, devices by Dong *et al.* can sort mixed worm populations and prepare age-synchronized worms for later use by using deformable membranes to create variable channel cross-sections fitting particular larval stages [44]. Churgin *et al.* developed a microfabricated array of 240 wells containing agar for cultivation and imaging of a single worm per well in conditions of standard culture [45]. To extract early embryos (from the 1 cell stage from gravid nematodes in a high-throughput way, Dong *et al.* created a microfluidic trap for crushing an on-chip worm population using an external force [46]. By squeezing the worms, embryos are released and collected in a trapping array for imaging.

This brief sketch shows that microfluidics has great potential to substitute traditional culture protocols and to perform long-term longitudinal studies on single *C. elegans* worms. So far however, read-out of crucial phenotypes for assessing mitochondrial function directly from worm within the fluidic channels remained impossible.

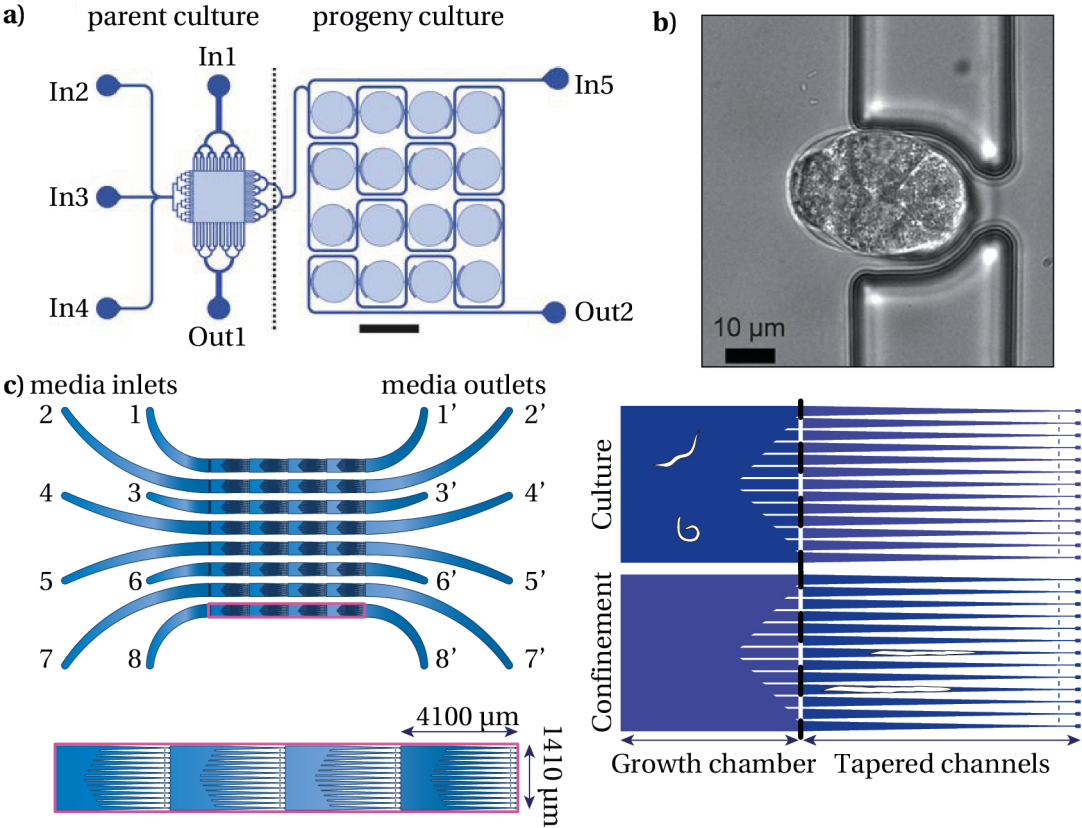


Figure 1.6 – High-content phenotyping of *C. elegans* using microfluidics. **a)** Single-worm full life-cycle phenotyping platform by Letizia *et al.*, adapted and reproduced with permission from [41]. **b)** Embryo incubators by Cornaglia *et al.*, adapted and reproduced with permission from [42]. **c)** Automated high-throughput phenotyping platform by Atakan *et al.*, adapted and reproduced with permission from [43].

1.4 Thesis outline

In this thesis, I present new microfluidic and micromechanical tools for *in vivo* assays on *C. elegans*. Each of the following chapters is dedicated to a separate instrument for studying key phenotypes in *C. elegans* worms and embryos. Due to different technologies used in the developed instruments, a separate state-of-the-art is given in the introduction of each chapter.

Chapter 1 describes key concepts recurring in all chapters of the thesis. An overview of the model organism *C. elegans* is given with relevant context, and metabolism is introduced. Furthermore, a brief review of the basics of microfluidics and a couple of example microfluidic systems for *C. elegans* studies is given.

Chapter 2 introduces a new microfluidic tool for direct calorimetry of *C. elegans*. We developed a thermopile-based calorimetry system and combined sensitive heat power measurements with a microfluidic trap for larval worm populations. It was possible to measure the metabolic heat production of the larval populations during basal respiration and during maximal respiratory capacity.

Chapter 3 shows a microfluidic platform combining long term culturing of *C. elegans* with integrated oxygen concentration sensing. A new fabrication protocol using the polymer OSTE+ was used to fabricate a culture chamber for hosting single L4 to adult worms, within which it was possible to measure the oxygen consumption rate of the worm continuously during up to 7 days in an automated manner.

Chapter 4 presents a new application of CFM, a force-microscopy technique with the possibility to apply multi-scale loads with high displacement ranges. The tool was used in combination with numerical simulations to conduct a quantitative study of the *C. elegans* embryonic eggshell. We developed a method to apply treatments to modify the shell structure that had significant effects on the shell elastic properties.

Chapter 5 summarizes the work and main conclusions, and provides a future outlook.

2 Direct calorimetry of *Caenorhabditis elegans* larvae

Basal heat production is a key phenotype for assessing the metabolic activity of small living organisms. Here, we present a new nanocalorimetric system, based on thin film thermopile sensors combined with microfluidic chips for measuring metabolic heat signals generated by C. elegans larval populations (60 to 220 organisms). In addition to versatile on-chip fluidic manipulation, our microfluidic approach allows confining worm populations close to the sensor surface, thus increasing the sensitivity of the assays. A customized flow protocol for dynamically displacing the worm population on-chip and off-chip was applied. The resulting sequential recordings of heat source and reference signals enabled precise measurements of slow varying heat-generating metabolic processes. We found an increase of the volume-specific basal heat production from the L2 to the L3 larval stage, and a significant decrease from the L3 to the L4 stage. Additionally, we investigated the metabolic heat production of the larval populations during maximal respiratory capacity, i.e. after inducing uncoupled respiration by on-chip treatment with the mitochondrial uncoupling agent FCCP. Depending on the larval stage, inducing uncoupled respiration causes an increase of the metabolic heat production ranging from 55 % up to 95 % with respect to untreated worms.

This section was adapted from the following publications:

- **R. Krenger**, T. Lehnert, and M. A. M. Gijs, “Dynamic microfluidic nanocalorimetry system for measuring *Caenorhabditis elegans* metabolic heat”, Lab Chip, 2018, **18**, p. 1641-1651.
- **R. Krenger**, R. Padovani, T. Lehnert, and M. A. M. Gijs, “Nanocalorimetric device for analysis of mixing enthalpy in microliter segmented flow plugs”, Proc. of 20th International Conference on Miniaturized Systems for Chemistry and Life Sciences (microTAS 2016), Dublin, Ireland, October 2016.

- **R. Krenger**, R. Trouillon, T. Lehnert, and M. A. M. Gijs, “Microfluidic differential nano-calorimetry system for measurement of mixing enthalpy and cellular heat”, Proc. of 21th International Conference on Miniaturized Systems for Chemistry and Life Sciences (microTAS 2017), Savannah GA, USA, October 2017.

2.1 Introduction

Many chemical reactions, changes in physical state or biochemical processes release energy in the form of heat, which can be measured by calorimetric methods [47]. Modern calorimeters, including differential scanning or isothermal titration calorimeters, are used for the evaluation of protein–ligand interactions and conformational transitions in biomolecules, which are important features in the process of drug discovery and functional analysis, but cannot be fully characterized by X-ray crystallography, nuclear magnetic resonance spectroscopy or computational methods alone [48, 49]. Isothermal microcalorimetry (IMC) offers real-time monitoring of heat-generating processes with sensitivities in the μW -range. IMC has been applied for metabolic heat studies of living entities. The technology was shown to be well suited to quantify metabolic rates of bacteria cultures or to detect bacterial contamination in donated blood within a few hours [50, 51]. Recording heat production as a phenotype in metabolic studies may bring about new insights in fundamental biological mechanisms [52]. Today, the main method for evaluating the metabolic activity of cell and bacteria populations, as well as of small living multicellular organisms, is measuring the oxygen consumption rate, an indirect method to quantify mitochondrial respiration [53]. On the other hand, IMC detects metabolic heat signals directly and offers the possibility for real-time bioprocess monitoring. Interestingly, a combination of both methods can give information on the coupling of anabolic (energy-consuming assembly of molecules) and catabolic (energy-releasing breakdown of molecules) processes [54].

Metabolic reactions include, in particular, the generation of the energy-storing compound ATP from ADP through OXPHOS, requiring a proton gradient between the mitochondrial matrix and the intermembrane space that is built up by the so-called electron transport chain (section 1.2, Fig. 1.3/1.4) [55, 27]. This gradient is consumed by ATP synthase to create ATP from ADP in a process called *coupled respiration*. Another H^+ gradient reducing pathway is *uncoupled respiration*, *i.e.* the direct transport of protons across the inner mitochondrial membrane, either via uncoupling proteins, or by means of specific uncoupling agents that may leak across the membrane [27]. *Uncoupled respiration* is a dissipative process that generates metabolic heat and can be induced artificially by exposing the organism to uncoupling agents.

In this work, we focus on metabolic studies using the nematode *C. elegans*, an important model organism for biological and biomedical research related to human health, for instance for studying aging processes or neurodegenerative diseases [19, 56]. Major metabolic pathways are conserved among heterotrophic organisms, such as *C. elegans*, so that findings made in the model organism may possibly be adapted to humans [27, 2, 57]. *C. elegans* is also an

emerging candidate for drug screening on the whole-organism level [19]. For the time being, to the best of our knowledge, only one group has applied direct calorimetry for metabolic studies on *C. elegans* [58, 59]. The authors examined the heat production of large *C. elegans* populations of thousands of worms by means of IMC with a focus on aging and decline of metabolic activity at advanced age (more details in section 2.2.2). Findings showed that the heat output per worm normalized to the protein content decreased exponentially during the worm aging process in the adult phase. However, time resolution and precision of IMC systems were not sufficient to derive conclusions during larval development. Additionally, basal heat production rates of living organisms, such as bacteria and cells, have been measured in commercial IMC microcalorimeters. Tab 2.1 gives an overview of typical heat production rates of important living biological model systems (compiled from two review papers [60, 61]).

Living organism	Heat production rate per organism
<i>E. coli</i> (aerobic)	1 pW
Rat white adipocytes	40 pW
Rat hepatocytes	330 pW
Human myocardial cells	2 nW
Adult <i>C. elegans</i>	13 nW

Table 2.1 – Basal heat production rates of living organisms.

This work presents a new microfluidic nanocalorimetry device, designed for on-chip metabolic heat measurements of living organisms. *C. elegans*, due to its biological significance, was chosen for a proof-of-concept study, in which we measured the basal metabolic heat production and the impact of a treatment with the mitochondrial uncoupling agent FCCP on the metabolic activity at different larval stages. Our microfluidic approach allows for precise handling of small worm populations and reversible application of active compounds during the assay. A sequential sample loading/unloading protocol to the thermopile sensor surface overcomes a fundamental limitation of the nanocalorimetric approach related to slow biological heat producing processes. The actual device design incorporates two independent thermopile sensors for parallel experiments.

2.2 State-of-the-art

2.2.1 Commercial isothermal microcalorimetry for biology

Texas Instruments - TAM

IMC is an interesting technology with applications to living organisms in biological studies. A state-of-the-art commercial microcalorimeter (TAM IV/TAM IV-48, TA Instruments, USA) is shown in Fig. 2.1. This line of devices, together with a handful of other devices, such as the MICROSC-4C/C80 (SETARAM Instrumentation, France) or the μ RC (thermal hazard technology, United Kingdom), operate with mL-sized reaction chambers that in some cases allow the injection of a reagent with subsequent mixing [62, 63]. These devices operate

in a twin configuration inspired by the Calvet calorimeter. Hereby, two ampoules, one for sample and one for a reference, are used to increase sensitivity by subtraction of the reference signal from the sample signal [64]. In this way, thermal fluctuations within the device and signal baseline shifts can be eliminated. By careful selection of the control experiment in the reference chamber, heat signals originating from undesired unspecific sources, *e.g.* the mixing enthalpies of buffer solutions, can be eliminated. A thermostat with large mass to optimize the thermal stability during the measurements is integrated in all commercial devices and is in fact a requirement for accurate determination of heat flows. Massive thermostats however have the drawback of long thermalization times until the heat distribution across the device is uniform. On the other hand, by working with large sample volumes and accurate thermostats, precise heat power measurements are possible. The sensing principle is based on the transfer of the produced or consumed heat through a thermoelectric heat flow sensor. The sensor is connected to the heat-producing ampoule with the samples and the isothermal heat sink of the device. Thermal differences between the ampoule and the thermostat are converted by the sensing element to an electric potential based on the Seebeck effect (see section 2.3 for details).



Figure 2.1 – Commercial IMC device for heat flow measurements. The TAM IV series (TA Instruments, USA) offers mL-sized ampoule-based calorimetric measurements, with possibility to perform up to 48 measurements in parallel. The sample ampoules are embedded in a massive thermostat. The injection of compounds, *e.g.* for the determination of mixing enthalpies or the quantification of binding energies is possible in open ampoule configurations. Reproduced from [65].

IMC has been greatly improved during many years until today. The technology has many advantages, but also severe limitations which still need to be overcome. These are discussed in the following (compiled from [47, 66, 67, 50, 51, 68]). State-of-the-art IMC systems are very accurate with heat power sensitivities down to 100 nW. Because of their large thermostats, thermal stability and stable measurement baseline signals are guaranteed beyond 24 h, which

enables the possibility for real-time measurements over long time, for example the measurement of growth curves of bacterial populations. The TAM IV offers thermal stability of $100\ \mu\text{K}$ and baseline shifts as low as $0.04\ \mu\text{W}$ over 24 h [69]. IMC (and calorimetric methods in general) are simple because complicated sample preparation steps are not necessary. In fact, the technique is label-free and non-invasive, which omits the need to manipulate and alter the samples and potentially cause experiment-influencing effects. A further advantage of calorimetry is the universality of the technique. Provided that there is a heat-generating or heat-consuming change in a sample, the technique can be applied to characterize undergoing processes. However, since the measurement of heat flow is non-specific, it is difficult to isolate a system from any potential sources that can influence the characterization of a particular process. For example, non-specific molecular binding, mixing enthalpies of buffers and culture media or even evaporation can contribute significantly to the heat signal, and therefore distort the experimental results. The main disadvantage, especially of the commercial devices that have been presented, are low measurement throughput rates of samples due to long thermalization times of the device. It can take up to 24 h to stabilize the temperature of the device and at least 1 h more when the sample ampoule is inserted into the device. The TAM-48 partially solves this issue, because up to 48 sample ampoules can be measured at the same time. However the sample volume in the ampoules is 4 mL, which is significant when expensive reagents are used for experimentation. During long thermalization times, samples may also degrade until the start of the experiment. Another consequence of the large sample ampoules is a relatively long distance to the sensor which increases the heat transfer time and therefore prolongs the response time between sample reactor and sensor. Sensing time constants can reach up to 150 s. Furthermore, the versatility of experiments is limited. Ampoules are provided in either closed or open configurations. Closed ampoules preclude any interaction with the samples, but open ampoules offer the possibility to inject samples or reagents into the ampoule during experiments. Besides that, there is little room for custom and more sophisticated, complicated experimental designs fluidic manipulations are precluded. A disadvantage specific to long-term culturing of living organisms inside the ampoules such as bacteria, cells or *C. elegans*, is the lack of control of the culture environment during the experiments. After many hours, the media can be contaminated by waste products or depleted of oxygen, for example, which are unsuitable conditions for growth and culturing of organisms.

Such commercial devices are optimized for the pharmaceutical industry, where drug screening is performed by testing the strength of protein-ligand interactions. Several of the limitations of commercial IMC systems, especially with regards to sample size, throughput and applications to living organisms, have been improved in custom laboratory-based chip calorimeters. Some examples are given in section 2.2.3.

Symcel - calScreener

Recently, calScreener (Symcel AB, Sweden), a new generation of parallelized a microcalorimeter for applications in microbiology, has entered the market (photograph shown in Fig. 2.2a) [70]. The system offers to perform IMC in a 48-well cell culture plate format and maintains typical heat power sensitivity in the μW -range. The parallelization of this instrument enables high sample throughput in low assay volumes of 100 μl to 300 μl . A photograph of the plate containing the sample wells is shown in Fig. 2.2b. The device provides an ideal platform for antimicrobial susceptibility testing (AST) with high throughput and in short assay times down to 8 h, about 2 times faster than using classical methods like broth microdilution. Typical heat flow curves obtained by growing *E. coli* in presence of culture media containing varying concentration of antibiotics are shown in Fig. 2.2c, and corresponding bacterial growth curves obtained by integration of the heat flow curves are shown in Fig. 2.2d. With such experiments the dose-dependent effect of the antibiotic on the growth of the bacterial culture can be quantified, for example [71, 72]. Other potential applications of the device include metabolic studies on cell cultures, or brown adipose tissue, for example [73]. The system shares the same limitations as the TAM IV devices (section 2.2.1).

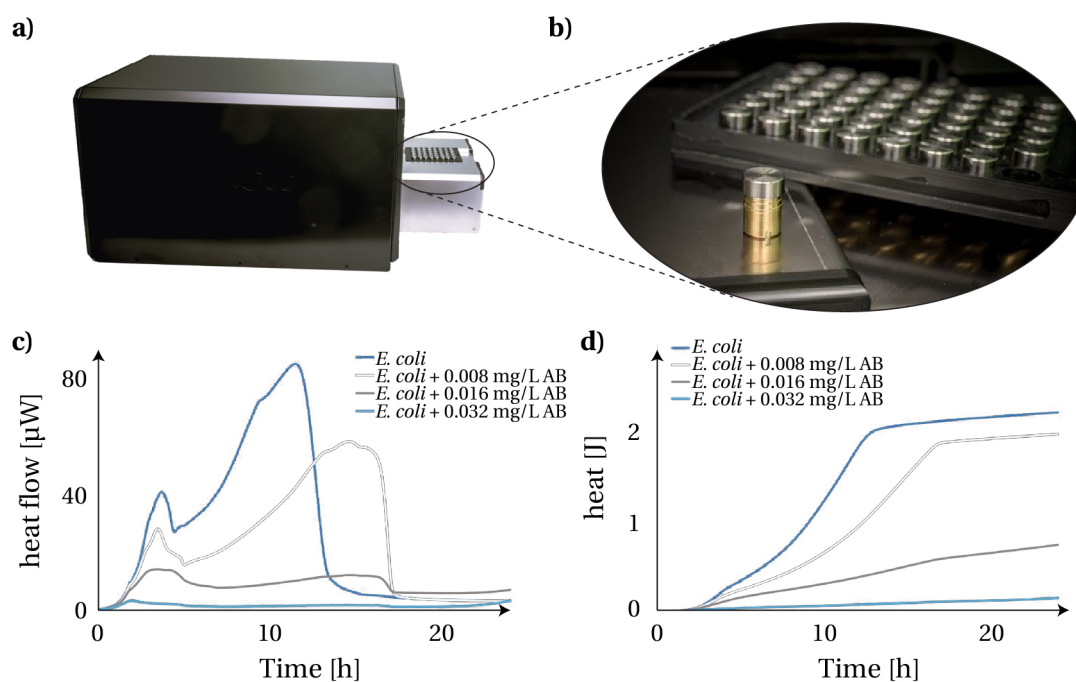


Figure 2.2 – Commercial parallelized IMC device. **a)** Photograph of the commercial, parallelized device (calScreener, Symcel AB, Sweden). **b)** Photograph of the well plate-based insert containing 48 sample ampoules. **c)** Example heat flow curves of *E. coli* growing in presence of different concentrations of a drug AB. **d)** Example total heat produced by the *E. coli* culture, representing bacterial growth curves. Adapted and reproduced from [70].

2.2.2 Isothermal microcalorimetry for *C. elegans*

Commercial IMC has been applied to study the heat production of *C. elegans*. In a study focusing on aging of the nematode, Braeckman *et al.* analyzed the metabolic activity of the worms not only by measuring the metabolic heat production, but also the oxygen consumption, carbon dioxide production and ADP/ATP contents of the worms depending on the protein content as the worms reach old age up to 14 d [58]. For the metabolic heat measurements performed in that work, a large amount of adult worms (approximately 3000 worms) was suspended in 1 mL buffer solution and placed in a commercial microcalorimetry system (Thermal Activity Monitor, Thermometric, Sweden) equipped with 20 mL ampoules. To prevent bacteria growth in the ampoules during long experiments (approximately 15 h), streptomycin and penicillin were added to the worm suspension. Generated metabolic heat signals of the worm populations are shown in Fig. 2.3a. Bacterial growth is dominating heat power signals (dashed line) after the lag phase in the culture medium in the absence of antibiotics. With penicillin and streptomycin, a stable heat power signal of about 13 nW for a single adult worm (aged 13 days) is measured (full line). The age-dependent heat production normalized by the worm protein content is shown in Fig. 2.3b. Values represented by full dots were worms on the surface of culturing medium solidified with agar, values represented by empty circles were worms suspended in liquid medium. Worms living on agar produce about 60 % more metabolic heat. This condition mimics classical *C. elegans* culture in the lab. In both cases, the metabolic heat decreases exponentially after adult age is reached.

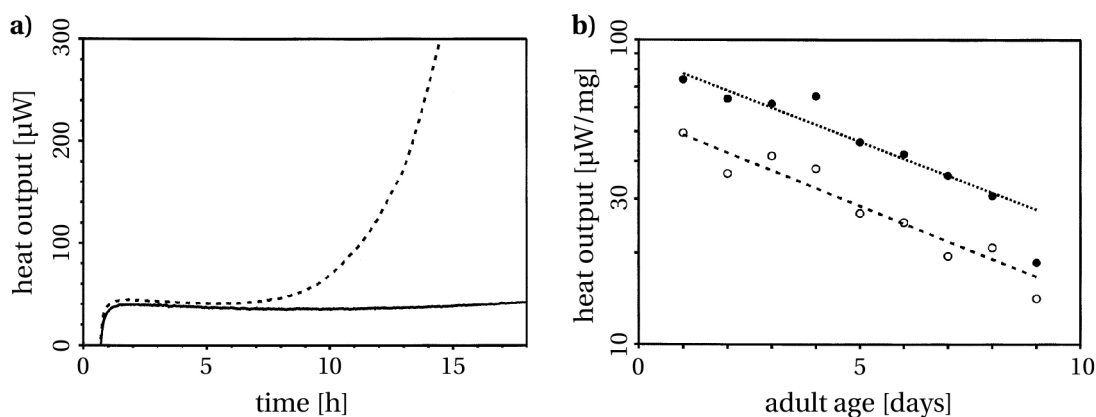


Figure 2.3 – Metabolic heat of large *C. elegans* adult populations measured by IMC. **a)** Dissipated heat of 13 days old adult worms in the presence of antibiotics (full line) and in the absence of antibiotics (dashed line). The heat signal increase in the absence of antibiotics reflects exponential bacteria growth after the lag phase. **b)** Daily measured metabolic heat signals of the worms during aging, normalized by the protein content of the worm population. Reproduced and adapted with permission from [58].

In a similar study performed by the same group, the metabolism of the nematode was analyzed during different developmental stages, including the dauer stage [59]. Again, multiple phenotypes were measured indicating the metabolic activity of the animals, including respiration rate, ADP/ATP contents. The metabolic heat measurements were performed in the

same manner as in the previously discussed study, namely with large quantities of worms. Summarized heat production measurements, depending on the worm age and normalized by protein content, are shown in Fig. 2.4. Interestingly, the authors have measured the heat production of larval and adult worms, and have concluded that larval worms have higher heat production rates than adult worms, after the results were normalized with respect to the protein content of the whole worm populations (black line). Additionally, they have measured the dauer recovery upon feeding (inset plot). Full metabolic activity after up to 3 weeks of diapause is reached after about 3 h. In this study however, the precision of the instruments precluded further conclusions during larval development.

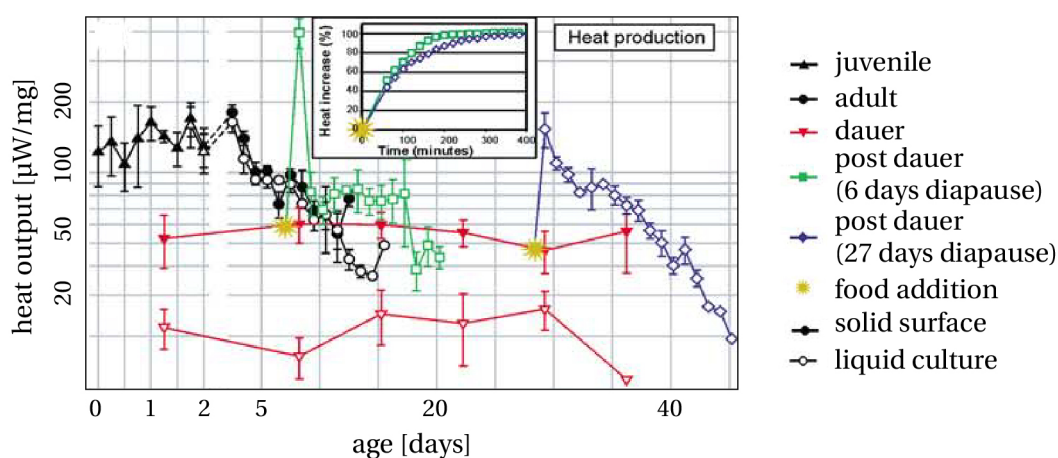


Figure 2.4 – Age-dependent metabolic heat of *C. elegans* populations measured by IMC. Reproduced and adapted with permission from [59].

2.2.3 Chip calorimetry for biological applications

Currently, miniaturized devices based on microfabricated heat sensors are emerging to overcome limitations of commercial IMC equipment. For instance, these chip calorimeters enable the thermal characterization of pl to µl-sized droplets in mixing experiments with sensitivities down to the nW-range, faster thermal response times and higher throughput [74, 75, 76, 77]. Other devices based on microelectromechanical systems (MEMS) sensors have been developed to enable more sophisticated experiments to be performed, such as IMC or continuous monitoring of enzyme reactions, while maintaining high sensitivity and fast response times [78, 79, 80, 81]. To improve fluid handling and further reduce sample consumption in isothermal experiments, microfluidics was implemented in some devices [82, 83, 84].

Although many measurements with living samples in large quantities have been performed in commercial microcalorimeters (Tab. 2.1, section 2.2.1), few biological studies have been performed in highly specialized calorimetric equipment with small sample sizes and/or

2.3. Theoretical principals of heat conduction calorimeters

microfluidic channels. An interesting application is the use of chip-based calorimeters as biosensors for the characterization of biological processes, such as enzyme activity [67, 61, 68].

Notably, Lerchner *et al.* developed a highly sensitive thermopile-based device for the study of metabolic heat of living organisms [85, 86, 87]. Two nested thermostats with separate proportional-integral-derivative (PID) controllers reduce thermal fluctuations near the thermopile to under 40 μK , which allowed stable baseline voltage signals with noise lower than 10 nW. In this device, the sample size was only 6 μL . They measured the heat production rates of *Pseudomonas putida* biofilms (0.13 pW per cell), *Staphylococcus aureus* (1.8 pW per cell) and zebrafish embryos (200 nW per embryo). Further studies on biofilms with a focus on antibiotic resistance have been performed [88, 89, 90]. In later iterations of the device, a segmented flow protocol has been implemented. The poly(methyl methacrylate) (PMMA) measurement chamber was replaced with a teflon tubing, which allowed the application of sequential measurements of flow plugs containing biofilms grown on glass beads or solid soil samples in volumes down to 10 μL . [91, 92].

2.3 Theoretical principals of heat conduction calorimeters

This section discusses the theoretical background of heat conduction calorimeters as they are implemented in most commercial devices and many chip-based calorimeters, including the device presented in the frame of this work. In heat flow calorimeters, a heat exchange between the sample vessel and a surrounding heat sink is allowed, as opposed to adiabatic calorimeters, where the temperature increase of an isolated sample vessel is measured. The temperature of the heat sink is kept as stable as possible using a thermostat surrounding the sample vessel. Heat generated in the sample flows towards the heat sink and is usually conducted through a sensing element that converts heat flow to a potential difference $V_{TP}(t)$ that is measured by a voltmeter. Chip calorimeters usually take advantage of microfabricated thermopiles, *i.e.* arrays of serially connected thermocouples fabricated on thin membranes with thicknesses ranging from tens of nm to tens of μm [93, 75, 94, 95]. Low heat capacity and high thermal resistance are key properties of the membrane material that permit the measurement of fast processes and small samples [61].

The Seebeck effect causes an electromotive force in a conductive material placed in a temperature gradient [96]. This leads to the formation of an electric potential difference at the interface of two different materials. An illustration of a single thermocouple made of two materials A and B is shown in Fig. 2.5a. A thermal gradient ΔT , where the material junction of the thermocouple is placed on the hot side and the ends of the wire on the cold side, results

in the thermocouple voltage V_{TC} across the two cold ends. When multiple (number = n) thermocouples are connected in series (Fig. 2.5b), the total thermopile output voltage V_{TP} over the cold junctions is equal to:

$$V_{TP} = n \cdot V_{TC}. \quad (2.1)$$

In heat conduction calorimeters, the thermopile sensors are integrated in a way that the hot junctions are in contact with the heat-generating sample. The cold junctions are in contact with a large thermal mass at a fixed, constant temperature. This heat sink is controlled by a precise thermostat to guarantee optimal thermal stability in the device. In such controlled conditions, where the temperature of the cold junctions is fixed and the heat produced by the sample flows exclusively through the thermopile, Tian's equation is used to convert the potential difference $V_{TP}(t)$ to the heat power P [97]:

$$P = PS \cdot \left(V_{TP} + \tau \frac{dV_{TP}(t)}{dt} \right), \quad (2.2)$$

where PS is the heat power calibration factor and τ is the time constant of the heat transfer between the sample and the sensor. In steady-state heat flow conditions, the equation simply becomes:

$$P = PS \cdot V_{TP}, \quad (2.3)$$

i.e. the heat power is directly proportional to the thermopile voltage $V_{TP}(t)$ with a factor PS , which can be determined by means of a calibration experiment.

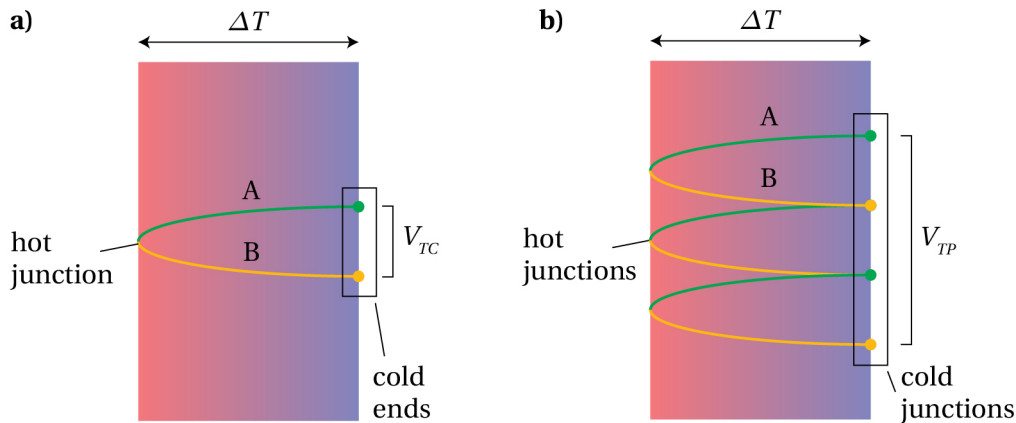


Figure 2.5 – Thermopile principle of operation. **a)** Illustration of a thermocouple junction made of materials A and B in a thermal gradient. An electric potential is generated between the hot and cold junctions of the two materials. **b)** n thermocouples connected in series (example $n = 3$) produce an output voltage $V_{TP} = n \cdot V_{TC}$. Based on [98].

2.4 Microfluidic chip fabrication

Standard soft lithography was used to fabricate two kinds of microfluidic chips designed for integration in the custom developed nanocalorimetry setup for different applications. One chip was used developed for the calibration of the thermopile sensors and for mixing enthalpy measurements, the other chip was applied for *C. elegans* metabolic heat measurements.

2.4.1 Mask fabrication

The microfluidic chip designs were drawn in the CleWin4 layout editor. The photomask fabrication process was reproduced from the EPFL Center of MicroNanoTechnology (EPFL-CMi) standard process flow and performed in the cleanroom facilities. The fabrication process is illustrated in Fig. 2.6. A blank $12.7\text{ cm}^2 \times 12.7\text{ cm}^2$ photomask (Nanofilm, USA) consisting of a glass plate covered by a 90 nm thin chromium layer and a 500 nm layer of AZ1518 positive photoresist was mounted into a high speed pattern generator (VPG200, Heidelberg Instruments, Germany). After importing the CleWin design files to the maskless laser lithography system, the patterns were written into the blank masks photoresist layer by a focused laser beam ($\lambda = 355\text{ nm}$) (Fig. 2.6a and b). The photoresist (PR) development using diluted AZ351 3.75:1 (Clariant, Germany), the chromium etch and the PR strip processes were done in an automated mask processor (Hamatech HMR900) (Fig. 2.6c - e).

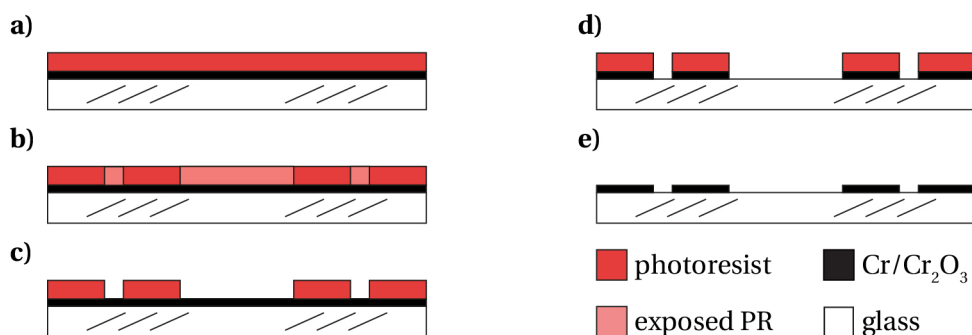


Figure 2.6 – Illustration of the mask fabrication process. **a)** 5 inch \times 5 inch photomask blank (Nanofilm, USA) consisting of a glass plate with a thin chromium layer on one side, which is covered by a layer of positive PR. **b)** Direct laser-writing of the custom mask patterns by an automated high-precision laser source. **c)** Development of the exposed PR. **d)** Wet etch of the chromium layer parts which are exposed to the etchant. **e)** Stripping of the remaining PR.

2.4.2 SU-8 master fabrication

Silicon wafers (<100>/P/SS/0.1-100, single-side polished wafers with $d = (100.0 \pm 0.5)\text{ mm}$ and $t = (525 \pm 25)\text{ }\mu\text{m}$) were provided by the EPFL-CMi and MicroChem GM3025 and GM3050 SU-8 negative photoresist was acquired from micro resist technology GmbH (Berlin, Germany). The mold fabrication process was performed in the EPFL-CMi cleanroom facilities using a

slightly adapted version of their standard SU-8 fabrication process. If not otherwise stated, parameters for spin-coating, bake temperatures/durations and exposure parameters were taken from the EPFL-CMi standard process flow. The mold fabrication process is illustrated in Fig. 2.7.

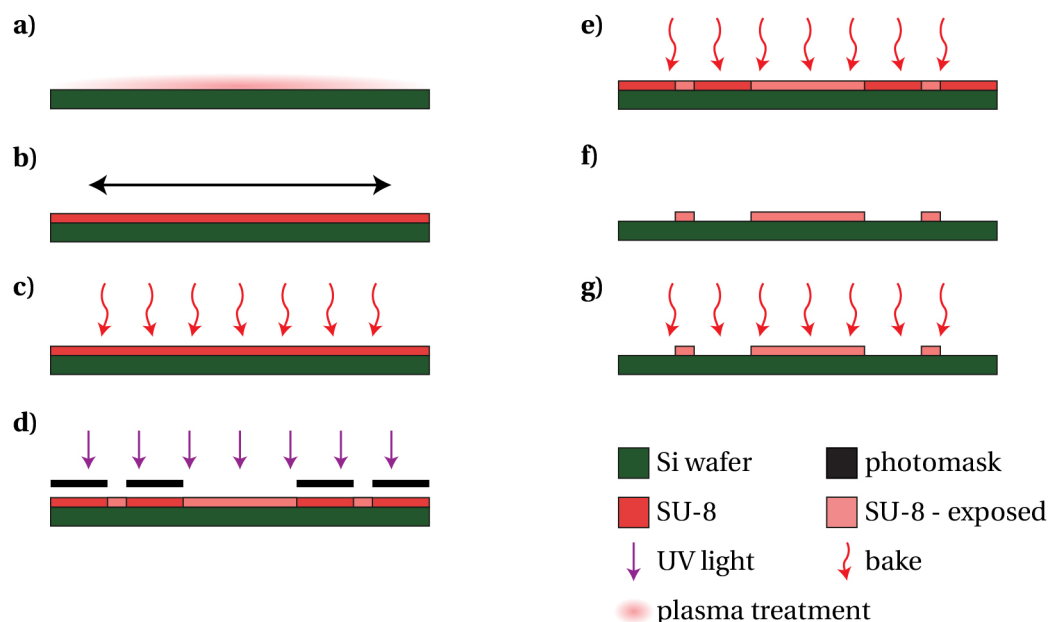


Figure 2.7 – Illustration of the SU-8 master fabrication process. **a)** A blank 4 inch silicon wafer is treated with oxygen plasma for cleaning and to improve resist adhesion. **b)** Spin-coating of the negative SU-8 photoresist on the wafer. **c)** Softbake of the SU-8 photoresist. **d)** Exposure of the SU-8 with UV light using the photomasks fabricated according to Fig. 2.6 **e)** Post-exposure bake of the SU-8 photoresist. **f)** Stripping of the non-exposed SU-8 photoresist. **g)** Hardbake of the patterned SU-8.

An array of 8 mm × 8 mm sized microfluidic chip structures were fabricated in SU-8 patterns on a Si wafer by photolithography. Blank Si wafers were oxygen plasma-treated for at least 4 min in a TePla 300 microwave plasma system (PVA TePla, Germany) to clean the wafer surface and to improve PR adhesion (Fig. 2.7a). Subsequently, SU-8 structural PR was spin-coated using a LSM200 (Sawatec, Switzerland) automated coater (Fig. 2.7b). After the coating, the wafers were rested for at least 10 min to help planarize the SU-8 layer. The SU-8 was soft-baked on a LSM200 programmable hot plate (Sawatec, Switzerland), slowly ramping up to a final temperature of 90 °C (Fig. 2.7c). The exposure of the SU-8 using a patterned photomask was done with either a MA6 or a MJB4 mask aligner (Süss MicroTec, Germany). In these machines, the coated Si wafer is first centered beneath the photomask, then brought in close contact to each other. A UV lamp ($\lambda = 365 \text{ nm}$) causes a crosslinking reaction in the SU-8 where exposed to the UV light (Fig. 2.7d). A post-exposure bake is then performed on a LSM200 hot plate (Sawatec, Switzerland) at a temperature of 90 °C (Fig. 2.7e). For PR development, the wafers were suspended upside-down in a propylene glycol methyl ether acetate (PGMEA) bath, then

rinsed alternating with PGMEA and isopropyl alcohol (IPA) until the resist was completely removed (Fig. 2.7f). Finally, the mold fabrication was ended with a hard bake of the developed SU-8 structures for 2 h at 135 °C. This step hardens the photoresist, improves photoresist adhesion to the Si wafer and cures the presence of small cracks that occur mostly on larger SU-8 surfaces.

2.4.3 Chip assembly

Float glass wafers ($d = (100.0 \pm 0.3)$ mm and $t = (550 \pm 10)$ μm) were provided by the EPFL-CMi. Poly(dimethylsiloxane) (PDMS) Sylgard 184 was purchased from Dow Corning (Wiesbaden, Germany). Trimethylchlorosilane (TMCS) was acquired from Sigma Aldrich (Buchs, Switzerland). The chip assembly was performed in the EPFL-CMi cleanroom facilities. A PMMA mold was fabricated by the EPFL Atelier de l'Institut de microtechnique (EPFL-ATPR) by computerized numerical control (CNC) milling to define the outer shape and size ($h \approx 5$ mm, $l = 8$ mm, $w = 8$ mm) of the PDMS chips that is required for fitting into the ceramic frame of the sensor membrane. The wafer containing the SU-8 patterns as well as the aluminium mold and a float glass wafer were treated with TMCS for 15 min in a vacuum desiccator to avoid PDMS adhesion upon demolding. The fluidic channels on the wafer were aligned with the PMMA mold and clamped together with 4 large paper binder clips. PDMS was prepared by mixing a 10:1 ratio of elastomer to curing agent and subsequent degassing in a vacuum chamber for 10 min. The mixed PDMS was then poured over the wafer PMMA-mold assembly (Fig. 2.8a). After curing the fluidic chips in an oven at 80 °C for 1 h (Fig. 2.8b), the PDMS was demolded from the Si wafer, while keeping the PMMA mold in place for punching inlet holes with a 0.75 mm diameter biopsy punch (World Precision Instruments Ltd., USA) for the connection fluidic tubing (Fig. 2.8c). Subsequently, the PDMS chips were removed from the PMMA mold. At the same time, PDMS was spin-coated at 3000 rpm on a TMCS treated float glass wafer to obtain an approximately 20 μm thick PDMS membrane, which was then cured at 80 °C for 1 h (Fig. 2.8e, f). Subsequently, the fluidic structures on the PDMS chip were sealed onto the PDMS membrane by oxygen plasma bonding (Fig. 2.8g). With this method, 24 individual chips were fabricated from one Si wafer and molded at the same time. Tygon flexible plastic tubing (ID 0.25 mm, OD 0.75 mm, EW-06420-01, Cole Parmer, USA) was used for the fluidic connections (Fig. 2.8h). Individual chips can be demolded from the float glass wafer before each experiment (Fig. 2.8i). A photograph of a single chip placed on a glass slide is shown in Fig. 2.9.

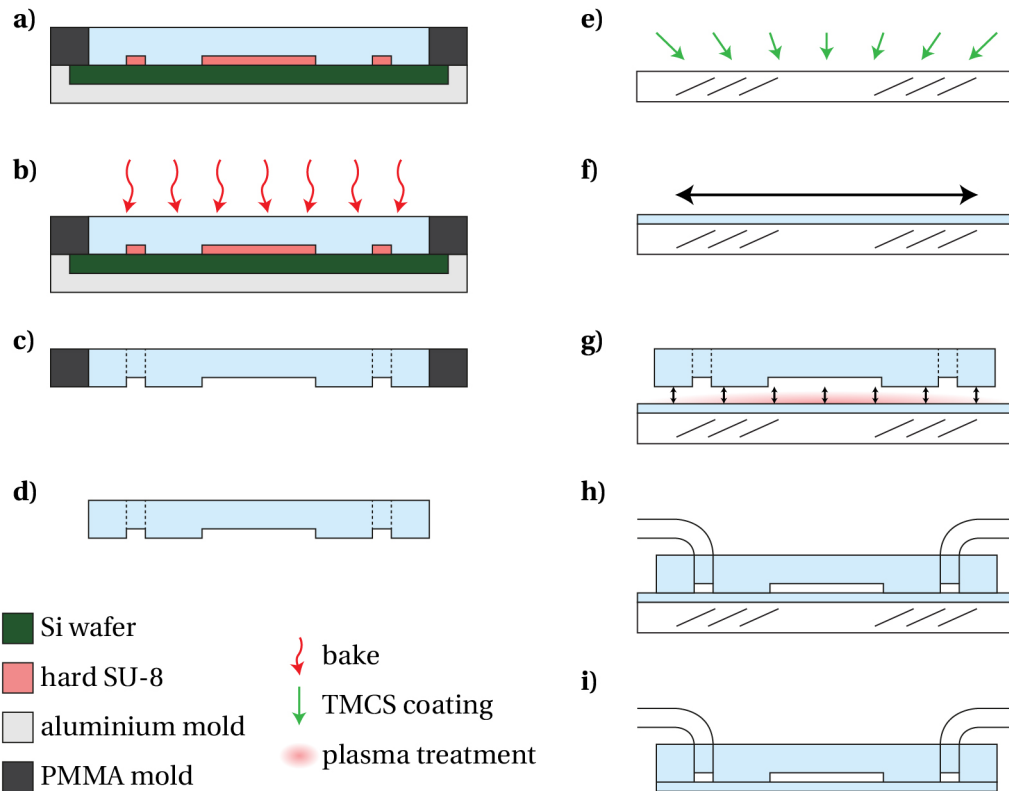


Figure 2.8 – Full wafer scale PDMS microfluidic chip fabrication and assembly process. **a)** A custom 2-part mold consisting of a bottom aluminium wafer holder and a top PMMA part to shape the outer dimensions of the final chip is used for the PDMS replica molding. The wafer is clamped between the two parts, and liquid PDMS is subsequently poured over the SU-8 patterns. **b)** The PDMS is cured at 80 °C for at least 1 h. **c)** Demolding of the top PMMA part of the mold and the PDMS chips. Inlet holes are punched using a 0.75 mm diameter tissue punch. **d)** Demolding of the chips from the PMMA mold. **e)** Silanization of a float glass wafer by exposure to TMCS under vacuum. **f)** Spin-coating of a $\approx 20 \mu\text{m}$ thick PDMS membrane on the glass substrate. **g)** Oxygen plasma bonding of the PDMS membrane to the demolded chips from step **d**. **h)** Insertion of the connective tubing into the previously punched inlet holes. **i)** Manual cutting of the PDMS membrane around the chip and lift-off of the sealed chip.

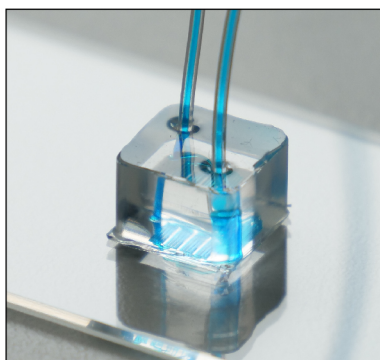


Figure 2.9 – Photograph of the final chip on a glass slide. The chip outer dimensions are $8\text{ mm} \times 8\text{ mm}$ with a height $h \approx 5\text{ mm}$). A dye solution has been introduced into the channels to visualize the microfluidic channels.

2.5 Microfluidic nanocalorimetry system

2.5.1 Description of the nanocalorimetric system

The nanocalorimetric system is based on a single-channel system that was previously developed in our laboratory [78, 98]. This system featured a PMMA sample reservoir (volume $\approx 50\ \mu\text{l}$) on top of the thermopile sensor and thus did not allow accurate fluidic control. A limit of detection (LOD) of $0.17\ \mu\text{W}$ was determined by a 1-propanol/water mixing experiment. Here, we present a more advanced system for the use with microfluidic protocols. Two identical and independent sensors have been incorporated in a redesigned calorimetric system, enclosing them under well-defined and equal environmental conditions for conducting parallel experiments. The new system comprises three main components: (i) two commercial thermopile sensors (XEN NCM9924, Xensor Integration, Delft, The Netherlands), (ii) a microfluidic chip directly placed on top of each thermopile sensor, and (iii) a highly accurate thermostat. The sensors feature a silicon–aluminum thermopile on a $22\ \mu\text{m}$ thick $8\text{ mm} \times 8\text{ mm}$ Si membrane, perimetrically distributed around a $4\text{ mm} \times 4\text{ mm}$ sensitive area in the center of the membrane (Fig. 2.10) [99]. The voltage signals generated by the thermal sensors are recorded by a two-channel nanovoltmeter (34420A, Keysight, USA) using custom LabVIEW (National Instruments, USA) software.

An exploded three-dimensional (3D) view of the final calorimetric platform is shown in Fig. 2.11. The microfluidic chips are designed in a way that all fluidic structures (channels or chambers), in which heat is expected to be generated, are in close contact with the sensitive area of the sensor. By sealing the channels with a thin PDMS membrane, fast heat transfer between chip and heat sensing sensor membrane can be achieved (Fig. 2.12). Fluidic control is provided by external high-precision syringe pumps (neMESYS Low Pressure syringe pump, Cetoni GmbH, Germany).

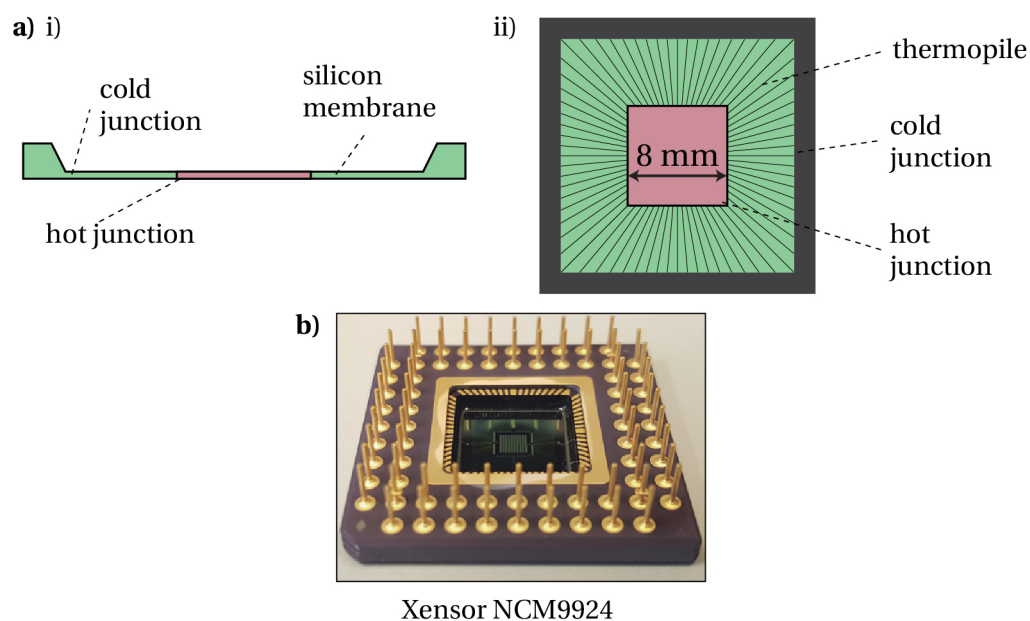


Figure 2.10 – Visualization of the commercial thermopile chip used for the calorimetric platform (Xensor NCM9924). **a)** Schematic cross-sectional view (i) and top-view (ii) of the thermopile sensor. The Si–Al thermopile is arranged radially around a 4 mm × 4 mm square area in the center of a 22 μm thick suspended monocrystalline silicon membrane. **b)** Photograph of the sensor.

The thermostat is built up from an Al block, enclosed by a polystyrene housing. Both sensor chips are clamped onto the Al block via their ceramic frame, thus providing a stable heat sink at the cold junctions of the thermopile (Fig. 2.11a). Several heating pads (2 × HK6912 and 4 × HK6917, not shown in Fig. 2.11a, Minco Products, USA) and a temperature sensor (Pt1000, Innovative Sensor Technology AG, Switzerland) connected to a temperature controller (Model 335, LakeShore, USA) build up the PID feedback loop. A schematic cross-sectional view of the microfluidic nanocalorimetric setup is depicted in Fig. 2.12.

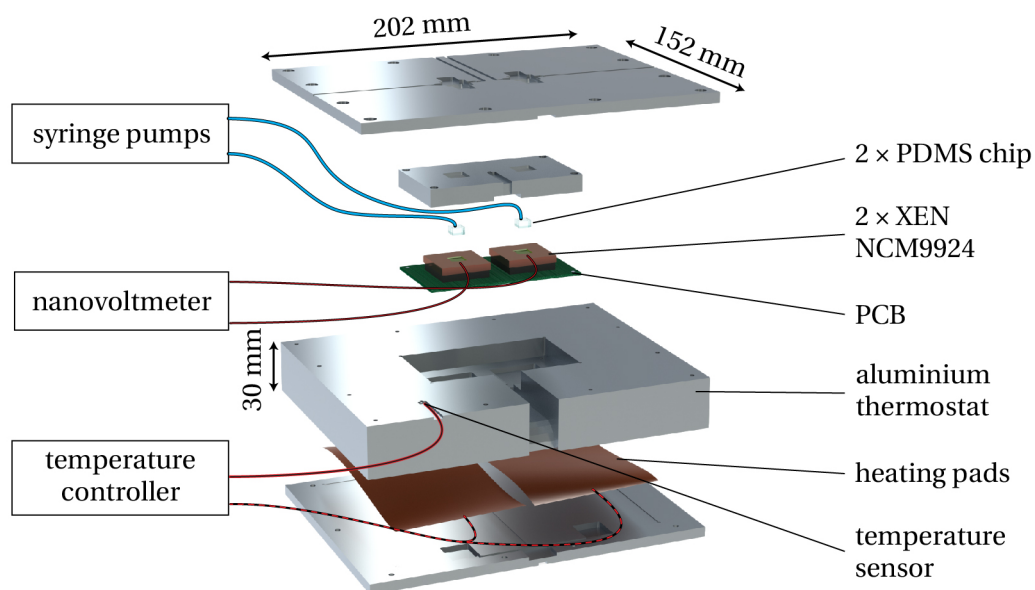


Figure 2.11 – 3D model of the nanocalorimetric system. **a)** Exploded 3D view of the integrated dual-nanocalorimeter device. The aluminium thermostat accommodates two thermopile sensors with microfluidic chips. Components for PID temperature control (Pt1000 temperature sensors and heating pads), signal readout (nanovoltmeter) and automated fluidic control (two syringe pumps) are integrated or connected to the device. **b)** Schematic cross-sectional view showing positioning of one of the two microfluidic chips on top of the sensor and fluidic connections. The Al thermostat is placed in a polystyrene box (not to scale).

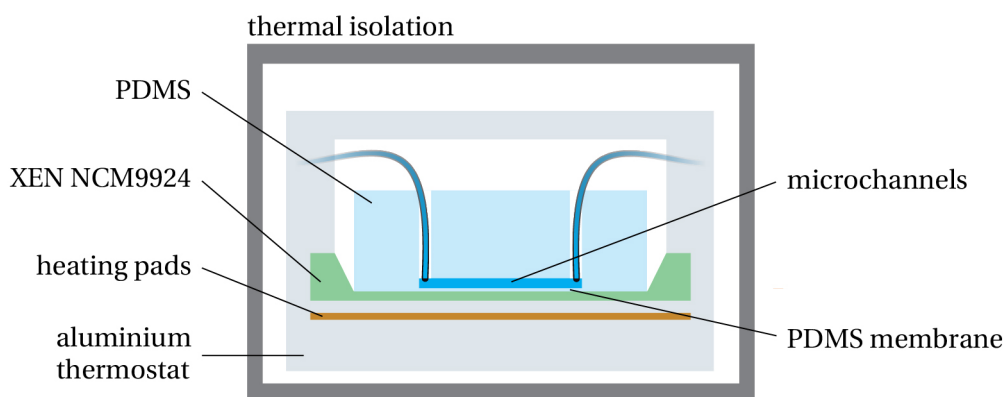


Figure 2.12 – Schematic cross-sectional view of the calorimetric system. The figure shows the positioning of one of the two microfluidic chips on top of the sensor and fluidic connections. The Al thermostat is placed in a polystyrene box (not to scale).

2.5.2 Sensor calibration

Calibration of the thermopile sensor was performed using a microfluidic chip to mimic the heat transfer conditions during experiments as closely as possible. The PDMS microfluidic chip shown in Fig. 2.13 was used for calibrating the voltage *vs.* heat power response of the thermopile sensor based on mixing enthalpy measurements. The specific design of this calibration chip features a single long meander-shaped channel ($l \approx 19$ cm, $w = 100$ μm , $h = 50$ μm) with two inlets (In1 and In2) and one outlet (Out), allowing diffusive mixing of two injected liquids in collinear streams. The channel structure fully covers the 4 mm \times 4 mm sensitive area of the sensor membrane. Simultaneous and continuous injection of two sample solutions generates a steady heat signal that is measured by the thermopile and transduced to a voltage signal $V_{TP}(t)$, corresponding to the enthalpy of mixing produced over the length of the channel. The highest signal is expected when flow parameters are adjusted such that full mixing occurs close to the channel outlet. This situation is depicted in the two photographs of Fig. 2.13, where the laminar flow of two dye solutions close to the inlets and full diffusive mixing at the outlet is shown. This condition is fulfilled for a mixing flow rate $v_{mix} = 0.1$ $\mu\text{l/s}$, corresponding to a Peclet number $Pe \approx 2000$ and a Reynolds number $Re \approx 1$, assuming a diffusion coefficient $D = 1 \times 10^{-9}$ m^2/s for dye molecules in aqueous solution.

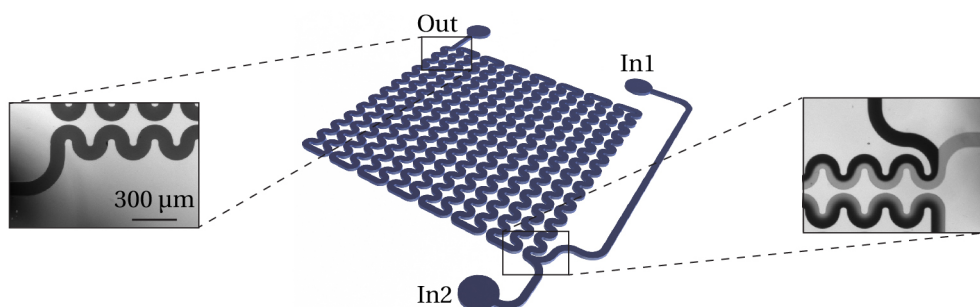


Figure 2.13 – Fluidic chip for the calibration of the thermopile sensor. The microfluidic chip with a serpentine channel ($l \approx 19$ cm, inlets In1 and In2, outlet Out). The photographs show the parallel laminar flow pattern of two injected dye solutions close to the inlets and full diffusive mixing close to the outlet.

The sensor was calibrated by taking advantage of the well-known mixing parameters of IPA and DI water. IPA and DI water were continuously injected into the mixing channel through In1 and In2 for 7 min, during which the corresponding $V_{TP}(t)$ signal was recorded. Subsequent aliquots were injected at different mixing ratios (7 min for each condition), which were obtained by varying the respective flow rates at the inlets, while keeping the total flow rate constant at v_{mix} . Diffusive mixing of the liquids at different ratios gave rise to a series of $V_{TP}(t)$ peaks with different amplitudes. The signal trace of a complete sequential mixing experiment is shown in Fig. 2.14a (blue curve). Each peak is generated by full diffusive mixing at different mole fractions of IPA X_{IPA} (indicated as red cross for each peak in Fig. 2.14a). The V_{TP} peak area A_{TP}^M under each peak, which is related to the corresponding mixing enthalpy, was calculated by integration with respect to time and divided by the total number of moles

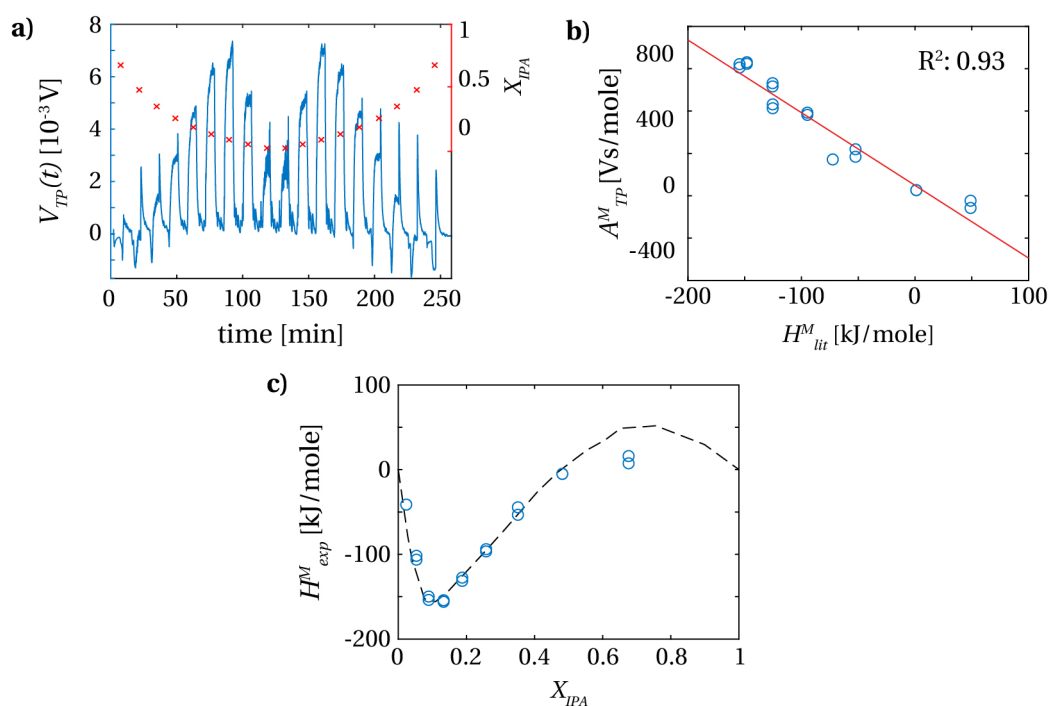


Figure 2.14 – Calibration of the thermopile sensor based on mixing enthalpy measurements. **a)** thermopile voltage $V_{TP}(t)$ of a typical calibration experiment. Different ratios of isopropyl alcohol IPA and deionized water (DI water) have been injected sequentially for 7 min. Between each aliquot, the flow was stopped for 7 min, during which $V_{TP}(t)$ is approaching the baseline (≈ 0 V). Red crosses in (a) indicate the IPA molar fraction X_{IPA} (right axis). **b)** The area A_{TP}^M for each $V_{TP}(t)$ peak in (a) divided by the number of moles of liquid flown through the channel is plotted *vs.* mixing enthalpy values H_{lit}^M reported in ref. [100]. The heat power calibration factor PS was determined by linear regression (red line, $PS = 3.4$ V/W). **c)** Experimental molar mixing enthalpy H_{exp}^M (blue circles) and H_{lit}^M values of Lama *et al.* (dashed line) as a function of X_{IPA} [100].

in each aliquot. In Fig. 2.14b, the resulting values are plotted *vs.* the corresponding literature molar mixing enthalpy H_{lit}^M values taken from Lama *et al.* [100]. These H_{lit}^M values, which were obtained by mixing IPA and DI water in ml-size ampoules (8 ml to 15 ml) in brass calorimeters, thus can be considered as a reliable reference for our measurements. Finally, we derived a heat power calibration factor $PS = 3.4$ V/W for our device by linear regression of the data points in Fig. 2.14b (red line, $R^2 = 0.93$). In Fig. 2.14c, the resulting experimental molar mixing enthalpy values H_{exp}^M (using $H_{exp}^M = A_{TP}^M / PS$) are plotted as a function of X_{IPA} (blue circles) and compared to literature values derived from ref. [100] (dashed line). Comparing the calibrated experimental enthalpy values with the curve in ref. [100] shows good overall agreement.

A prerequisite for many applications, especially for drug screening, are high-throughput measurements of mixing enthalpies, for example the characterization protein-ligand binding. Several chip-based approaches have been proposed, however, a device combining enhanced throughput and high sensitivity, has not been proposed so far [80]. The presented calibration method of our chips acts at the same time as a device that can be used to characterize

binding reactions of many liquid samples and using only minute volumes in the μl -range, which results in a significant reduction of cost when comparing the required sample volumes to common volumes used in commercial calorimeters (ml-range). The sequential sample injection allows multiplexed generation of various assay conditions, has high potential for a variety of applications, including drug discovery processes, detection of enzymatic reactions and biological experiments.

2.5.3 Worm chip design

The microfluidic worm chamber for the *C. elegans* nanocalorimetric assays is displayed in Fig. 2.15. It comprises an arrangement of 16 parallel chambers ($h = 65\ \mu\text{m}$) covering the $4\ \text{mm} \times 4\ \text{mm}$ sensitive area of the thermopile sensor. This configuration allows for uniform flow and worm population distribution. Furthermore, this compartmentalization prevents the thin PDMS membrane from bulging. PDMS filter structures ($5\ \mu\text{m}$ spacing) facing the chip outlet confine larval worms from the early L2 to the late L4 stages in the chambers upon application of an external flow. Worm suspension, media and treatment agents are supplied through the inlet of the chip by suction from the outlet.

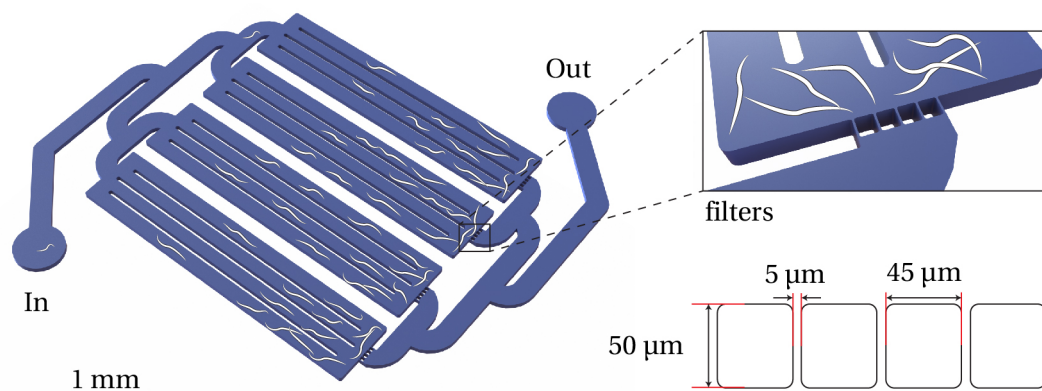


Figure 2.15 – Microfluidic chip for nanocalorimetric assays of *C. elegans* larval populations. The worm chip comprises a parallel arrangement of 16 trapping chambers ($w = 200\ \mu\text{m}$, $h = 65\ \mu\text{m}$, $l = 3.8\ \text{mm}$). Worm populations or compounds were injected through the inlet (In). Worms were confined in the chambers by on-chip PDMS filter structures at the chamber side facing the chip outlet (Out) (filter spacing $5\ \mu\text{m}$, see enhanced view).

2.6 Experimental

2.6.1 *C. elegans* age-synchronization

NGM agar plates, *E. coli* OP50 and S-Basal medium were prepared following standard protocols [22]. *C. elegans* N2 wild type worms were obtained from the Caenorhabditis Genetics Center (CGC). The worm populations were cultured at room temperature on NGM agar plates together with *E. coli* OP50 as food source [2]. Age-synchronized worm populations were obtained by isolating eggs with a bleaching procedure (adapted from Stiernagle *et al.* [22]). The bleaching solution was prepared by mixing 0.33 ml 4 mol/L NaOH, 1 ml 10 % solution of sodium hypochlorite and 3.66 ml DI water. Embryos were isolated by flushing the bleaching solution over an agar plate containing gravid hermaphrodites, collecting the suspension in an Eppendorf tube, and vortexing every 2 min for about 8 min, or until the worms are dissolved. To retrieve the eggs from the bleaching solution, repeated centrifugation at ≈ 1680 rcf for 60 s was performed, replacing the supernatant by 1 ml of S-Basal, and re-suspending the eggs by vortexing. A synchronized worm population was obtained by maintaining isolated eggs in S-Basal overnight until hatching, and distributing the arrested L1 larvae on agar plates containing a lawn of *E. coli* OP50. The worms were then collected for the experiments after 12 h, 24 h and 48 h by washing over the plate with S-Basal, corresponding to the early L2, L3 and late L4 stages, respectively.

2.6.2 Metabolic heat measurement protocol

The initial worm loading procedure before performing a nanocalorimetric assay is depicted in Fig. 2.16a. A PDMS chip prefilled with S-Basal was placed on a glass slide. A synchronized worm suspension, comprising 60 to 220 organisms, was then loaded into the chip. Subsequently, the microfluidic chip was transferred onto the thermopile sensor, fixed on the Si sensor membrane by self-adhesion and connected to the syringe pump.

During the on chip metabolic assays, the synchronized worm populations were treated with the mitochondrial uncoupling agent FCCP, purchased from Sigma-Aldrich (Buchs, Switzerland). A stock of 10 mmol/L FCCP in dimethyl sulfoxide (DMSO) was prepared from the powder, then kept frozen in aliquots. Before a calorimetric experiment, FCCP stock solution was added to S-Basal media to a concentration of 30 $\mu\text{mol/L}$ to be used for the worm treatment.

A typical experiment for monitoring the effect of a biochemical agent on the metabolic heat output of a worm population takes approximately 4 h. This duration includes thermal stabilization of the thermostat and the chip, application and incubation of the active compound, and the quantification of the heat power of the worm population before and after treatment. Temperature stabilization at a set point of 25 °C, after closing the outer polystyrene housing

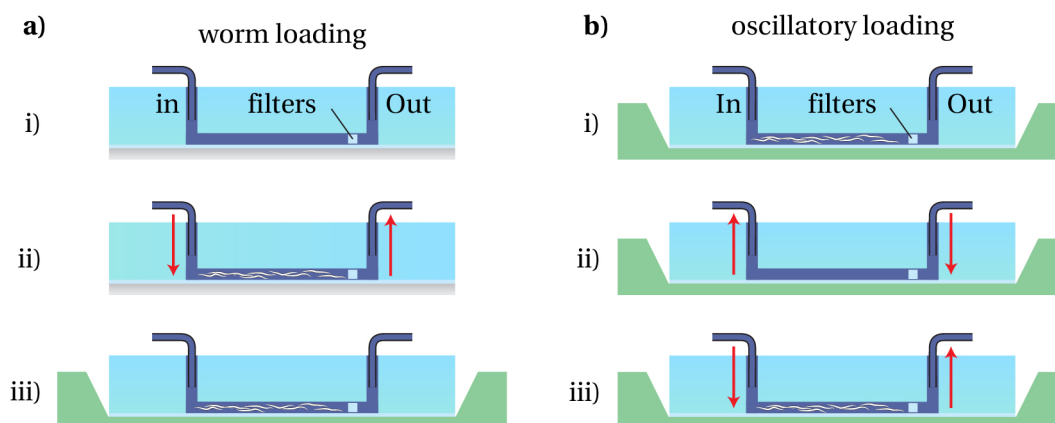


Figure 2.16 – Worm loading and oscillatory loading for metabolic assays of *C. elegans* larval populations. **a)** Cross-section of the chip depicting the initial worm loading: the PDMS chip was placed on a glass slide (i), and filled with a synchronized *C. elegans* population of up to 220 worms under microscope control (ii). Subsequently, the chip was transferred on the sensor membrane (green) and enclosed in the thermostat of the nanocalorimeter (iii). **b)** Cross-section of the chip showing the oscillatory flow protocol during the assay: for measuring metabolic heat, the worm suspension remained stationary (no flow) on the sensor area (i). For reference measurements, worms were pushed into a connecting tube by filling the chambers with buffer solution (ii). Subsequently, the worm population was sucked back onto the sensitive area of the chip to perform the next metabolic heat measurement (iii).

of the thermostat, takes about 90 min. After this period, the temperature variation of the Al holder is in the range of ± 1 mK and a stable baseline $V_{TP}(t)$ in the range of ± 2 μ V over 60 min is obtained.

For the accurate measurement of the metabolic heat power generated by a *C. elegans* population, we take advantage of the oscillatory loading cycle protocol depicted in Fig. 2.16b. The entire worm population is pushed out of the chip into the connecting tube (flow of 50 nl/s, applied from the outlet for 100 s) and subsequently pulled back into the on-chip worm chamber (flow of -50 nl/s, applied for 200 s). The procedure is repeated 3 times for each condition. In this way, the metabolic heat source is periodically removed from the thermopile sensor and replaced by buffer solution, resulting in a $V_{TP}(t)$ voltage sequence of alternating heat and baseline signals. We analyze the differential signals of such sequences that correspond to the metabolic heat generated by the on-chip worm population. A thermal stabilization time lapse of 200 s is allowed after each fluidic transfer. Fig. 2.17 depicts a typical flow protocol used for the metabolic heat assays. During thermal stabilization (90 min, blue area in Fig. 2.17), a slow negative flow of -5 nl/s is applied to pull the worms gently against the filter structure facing the worm chamber outlet. This ensures that worms do not escape by swimming through the inlet of the chamber, where no filter structures have been implemented. Three loading/unloading steps are carried out before and after application of the active compound to determine the

impact on the metabolic heat of the worm population (total duration \approx 30 min for each sequence of 3 cycles, orange areas in Fig. 2.17). The compound for worm treatment was applied for 30 min (injection + incubation, red area in Fig. 2.17). This flow protocol is fully automated.

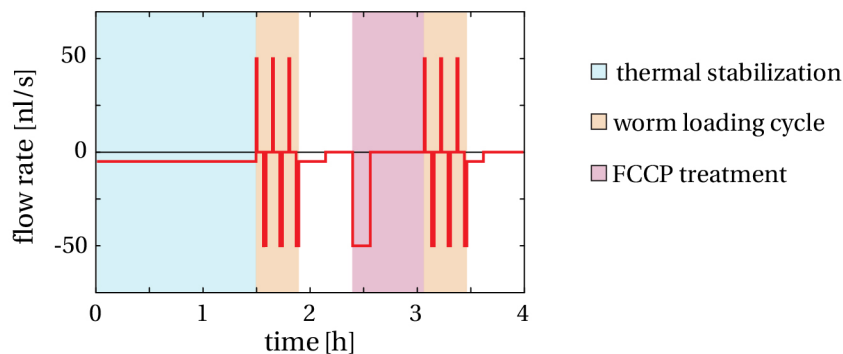


Figure 2.17 – Metabolic heat measurement flow protocol for worms treated with the uncoupling agent FCCP. The chart shows the flow protocol controlled by an external syringe pump. During thermal stabilization (90 min, blue area), a weak flow ensured that worms stay on the chip. A first oscillatory flow cycle (three subsequent loading/unloading steps, orange area) allowed measuring the heat signature of the untreated worm population. Subsequently, the chip was filled with medium containing FCCP, and the worm population was incubated for 30 min (red area). A second oscillatory cycle was performed to measure the heat signature after treatment (orange area).

2.6.3 Quantification of a worm population

For quantification of the worm populations, a stereomicroscope (Discovery V8, Zeiss, Germany) combined with a microscope camera (PL-B681C, Pixelink, USA) was used to acquire images of the worm chips. The image processing approach is shown in detail in Fig. 2.18. Images of the on-chip population were taken before mounting the chip on the thermopile sensors and after the experiment for verification. Background images without worms were subtracted from the sample images using MATLAB as processing software. For counting the worms of an on-chip population, the contrast of the foreground images could then be easily enhanced.

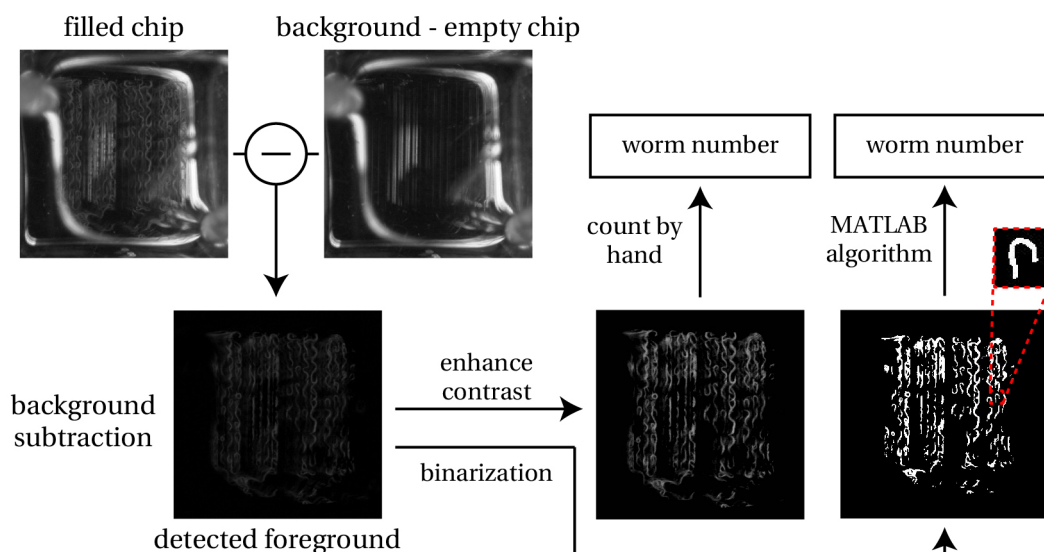


Figure 2.18 – Image processing for counting on-chip worm populations. Images of the microfluidic chips were taken after worm loading and compared to background images before worm loading (filled with buffer solution). MATLAB was used to subtract the background image from the image of a filled chip, yielding only the contribution of the worms (foreground). MATLAB was also applied to enhance the contrast and binarize foreground images (using MATLABs adaptive thresholding function with sensitivity = 0.05). On the processed images, worm populations can either be counted manually or estimated using MATLAB. In the later case, a rectangular area is manually drawn around a worm to find the number of white pixels making up single organism. This number of pixels is then divided by the number of white pixels in the whole binarized foreground image to estimate the total number of worms on-chip.

2.7 Results

Our microfluidic approach enables sensitive metabolic heat measurements of synchronized larval *C. elegans* populations and the application of active compounds on-chip, thus allowing quantifying metabolic heat variations upon worm treatment. For evaluating the basal metabolic heat of a worm population and in particular the response to FCCP, we recorded $V_{TP}(t)$ of different populations using the oscillatory protocol described in the experimental section (see Fig. 2.17 for the full protocol). Fig. 2.19a shows a typical $V_{TP}(t)$ sequence, resulting from the flow pattern depicted in the lower part of the figure, *i.e.* consecutive unloading/loading of the worm population for 3 times.

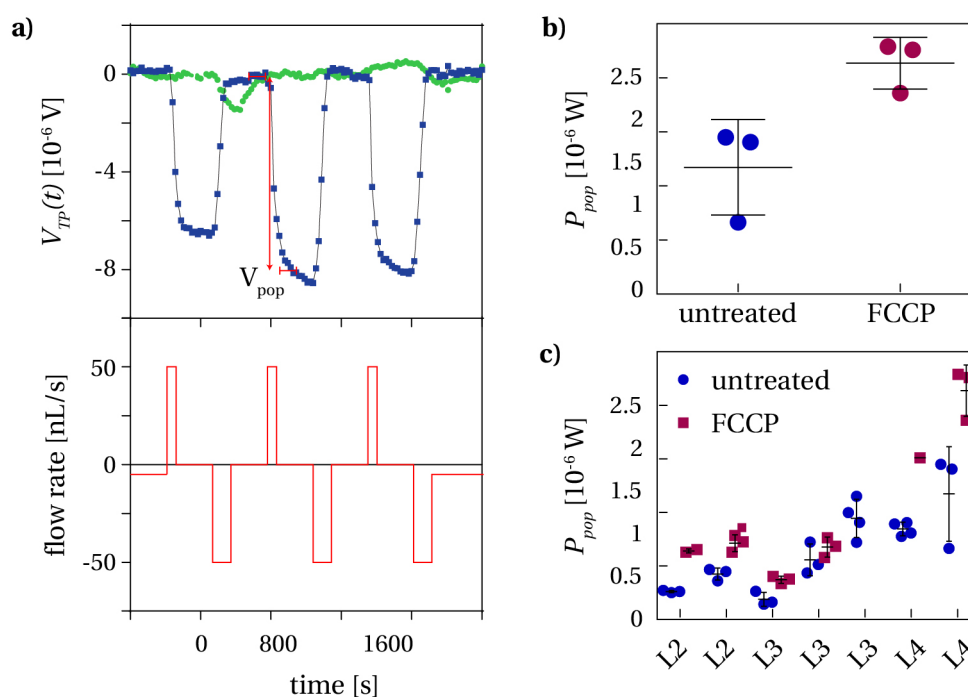


Figure 2.19 – Quantification of metabolic heat power of on-chip worm populations. **a)** Upper chart: representative $V_{TP}(t)$ signal sequence during an oscillatory cycle (blue curve) and corresponding control (no worms, green curve). The same flow protocol was applied in both cases. The effective heat signature of the on-chip worm population V_{pop} was determined by the $V_{TP}(t)$ signal difference right before (reference) and after (signal) a worm reloading step. Bottom chart: flow profile applied for loading/unloading the worm population onto the chip, matched to the $V_{TP}(t)$ sequence. **b)** Total metabolic heat power P_{pop} generated by a synchronized population of ≈ 220 worms in the L4 larval stage before (blue dots) and after FCCP treatment (red dots). Scattered data points correspond to the oscillatory loading cycles before (derived from Fig. 2.19a) and after FCCP treatment, respectively ($n = 3$). **c)** Individual data for each metabolic assay indicated in Tab. 2.2: total metabolic heat power P_{pop} ($P_{pop} = V_{pop}/PS$ with $PS = 3.4$ V/W) generated by an on-chip worm population before and after FCCP treatment. Data points represent P_{pop} values obtained by a typical loading/unloading cycle ($n = 3$), error bars represent mean \pm SD.

In this case, the signal sequence corresponds to a population of ≈ 220 worms in the L4 stage prior to FCCP treatment. Upon withdrawal of the worm population from the sensor area, *i.e.* temporary displacement into the connecting tubing, the thermopile response $V_{TP}(t)$ signal drops by a few μV , as the heat source was removed from the sensor surface. The $V_{TP}(t)$ signal rises again when the worm population is loaded back into the microfluidic chip and in contact with the sensitive area of the thermopile sensor. To reliably determine the contributed V_{pop} , *i.e.* the voltage difference corresponding to the worms' metabolic activity, V_{pop} was calculated by subtracting mean values of $V_{TP}(t)$ right before and after reloading the worms (averaged over a time lapse of 60 s in both cases). With this procedure, we reduce the impact of systematic errors (*e.g.* voltage drift after loading) on the signal of interest. Stereomicroscope images were taken after the initial worm loading step of each assay, from which the worm populations were quantified (see Section 2.6.3, and Fig. 2.18). As the optical access to the chip was obstructed by the thermostat during the assay, it was not possible to count the worms during an oscillatory measurement cycle. However, fluidic connections and manipulation were tested before each assay to ensure that the worm population can be reliably moved on and off the chip without further control and without loss of worms or clogging of the device.

From a signal sequence as shown in Fig. 2.19a, we can calculate the metabolic heat power signal of an on-chip worm population P_{pop} by means of the sensor calibration factor $PS = 3.4 \text{ V/W}$. Control measurements using the same flow profile, buffers and treatment agents, but no worm population, did not show significant $V_{TP}(t)$ modulations thanks to careful thermalization of media and low flow rates (Fig. 2.19a, green curve). Fig. 2.19b shows P_{pop} values obtained for a single assay prior to FCCP treatment (corresponding to Fig. 2.19a) and after FCCP treatment, where the full flow protocol was applied (Fig. 2.17). In this particular case, mean values \pm standard deviation (SD) indicate an increase in the metabolic heat from $(1.17 \pm 0.44) \mu\text{W}$ before to $(2.14 \pm 0.24) \mu\text{W}$ after FCCP treatment, respectively.

Assay	Larval stage	Worm age (hours)	Number of worms	FCCP treatment
1	L2	12	170	Yes
2	L2	12	100	Yes
3	L2	12	100	Yes
4	L3	24	135	No
5	L3	24	60	Yes
6	L4	48	220	Yes
7	L4	48	100	Yes

Table 2.2 – Metabolic heat assays performed in this work, using *C. elegans* populations of different larval stages. The worm count was done on processed stereomicroscope images (see Fig. 2.18).

Different assays were performed to evaluate the metabolic heat and the heat variation upon treatment with FCCP for *C. elegans* at different development stages, ranging from the early L2 to late L4 / young adult (YA) stage. Details on all individual assays performed in this work, including the exact age of the populations in hours and worm count, are provided in Tab. 2.2. P_{pop} data obtained from each individual assay is plotted in Fig. 2.19c. An additional control

assay to determine possible effects due to the maintenance of the worm population on the chip for several hours is presented in Fig. 2.20a. This experiment confirmed that the increase of the V_{pop} signals is indeed caused by the FCCP treatment and not due to long-term drifts. The slight decrease of V_{pop} values can be attributed to starvation and/or arrested development of the on-chip worm population. Representative $V_{TP}(t)$ signal sequences, which directly compare the sensor response before and after FCCP treatment, are shown in Fig. 2.20b.

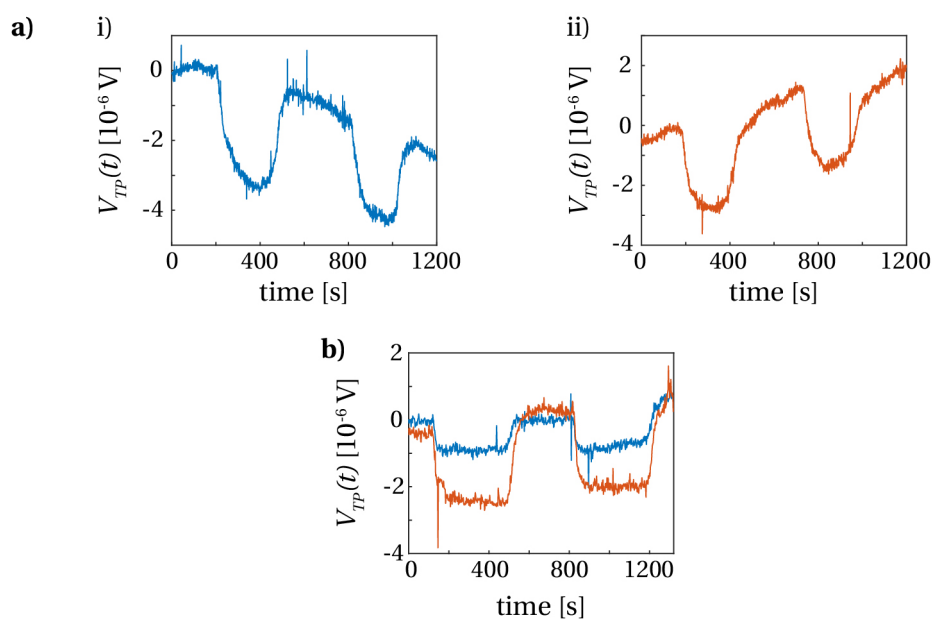


Figure 2.20 – Control measurements for metabolic assays. **a)** Long-term control experiment with L3 worms (for population information see Tab. 2.2, assay 4). ai) $V_{TP}(t)$ response of the oscillatory flow profile (2 cycles) after worm loading and 60 min thermal stabilization. V_{pop} values of $3.4 \mu\text{V}$ (cycle 1) and $3.1 \mu\text{V}$ (cycle 2) were calculated. aii) $V_{TP}(t)$ response of the oscillatory flow profile of the same untreated population after on-chip incubation for 8 h in buffer without bacterial food supply. V_{pop} values decreased slightly to $2.5 \mu\text{V}$ (cycle 1 and cycle 2). No baseline correction was applied in these cases. This control assay confirms that the measured increase in $P_{pop|FCCP}$ after FCCP treatment compared to the initial P_{pop} values is not due to a shift caused by long experiment durations, but by the FCCP treatment indeed. **b)** Representative $V_{TP}(t)$ response of a L2 worm population, before (blue curve) and after (red curve) FCCP treatment (for population information see Tab. 2.2, assay 1).

Fig. 2.21 summarizes the results and data analysis with respect to each larval stage. Fig. 2.21a shows the metabolic heat power normalized metabolic heat power per worm P_{worm} , obtained by dividing P_{pop} by the number of worms on the chip, before and after FCCP treatment for the early L2, late L3 and late L4 stages, respectively. P_{worm} corresponds to mean values \pm SD for each stage, based on the number of assays indicated in Tab. 2.2. This data reveals that the metabolic heat production per worm increases significantly from L2 to late L3, both without and with FCCP treatment. For untreated worms P_{worm} increases from (2.6 ± 1.3) nW at L2 to (6.9 ± 1.4) nW at L3, respectively (*i.e.* by a factor of ≈ 2.6) and remains nearly constant from L3 to L4 ((7.1 ± 1.9) nW for untreated L4). FCCP treatment increases the metabolic heat production per worm to (5.0 ± 1.7) nW at L2 (*i.e.* by $\approx 95\%$), to (11.3 ± 1.3) nW at L3 (*i.e.* by $\approx 63\%$)

and to (11.1 ± 2.5) nW at L4 (*i.e.* by $\approx 55\%$), thus generating a slightly lower relative increase in the latter case. Fig. 2.21b represents the corresponding absolute heat power per worm after FCCP treatment $P_{worm/FCCP}$, obtained by subtracting P_{worm} values before and after FCCP treatment, *i.e.* considering only the effect of the FCCP treatment. $P_{worm/FCCP}$ increases by (2.4 ± 0.8) nW for L2 and by (4.3 ± 1.1) nW for L3, respectively. Thereafter $P_{worm/FCCP}$ does not show a statistically significant variation with respect to L3 ((3.9 ± 1.5) nW, for L4).

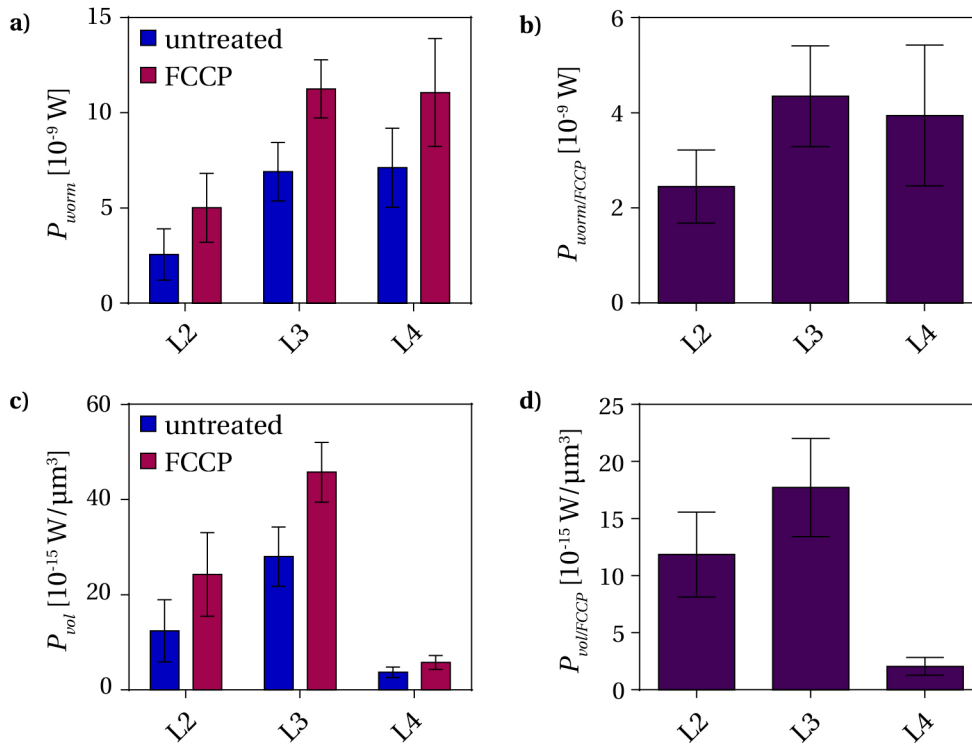


Figure 2.21 – Overview and analysis of the metabolic heat data comparing *coupled* and *uncoupled* respiration of *C. elegans* at different larval stages. **a)** Metabolic heat power per worm P_{worm} for L2, L3, and L4 larval stages, before (blue bars) and after FCCP treatment (red bars), respectively. For both conditions, P_{worm} increased from the L2 to L3 larval stage and remained constant from L3 to L4. **b)** Differential heat power per worm $P_{worm/FCCP}$, obtained from (a) by subtracting P_{worm} values before and after FCCP treatment, emphasizing an increase of the FCCP-related change in metabolic heat production from the L2 to L3 stage. **c)** Heat power P_{vol} per μm^3 of worm biomass, before and after FCCP treatment, obtained by normalizing P_{worm} with respect to the worm body volume (data shown in Tab. 2.3). Data reflects an increase of P_{vol} from L2 to L3 and a steep drop at the L4 stage. **d)** Differential $P_{vol/FCCP}$ values derived from (c) by subtracting P_{vol} values before and after FCCP treatment, showing a very small impact of the FCCP treatment on P_{vol} at the L4 stage. Data in all graphs is presented as mean \pm SD for each larval stage (n = number of assays as indicated Tab. 2.2 times 3 loading cycles).

Furthermore, we analyzed our data with respect to the body volume of the worms in order to account for their size difference. Experimental worm body volume data at worm ages 12 h, 24 h and 48 h are shown in Tab. 2.3. In Fig. 2.21c, the normalized metabolic heat power per volume P_{vol} (*i.e.* P_{worm} divided by the larval volume) for each larval stage is presented. For untreated

Larval stage	Worm volume [$1 \times 10^6 \mu\text{m}^3$](worm age)	mtDNA copies
L2	0.21 (12 h)	22000
L3	0.25 (24 h)	29000
L4	1.92 (48 h)	130000

Table 2.3 – *C. elegans* larval body volume at different stages (courtesy of B. Atakan, EPFL-LMIS2 [43]) and the total number of mitochondrial deoxyribonucleic acid (mtDNA) copies per larva (N2 wild type worms). Values for the worm length and area were extrapolated from two-dimensional (2D) images at the indicated age, then the volume was calculated using the formula proposed in [101]. mtDNA numbers for a specific larval stage was taken from [102] (exact age in hours was not reported).

worms, an increase in P_{vol} from $(12.4 \pm 6.2) \text{ fW}/\mu\text{m}^3$ for L2 to $(28.0 \pm 5.8) \text{ fW}/\mu\text{m}^3$ for L3 is observed (*i.e.* by a factor of ≈ 2.3). For FCCP-treated worms the metabolic heat production per unit volume increases to from $(24.3 \pm 8.2) \text{ fW}/\mu\text{m}^3$ for L2 to $(45.7 \pm 5.1) \text{ fW}/\mu\text{m}^3$ for L3 (*i.e.* by a factor of ≈ 1.9). This evolution is qualitatively comparable to the heat power P_{worm} normalized per worm in Fig. 2.21a. However, in contrast to P_{worm} , P_{vol} dropped significantly in the L4 stage ($(3.7 \pm 1.0) \text{ fW}/\mu\text{m}^3$ and $(5.8 \pm 1.3) \text{ fW}/\mu\text{m}^3$, for untreated and FCCP-treated worms, respectively). The absolute heat power per volume after FCCP treatment $P_{vol/FCCP}$ in Fig. 2.21d, again emphasizing merely the impact of FCCP on the heat production, shows a corresponding sharp drop from L3 to L4. The relative increase of untreated and FCCP-treated worm signals are identical for P_{worm} and P_{vol} . A statistical analysis of the data is provided in Tab. 2.4.

Larval stage	p -value	t -ratio	df	P_{worm} and P_{vol} increase by FCCP treatment
L2	0.006	3.185	15	95%
L3	0.003	4.110	8	63%
L4	0.026	2.662	9	55%

Table 2.4 – Statistical analysis of metabolic assays. Student’s t -test with a 95 % confidence limit ($p \leq 0.05$, degrees of freedom df) of metabolic heat data and percentage of increase of metabolic heat production P_{worm} and P_{vol} upon FCCP treatment.

2.8 Discussion

The signal-to-noise ratio (SNR) of chip calorimeters decreases upon downscaling of sensor and sample size, mainly because the ratio of heat producing sample volume to heat sensing surface becomes smaller [67, 103]. In our device, the shallow shape of the microfluidic chip allows keeping the whole sample suspension in close contact with the thermopile sensor, thereby optimizing metabolic heat collection and reducing heat losses. Separation of sample solution and the sensing surface by a very thin membrane minimizes heat transfer resistances and time constants. These improvements result in a nearly 5-fold increase of the power sensitivity as compared to the previous open-chamber system, where a similar 1-propanol in water mixing calibration experiment was performed ($PS = 3.4 \text{ V/W}$ vs. 0.6 V/W , respectively) [78]. Furthermore, slow or almost steady-state heat generating processes, typically

observed in metabolic or other biological studies, further decrease the SNR, as heat losses to the environment become more prominent [67, 103]. The standard approach of detecting slow processes is to keep the sample volume sufficiently high to achieve a proper SNR. Working with sample volumes in the μl -range containing biological entities, such as bacteria, cells or *C. elegans*, therefore requires carefully designed experimental settings to record the resulting nW-range metabolic heat signals in real-time. We circumvented this issue by introducing a sequential measurement protocol, *i.e.* by repeatedly displacing the whole sample volume on- and off-chip, resulting in a sequence of short recording intervals. On the one hand, this protocol minimizes heat loss during the measurement cycle, and, on the other hand, reference signals may be recorded immediately after each sample unloading step. Any slow baseline drift superimposing the biological signal can thus be extracted. The LOD was determined as $3 \times \text{SD}$ of the $V_{TP}(t)$ signal before the first oscillatory unloading step, *i.e.* the constant heat power signal of a stationary worm population on the chip (measurement duration 1400 s, corresponding to the duration of a whole oscillatory cycle). The mean LOD value for all assays was ≈ 280 nW, corresponding to the metabolic heat production of ≈ 100 L2 or ≈ 37 L3/L4 worms.

In a previous study, a population of ≈ 3000 adult worms was loaded into a commercial isothermal microcalorimeter and monitored over a period of about two weeks, requiring incubation with culture media containing antibiotics to suppress bacterial growth [58, 59]. Confinement in an ampoule did not allow any interaction with the sample, in particular fluidic exchange and the application of active compounds to evaluate the effect on the metabolic response of the organisms. Results obtained by this group suggested that metabolic heat output decreases exponentially in aging adult worms [58]. Moreover, an increase of heat production during dauer recovery was observed [59]. It was thus possible to observe qualitatively the heat produced by large larval worm populations, however, low signal and time resolution impeded further quantification and analysis. The measured metabolic heat was normalized with respect to the protein content of the worm [59]. In our study, we focused on larval metabolic heat signals, since these could not be recorded precisely in the previous studies. We determined the volume-specific heat, thus our results do not rely on specific assumptions on the protein content of the worms. Taking advantage of our microfluidic/nanocalorimetric device, we could clearly improve the conventional system performance, by enabling basal heat signal recordings of *C. elegans* larval populations of only 60 to 220 animals, *i.e.* up to 50 times smaller than previously reported. In addition, the microfluidic technique allows applying versatile fluidic protocols during the thermal recording. PDMS on-chip filter structures, as shown in Fig. 2.15, allowed convenient trapping and confinement of larvae from the L2 to L4 stage in the measurement chambers. By this means, measuring directly the variation of the metabolic heat in *C. elegans* upon application of an uncoupling agent was achieved for the first time with our microfluidic device. The chip design may be readily adapted for adult worms by slightly upscaling critical dimensions. However, manipulation of L2 larvae may be more difficult, as these small worms either may pass through the flexible PDMS filter structure or tend to form clusters and clog the structure if the filter spacing is too small.

Mitochondria are the major metabolic heat source in a living organism. Metabolic heat data presented in Fig. 2.21 therefore evoke a comparison with the total number of mitochondria in a worm, or the corresponding amount of mitochondrial deoxyribonucleic acid mtDNA, respectively. Tsang et al. determined the mtDNA copy number at different worm development stages (see Tab. 2.3) [102]. The authors found a moderate rise from larval stage L2 to L3, followed by a strong increase from the L3 to the L4 stage. Another outburst of mitochondrial growth occurred at the transition to adulthood, corresponding to an increasing energy requirement of the organism when entering in the reproduction phase. In Fig. 2.21 we plotted the variation of metabolic heat from the early L2 to the late L4 stage. For untreated worms, the metabolic heat per worm P_{worm} showed a ≈ 2.6 -fold increase from the early L2 to the late L3 stage, and then remained constant up to the late L4 stage (Fig. 2.21a). In principle, one would expect a correlation of the heat signal and the number of mitochondria at the different development stages. However, comparing our data with [102], suggests that the onset of metabolic heat production somewhat precedes the reported increase of the mtDNA copy number from L3 to L4. Unfortunately, the exact age in hours at the mtDNA count in a specific larval stage was not reported, thus a certain overlap of heat signal and mtDNA count increase in the L3 stage is still conceivable. Nevertheless, more detailed studies are required to confirm a possible correlation between the two phenotypes.

Metabolic heat values P_{vol} normalized with respect to body volume at different larval stages (Fig. 2.21c) showed an increase from L2 to L3, and a dramatic decline from L3 to L4. Combining own *C. elegans* experimental volumetric growth data (shown in Tab. 2.3) and mtDNA counts in the corresponding larval stage, yields a mtDNA content of 0.11 copies/ μm^3 in early L2, 0.12 copies/ μm^3 in late L3 and 0.07 copies/ μm^3 in late L4, respectively. The larval age corresponds to the time point when the worm volume was determined. According to this data, the worm body volume outgrows the reported mitochondrial proliferation occurring from the L3 to L4 stage (increase by a factor of ≈ 7.7 and ≈ 4.5 , respectively), resulting in an effective diminution of the mtDNA density, which qualitatively accounts for the strong drop in P_{vol} from L3 to L4. However, further biological investigations are required to unravel the experimentally observed quantitative evolution of this phenotype. Other heat generating processes, e.g. muscle contraction powered by ATP consumption or non-mitochondrial respiration, may add to the measured heat signals, but mitochondrial respiration may be considered as the major part of the heat production [55].

Furthermore, using our nanocalorimetric device, we could quantify the variation of metabolic heat production in *C. elegans* worms upon treatment with the uncoupling agent FCCP for the first time. For the time being, the metabolic activity of *C. elegans* reacting to uncoupling agents was only evaluated by oxygen consumption rate measurements, however, no complementary direct calorimetric heat measurement has been reported for *C. elegans* undergoing *uncoupled respiration*. Exposure to FCCP has been shown to shift an organism's bioenergetic profile towards an enhanced respiratory capacity, where oxygen uptake is strongly increased. Such experiments have been performed on cell cultures, [104, 105], and more recently for *C. elegans* in the early and late adult stages [106]. Oxygen consumption assays using a commercial

Seahorse XF96 respirometer may be carried out with a small number of worm (10 to 20 adults) and allow the application of treatment agents to the sample well, but not their removal. Injection of FCCP was shown to cause a 2 to 3 fold increase of the oxygen consumption rate in adult worms [106], indicating a shift to maximal mitochondrial respiration capacity due to the collapse of the mitochondrial membrane potential. Interestingly, in our work we observed a clear increase of the metabolic heat generated by FCCP-treated worm populations, *i.e.* from P_{worm} to $P_{worm/FCCP}$ (in the range of $\approx 55\%$ to $\approx 95\%$, depending on the larval stage, see Tab. 2.4). These findings indicate that our metabolic heat power measurements qualitatively correspond to previous oxygen consumption rate measurements. Even if this feasibility study and preliminary data may not allow further biological conclusions, it confirms the correlation of both phenotypes, and thus the possibility to conduct more holistic metabolic studies.

2.9 Conclusions

We proposed a new nanocalorimetric device that may be operated in a closed, PDMS microchip-based configuration. We developed a dual-channel system with two individual thermopile sensors, allowing for two parallel measurements under identical environmental conditions. A membrane-sealed microfluidic chip enables efficient heat transfer from the sample to the sensor and versatile fluidic protocols. A feasibility study, enabling metabolic heat measurements of multicellular organisms, in particular of the nematode *C. elegans*, was designed as validation of our nanocalorimetric system. We conducted experiments on synchronized *C. elegans* larval populations to determine the worm- and volume-specific heat generated at different larval stages and the metabolic heat response during compound-induced *uncoupled respiration*. A principle limitation of isothermal chip calorimetry is that slow heat signal variations in the low μW -range, such as the metabolic heat signals analyzed in the present assays, are prone to low SNR, especially as the sample volume decreases. We successfully implemented an oscillatory fluidic assay protocol, based on the sequential displacement of the worm population, *i.e.* the heat source, on and off the sensing membrane. Our study revealed previously unavailable data on metabolic heat production during the developmental phase of *C. elegans*. The worm population size used in our experiments ranges from 60 to 220 organisms, *i.e.* up to 50 times smaller than previously reported [58, 59]. Moreover, the microfluidic approach enables measuring dynamic metabolic heat changes through the injection of active compounds without disturbing isothermal conditions during heat signal recordings. In particular, we quantified the effect of the mitochondrial uncoupling agent FCCP on the basal metabolic heat production of *C. elegans* larvae at different stages. Our results are supported by findings on mitochondrial biogenesis during the later larval stages. Nanocalorimetry is a highly-sensitive technology that may be combined with other analytical methods. Considering metabolic heat production as a new phenotype opens the way to a more holistic understanding of fundamental biological processes.

3 Indirect calorimetry of *Caenorhabditis elegans* worms

Mitochondrial dysfunction is related to many diseases including metabolic disorders and aging-related conditions. Mitochondrial respiration is a key phenotype for assessing mitochondrial functioning. We present a new microfluidic worm culture system with integrated luminescence-based sensing of the on-chip oxygen concentration for measuring the oxygen uptake of Caenorhabditis elegans worms. The microfluidic chip was fabricated in off-stoichiometry dual-cure thiol-ene-epoxy (OSTE+), allowing reliable measurement of the dissolved oxygen and the fabrication of high-resolution microstructures down to the μm -range. With our microfluidic approach it is possible to confine a single nematode from the L4 stage in a culture chamber over a time span of up to 7 days. An automated protocol for feeding and performing oxygen consumption rate measurements during the worm development was applied. We found an increase of oxygen consumption rate (OCR) values from the L4 stage to the adult worm, and a continuous decrease as the worm ages. In addition, we performed a metabolic assay using C. elegans worms using the mitochondrial uncoupling agent FCCP, which increased OCR by a factor of ≈ 2 when compared to basal respiration rates. Treatment with sodium azide inhibited mitochondrial respiration and returned OCR values to zero.

This section was adapted from the following manuscript:

- **R. Krenger**, T. Lehnert, T. Mayr and M. A. M. Gijs, “On-chip real-time detection of *C. elegans* oxygen consumption rate during its life span”, manuscript in preparation.

3.1 Introduction

Mitochondrial dysfunction is regularly associated with metabolic disorders, *e.g.* diabetes mellitus, obesity and cardiovascular disease, but also neurodegenerative diseases such as Alzheimer's disease, Parkinson's disease, Huntington's disease and amyotrophic lateral sclerosis [12, 13, 14, 15, 16, 17, 18]. Potential drug candidates for combatting such disorders need to be evaluated with respect to adverse effects on the mitochondria [107]. Mitochondrial functioning, *i.e.* ATP production in response to cellular energy demand, can be assayed by measuring the OCR of an organism *in vivo*. Oxygen uptake can be considered as a direct indicator of cellular respiration [108]. Measuring OCR in order to evaluate mitochondrial functioning on a whole-organism level has a greater physiological relevance than looking at cell lines or even isolated mitochondria, but the analysis of results is more complex and leaves more room for interpretation. As mentioned before, the nematode *C. elegans* is a convenient model organism in biology for researching diseases and whole organism drug screening due to its genetic amenability and the availability of human disease models (refer to section 1.1) [2, 19, 20]. Worms are suitable for assays extending over the animals' whole life span. Microfluidic phenotyping platforms have been developed for a wide range of assays, including measuring the life span of worms on-chip in an automated manner, and monitoring embryonic and post-embryonic development upon drug exposure at single-organism resolution [40]. A platform developed by Letizia *et al.*, for example, allows evaluating parameters such as egg hatching rate, embryonic and larval development time, worm length, and more importantly, the mitochondrial stress in mutant GFP expressing worms (*hsp-6p::gfp*) during the full life span [41]. In their study, they used the antibiotic doxycycline to induce mitochondrial unfolded protein response (UPR^{mt}), *i.e.* a mitochondrial response to stress conserved in living organisms [109, 110]. The authors used fluorescence imaging to quantify the induction of UPR^{mt} in doxycycline-treated worms and compared the signals to untreated worms. Their results confirmed expected phenotypic changes upon drug treatment, *i.e.* delayed worm development, reduced egg laying rates and enhanced mitochondrial stress.

However, the direct measurement of OCR to assess mitochondrial functioning of *C. elegans* worms on-chip was not possible so far. The development of a microfluidic life span phenotyping platform with the capability of integrated oxygen sensing, while keeping the possibility of measuring the response of a single animal, could be crucial for enabling more advanced screening of the mitochondrial state on the whole-organism level. Additionally, the presence of oxygen in on-chip culture applications of living organisms is an important parameter for maintaining homeostasis, development, behavior and physiological conditions in general. Integrated oxygen sensing could help to monitor on-chip oxygen levels and thus enable better defined assay conditions.

In the present chapter, we describe the development of a microfluidics-assisted platform for life-time culture of single *C. elegans* worms with integrated luminescence-based oxygen sensing capability. The approach allows the confinement of a single young worm (L4 stage) and subsequent on-chip culture in a microfluidic chamber with automated feeding and OCR

3.2. Current approaches for OCR measurements

measurements in regular intervals. Additionally, the platform allows the reversible applications of active compounds during the assays. In section 3.2, the state-of-the-art for respirometry is summarized, and an overview of commercial equipment for OCR measurements is given. The sensing principle of the luminescence-based oxygen sensing technique is explained in section 3.2.2. Relevant state-of-the-art of existing systems for OCR measurements of *C. elegans* is presented in section 3.3. In section 3.4, our microfluidic approach for measuring OCR is detailed. Section 3.5 describes the new system and experimental protocol that were developed. Results obtained are presented (section 3.6) and discussed (section 3.7).

3.2 Current approaches for OCR measurements

3.2.1 Small-scale systems based on electrochemical detection

The development of miniaturized sensors enabled the integration of these sensors in microfluidic environments [111]. In early stages, small-scale Clark-type electrodes were used for electrochemical detection of dissolved oxygen [112, 113]. Clark-type electrodes rely on the reduction of molecular oxygen at the cathode that generates an electrical current. Major disadvantages of this sensor type are the intrinsic consumption of oxygen that can skew the results of measurements and their relatively short life span due to the contamination of the electrodes by means of the chemical reactions required for sensing [114]. Another drawback with respect to integration in fluidic devices is the requirement of physical electrical connections to the sensing electrodes for the read-out of current flows.

3.2.2 Miniaturized systems using luminescence-based oxygen sensors

Compared to electrochemical oxygen sensors, optical sensing methods are more promising for integration in microfluidic systems. The technique is fully non-invasive, easily scalable, does not get degraded by the analyzed sample, does not intrinsically consume dissolved oxygen and requires no physical connection between the sensor and the detector [115, 116, 117, 114]. Optical oxygen sensors take advantage of a luminescence-based method, where oxygen molecules quench the intensity or lifetime of an excited state in a luminescent indicator molecule [118].

Working principle of luminescence-based oxygen sensors

Photoluminescence is the spontaneous emission of light by a substance upon absorption of photons. Photoluminescence can be classified into fluorescence and phosphorescence: in fluorescence, a dye immediately re-emits absorbed radiation albeit a frequency shift, whereas in phosphorescence, re-emission of a photon takes place on a longer time scale. Luminescence-based oxygen sensors take advantage of either phosphorescent or fluorescent indicator dyes whose luminescent properties change depending on the oxygen concentrations they are ex-

posed to. Specifically, the presence of oxygen quenches luminescence by inhibition of photon re-emission by absorbing the energy of the excited state of the dye [119]. The Stern-Volmer equation models the quenching behaviour [120]:

$$\frac{\tau_0}{\tau} = \frac{I_0}{I} = 1 + k_q \cdot \tau_0 \cdot cO_2, \quad (3.1)$$

where cO_2 is the concentration of dissolved oxygen, k_q is the quenching rate constant, τ and τ_0 are the excited state lifetimes in the presence and absence of oxygen, I and I_0 are the excited state luminescence intensities in the presence and absence of the oxygen. Based on this model, by detection of the luminescence intensity or excited state lifetime, the oxygen concentration can be calculated. A schematic view of the principle and a possible measurement setup is shown in Fig. 3.1a.

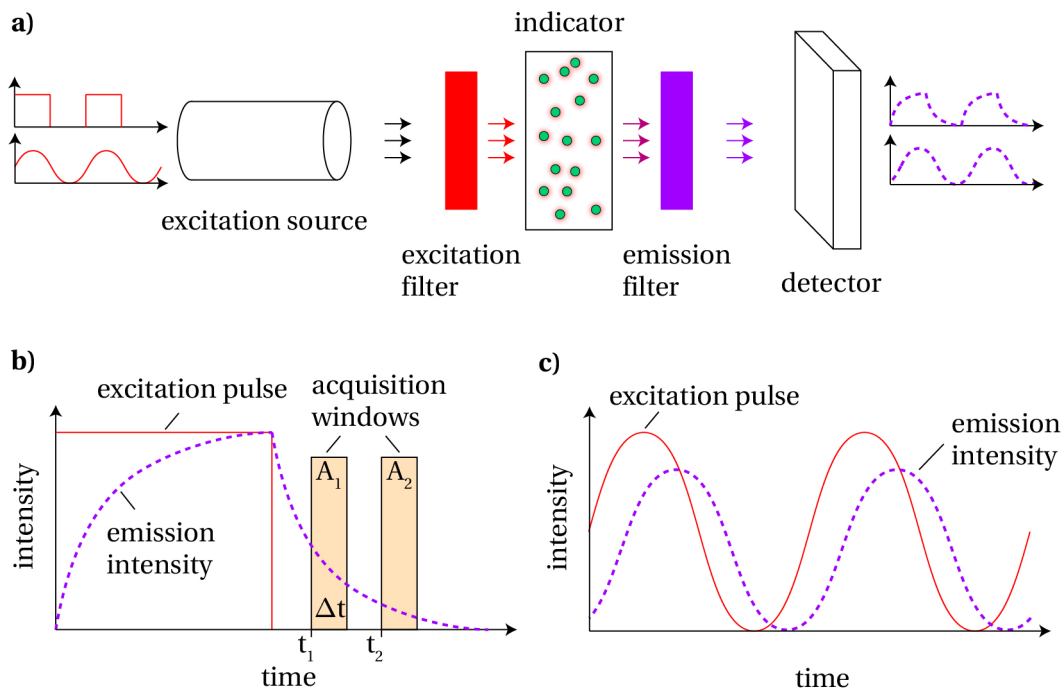


Figure 3.1 – Illustration of the sensing principle of luminescence lifetime-based oxygen concentration measurements. **a)** Schematic of a minimalistic measurement setup for lifetime-based sensing of dissolved oxygen concentration. Modulated light (sinusoidal or square wave) from an excitation source is used for excitation of the luminescent indicator dye. The sinusoidally or exponentially modulated light emitted by the dye is captured by a detector. **b)** Principle of time-domain luminescence lifetime detection. Light modulated with a square wave excitation pulse (red curve) is used to induce luminescent emission that decays exponentially after excitation is stopped (purple curve). Two or more acquisition windows with a duration of Δt are used to characterize the time constants of the exponential decay. **c)** Principle of frequency-domain based methods for luminescence lifetime detection. The information about the luminescence lifetime is contained in the phase shift between the sinusoidally modulated excitation pulse end the emitted light intensity. Based on [111], [121] and [122].

3.2. Current approaches for OCR measurements

Measurement of the emitted light intensity after excitation of the sensing dye is easy to implement, but shows significant effects of photobleaching after repeated excitation. Therefore, luminescence lifetime-based sensing methods are more robust and more commonly used. In luminescence lifetime-based sensing, a modulated excitation light source is used to measure the luminescence lifetime of the re-emitted light of the indicator dye, either in the time domain or in the frequency domain. In the time domain (Fig. 3.1b), the excitation pulse is a square wave that induces exponential decay of the re-emitted light intensity. A minimum of two acquisition windows A_1 and A_2 (at times t_1 and t_2 with durations of Δt) are used to characterize the exponential decay. The luminescence lifetime τ of the indicator dye can then be calculated according to the following equation:

$$\tau = \frac{t_2 - t_1}{\ln\left(\frac{A_1}{A_2}\right)} \quad (3.2)$$

The measurement method in the frequency domain (Fig. 3.1c) is performed by analyzing the phase shift between the modulated excitation light pulse and the emitted intensity by the luminophore. The phase shift Φ can be calculated with the equation:

$$\tan(\Phi) = \omega\tau, \quad (3.3)$$

where ω is the angular frequency of the modulated excitation pulse [122]. The device that is used in this work is based on the lifetime-based sensing method in the frequency domain.

3.2.3 Commercial OCR equipment

Respirometry is a common technique applied in many research laboratories for metabolic studies on living organisms. The current state-of-the-art in commercial respirometry is the Seahorse Extracellular Flux Analyzer (Seahorse XF, Agilent, USA), shown in Fig. 3.2a [123]. This device is capable of measuring cellular oxygen consumption rate and extracellular acidification rate (ECAR) of living cells in a 96-well plate format (Seahorse XF96). ECAR measures the concentration of H^+ ions in solution or, in other words, a change of pH in the culture environment. This can be used to gain more insight on the rate of glycolysis in the mitochondria, as the production of lactic acid during the anaerobic conversion of glucose to pyruvate lowers the pH in the culture media [124]. Additionally, acidification is caused by CO_2 produced in the TCA cycle during respiration. The working principle of the Seahorse XF respirometer is illustrated in Fig. 3.2b. The samples, usually cells cultured in a monolayer in custom Seahorse cell culture microplates, are first inserted into the respirometer. A $37^\circ C$ culture environment is provided in the device. Each well contains a working volume of culture media of about $150\ \mu l$ to $275\ \mu l$. The sensing cartridges are equipped with oxygen- and H^+ sensitive luminophores. An optical technology is used for the measurement of the O_2 or H^+ dependent luminescence of these molecules (further explained in section 3.2.2). During OCR and ECAR measurements,

Chapter 3. Indirect calorimetry of *Caenorhabditis elegans* worms

an array of optical fibers is inserted into the well plate containing the samples. At the same time, the fiber confines the sample volume in the well to about 2 μl and seals the chamber to prevent oxygen diffusion from culture media above the sealed microplate. The device then measures the concentration of O_2 and H^+ in real time during 5 min to 8 min to determine the OCR and ECAR of the sample, respectively, resulting in a single data point. Injection ports adjacent to the optical fiber offer the possibility to sequentially introduce up to four drugs sequentially into the microplates. The treatment agents are dispersed uniformly in the culture environment of the cells by means of a mixing mechanism consisting of moving the optical fiber up and down into the culture medium repeatedly. Such protocols are used to perform standard metabolic assays or studies that involve the measurement of a drug-dependent response. Metabolic assays of mitochondrial function are performed using serial injections of test compounds into the wells containing cell culture (section 1.2, Fig. 1.5) [31].

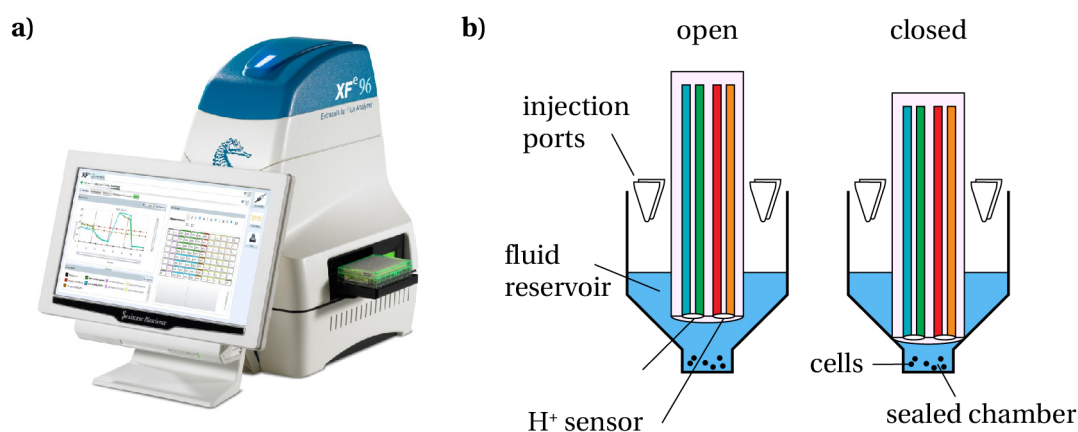


Figure 3.2 – Commercial Seahorse XF respirometers. **a)** Photograph of a commercial Seahorse XF96 respirometry system (Agilent Technologies, USA). **b)** Measurement unit of the respirometer. The sensor cartridge contains fluid reservoirs with embedded luminophores that are excited by light transmitted through optical fibers in the measurement probe. The measurement probe is used in two positions (open and closed) to create a sealed microchamber during the oxygen concentration measurements. 4 injection ports are used to inject treatment compounds into the fluid reservoir. Adapted and reproduced from [123].

Not considering the high cost of the Seahorse XF respirometers, these commercial devices have a large set of advantages but a couple of particular disadvantages that prevent their use in more specific applications and complex experimental designs. These advantages and disadvantages are summarized in the following. The 96-well plate format in the Seahorse respirometers offers the potential for large scale screening applications due to the possibility of multiplexed experiments. To obtain a single OCR and ECAR data point in a simultaneous measurement, only a duration of a few minutes is required. The relatively low required sample volume of down to 150 μl per well is cost-efficient. In addition, in common with all optical OCR detection methods, the technique is non-invasive and does not require specific sample preparations with fluorescent markers, for example. The well-plate format has several limitations as well, especially when long-term studies have to be performed. The protocol is optimized

for adherent and suspension cell cultures. The cultures need manual maintenance during longer experiments, as culture media in the wells need to be replenished due to the depletion of nutrients and the presence of metabolic waste products. Treatment agents, which are no longer desired in the wells after injection, must also be removed from the culture environment manually. For other applications, in particular multicellular organisms such as *C. elegans* requiring culture temperatures ranging from 20 °C to 25 °C, the automated temperature control has to be turned off, as it was designed to run at 37 °C. Then, ambient temperature determines the temperature in the sample cartridge. However, during the operation, the internal temperature of the device increases by about 2 °C to 4 °C, compromising the determination of precise OCR values due to temperature fluctuations and physiological changes [106]. In the specific case of *C. elegans* long-term studies, progeny could not be flushed away from the wells, also influencing OCR values. Nevertheless, Seahorse XF respirometry has already been used in several studies [125, 126, 127, 128, 106], where the mitochondrial function in *C. elegans* has been characterized.

3.3 OCR measurements of *C. elegans*

A simple standard method for the determination of the OCR of *C. elegans* samples in many laboratories involves the suspension of hundreds to thousands of worms in ml-sized volumes in respirometer cells containing Clark-type electrodes [58, 129, 130]. On the other hand, the Seahorse XF respirometers (Seahorse Bioscience, USA) offer optical detection of the oxygen concentration in a multiplexed well-plate format with up to 96 wells. Injection of treatment agents is possible to directly study the response of the sample to specific compounds. Several studies have been performed with these respirometers, where it was possible to measure the OCR of as few as 10 worms per well starting from the L4 larval stage [125, 126, 127, 128, 106].

A custom-made instrument by Suda *et al.* based on a commercial oxygen probe with an optical detection method, where the OCR of 1 to 40 adult worms could be measured in a sealable acrylic chamber ($d = 1$ mm, $h = 0.5$ mm) is shown in Fig. 3.3a [131]. Here, the probe was inserted directly into the liquid in the chamber, and the system was sealed with silicon grease. Using this system, they were able to measure consumption rates of worms aged 2 to 10 days. However, their chamber was prone to evaporation and did not permit to perform measurements with a duration longer than 12 h.

Huang *et al.* presented a microfluidic module with a pneumatically actuated PMMA lid used for sealing of a PMMA microwell, where the OCR of a single worm can be measured (Fig. 3.3b) [132]. An oxygen-sensitive luminescent layer on the bottom of the wells was used for the quantification of the oxygen concentration. They also assessed the basal respiration and the maximal respiration rate using the compounds FCCP and N_3^- , which allowed the determination of basal OCR, ATP-linked OCR, maximal OCR, and non-mitochondrial OCR.

Chapter 3. Indirect calorimetry of *Caenorhabditis elegans* worms

Manual treatment of a single worm with these components was possible with their design, however, long-term culture including feeding and washing out of embryos/larvae was not possible.

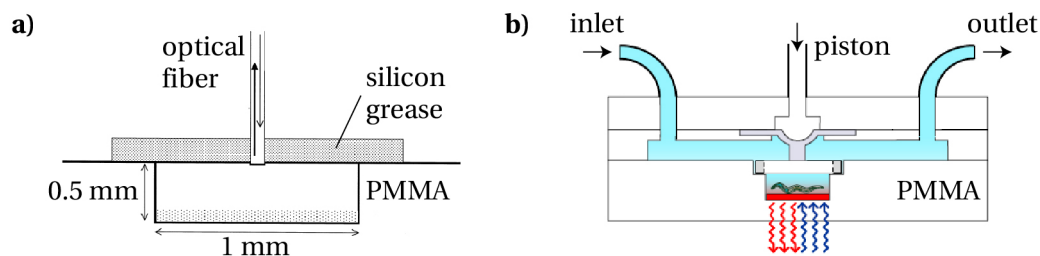


Figure 3.3 – Microchamber-based approaches for OCR sensing on *C. elegans*. **a)** Illustration of the PMMA microchamber by Suda *et al.* Adapted and reproduced from [131]. **b)** Illustration of the PMMA microchamber with a pneumatically actuated piston by Huang *et al.* Adapted and reproduced from [132].

In a reference study performed by Koopman *et al.* in a Seahorse XF96 respirometer, the authors measured the basal respiration, maximal respiration and non-mitochondrial respiration and non-mitochondrial respiration of wild-type *N2* worms and a strain with a genetically modified electron transport chain, namely *mev-1(kn1)*. Their results show that the metabolic rate of the worms varies considerably according to the worm life stage. Peak basal respiration rates are reached during the period of maximal reproduction, with a significant decline after day 4 of adulthood. Fig. 3.4a shows the OCR profile of well-fed nematodes obtained from NGM agar plates until day 12 of adulthood. Measured OCR values normalized to a single organism range from ≈ 5 pmol/min in the L4 stage to ≈ 13 pmol/min during peak consumption rates in adult worms at day 4 of adulthood [106]. A metabolic assay was also performed with the uncoupling agent FCCP and the respiration inhibitor N_3^- . The results of the assays are shown in Fig. 3.4b and Fig. 3.4c. Upon FCCP treatment, normalized respiration rates of adult worms increased by a factor of ≈ 2 in a non dose-dependent manner (Fig. 3.4b). Treatment with azide allowed to determine non-mitochondrial respiration (consumption of O_2 originating *e.g.* from enzymatic reactions) of adult worms (Fig. 3.4c). A critical dose of N_3^- 40 mmol/l was required to block respiration entirely. Non-mitochondrial OCR values corresponded to ≈ 2 pmol/min per adult worm.

For all approaches presented so far, for the measurements of the OCR over the worms life span, multiple and separate experiments with worms from each developmental stage had to be performed. For each experiment, worms were taken directly from NGM agar plates, because the devices were not designed in a way that allows worms to be cultured within the system in the presence of nutrients.

3.4. Microfluidic approach for oxygen sensing

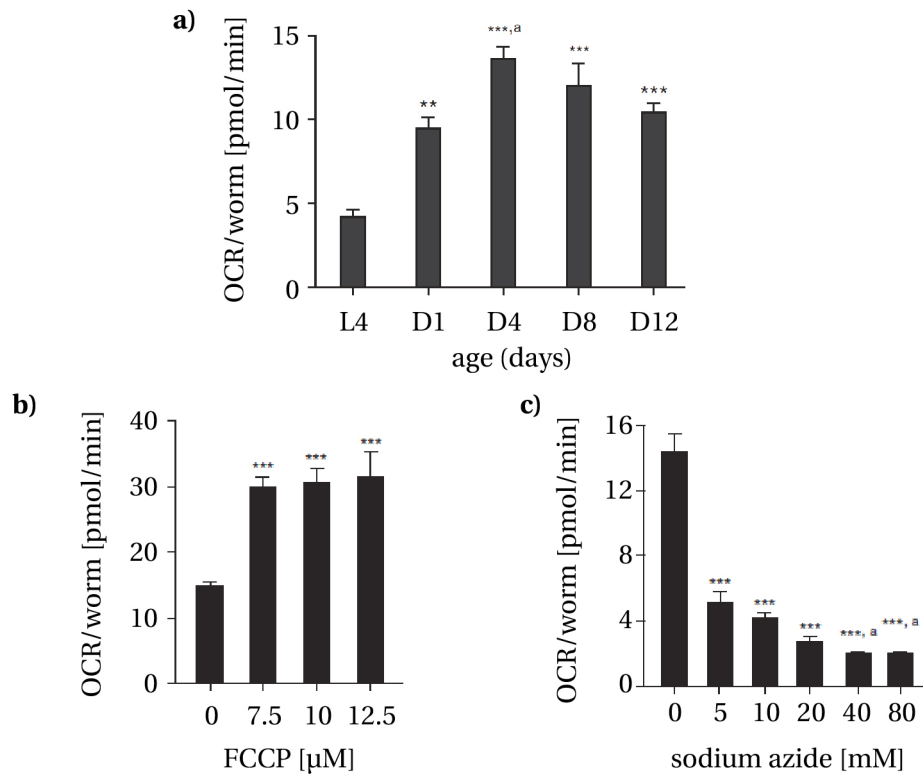


Figure 3.4 – Single worm respiration rates of *C. elegans* in basal and uncoupled conditions obtained in a Seahorse XF96 respirometer. **a)** Basal respiration rates of *C. elegans* from larval stage L4 to day 12 of adulthood. OCR values increased from L4 to day 4 of adulthood, and dropped for older worms. **b)** Maximal respiration rates upon treatment with the mitochondrial uncoupling agent FCCP. The OCR values increased approximately by a factor of 2. **c)** Non-mitochondrial respiration rates of worms after disruption of the respiratory chain. Adapted and reproduced from [106].

3.4 Microfluidic approach for oxygen sensing

3.4.1 Considerations for on-chip culture and OCR measurements

Microfluidic devices permit robust life span culture and phenotypic analysis of few organisms from embryos to adult worms [133, 134, 135, 40, 43]. Microfluidic chips with culture chambers specifically designed for *C. elegans* solve the previously stated issues concerning culture and long term studies on them. Using automated pumps, feeding, removal of progeny and manipulation of treatment compounds in the worm's culture environment is readily feasible. Furthermore, microfluidic chips can be used in combination with integrated optical oxygen sensing. Common soft lithography with PDMS is generally used for manufacturing of the chips due to the simplicity of fabricating chips with low feature sizes, low cost, and the biocompatibility of the material [136]. PDMS has a high gas permeability and oxygen permeability in particular [137, 138, 139]. In fact, PDMS was shown to continuously replenish and stabilize on-chip oxygen levels by oxygen diffusion through the bulk polymer [140]. This was a

Chapter 3. Indirect calorimetry of *Caenorhabditis elegans* worms

	Glass	Thermo- plastics	Elastomers	Ostemers
Young's modulus [GPa]	50 to 90	1.4 to 4.1	0.0005	1
microfabrication technique	etching	injection-molding	casting	casting
smallest channel dimensions	< 100 nm	≈ 100 nm	< 1 μm	< 1 μm
thermal stability	very high	medium-high	medium	medium
solvent compatibility	high	medium-high	low	medium
oxygen permeability	very low	low	high	low-medium
optical transparency	high	high	high	high

Table 3.1 – Overview of relevant materials for microfluidic chip fabrication with integrated oxygen sensors. Based on [141]. Ostemer data taken from [142].

significant advantage previous microfluidic culture applications, because oxygen supply to the living organisms is a not an issue. For oxygen sensing applications, however, it is necessary to prohibit fast oxygen resupply into the media in order to be able to measure the oxygen depletion of the samples on-chip. Therefore, materials with low gas permeability such as glass, silicon or thermoplastics were chosen in the devices and studies discussed in section 3.3.

On the other hand, for on-chip culture of *C. elegans* nematodes, microfluidic chips with small feature sizes down to the μm-range are required, for instance for worm traps or filter structures. An overview of the relevant materials with respect to microfluidic chip fabrication with integrated oxygen sensors is given in Tab. 3.1.

Glass is solvent-resistant, optically transparent, and has an almost zero oxygen permeability. However, microfabrication is time-consuming, expensive and not easily scaleable. Dangerous chemicals such as hydrofluoric acid are needed for etching steps, and wafer bonding at high pressure or high temperature is difficult [143, 141]. Furthermore, microfluidic connections require glass drilling and often involve adhesives [144]. In contrast to glass microfluidic devices, thermoplastics such as PMMA, polycarbonate (PC) or polyethylene terephthalate (PET) can be shaped by hot embossing or injection molding. Moreover, micromilling can be used for shaping of fluidic structures and microchannels [145, 146]. This technique is a convenient way for fast prototyping, provided that feature structures are not too small. Microfluidic systems fabricated from thermoplastics are often made by injection molding, which allows the large-scale production of numerous devices in parallel, provided that expensive metal or silicon molds are available [141]. For these reasons, materials like glass, silica or thermoplastics are not ideally suitable for fast prototyping on lab-scale.

3.4. Microfluidic approach for oxygen sensing

Newer polymer systems based on photoinitiated thiol-ene reactions emerged as a promising alternative for lab-on-a-chip applications [147]. These polymers allow replica molding and are therefore suitable for lab-scale studies and fast prototyping [148, 149]. Recently, the off-stoichiometry dual-cure thiol-ene-epoxy (OSTE+) polymer system was introduced. A two-step curing process enables rapid prototyping of rigid microfluidic devices with properties similar to thermoplastics [150, 142]. The polymer system is composed of three monomers: thiols, enes and epoxies. In the first photoinitiated polymerization step, thiols polymerize with enes resulting in an elastomer with properties similar to PDMS. The second curing step produces a rigid, inert polymer by heat activated polymerization of the thiol-ene with the epoxy monomer. Thermal bonding can be carried out simultaneously with the second curing step, where the polymer becomes rigid and can be bonded to different surfaces including glass, aluminium, silicon, thermoplastics and OSTE+ itself. The biocompatibility of cured OSTE+ polymer is comparable to polystyrene and polycarbonate [150, 151]. The OSTE+ polymer system is suitable for on-chip oxygen concentration measurements and *C. elegans* life span culture applications for two main reasons: (i) low gas permeability ($\approx 10\%$ that of PDMS) and (ii) the possibility of fast prototyping of small-featured microfluidic devices using a process similar to PDMS. The curing steps can be carried out with only a UV lamp and an oven and do not require intensive manual labor steps or expensive laboratory equipment such as an oxygen plasma system.

3.4.2 Integration of the oxygen sensor

For the integration of oxygen sensing capabilities into microfluidic chips, we used a modified version of the commercially available REDFLASH oxygen sensor spots (pyroscience, Germany) and a Piccolo2 oxygen meter (PICO2-OEM, pyroscience, Germany) combined with a 1 m long optical fiber (PICFIB2, pyroscience, Germany). The sensing principle has been described in section 3.2.2. The sensor spots are approximately 1 mm in diameter and were spotted onto a standard microscopy glass slide using a CNC airbrush to a final thickness of about 2 μm . The spots are excited with red light at a wavelength of 610 nm to 630 nm and emit oxygen-dependent luminescence in the near infrared (NIR) range at 760 nm to 790 nm [152]. Precise information of the sensor dye composition and preparation of the spots can be found in [153], where the same sensor has been used in silicon-glass microreactors. To read-out the oxygen concentration from the OSTE+ microfluidic chips, the Piccolo2 oxygen meter was placed directly below the REDFLASH sensor spot as shown in Fig. 3.5a. Light from the oxygen meter is guided through the optical fiber towards the sensor spot. The re-emitted NIR light is guided back towards the detector of the oxygen meter. Good re-emission signal intensities were obtained for the custom sensor spots with 60 % light emitting diode (LED) intensity of the oxygen meter. The assembled oxygen sensing setup (see section 3.4.3 for fabrication process) including fluidic connections is illustrated in Fig. 3.5b. The optical fiber of the oxygen meter is brought in contact with the glass slide through an opening in the PMMA clamp.

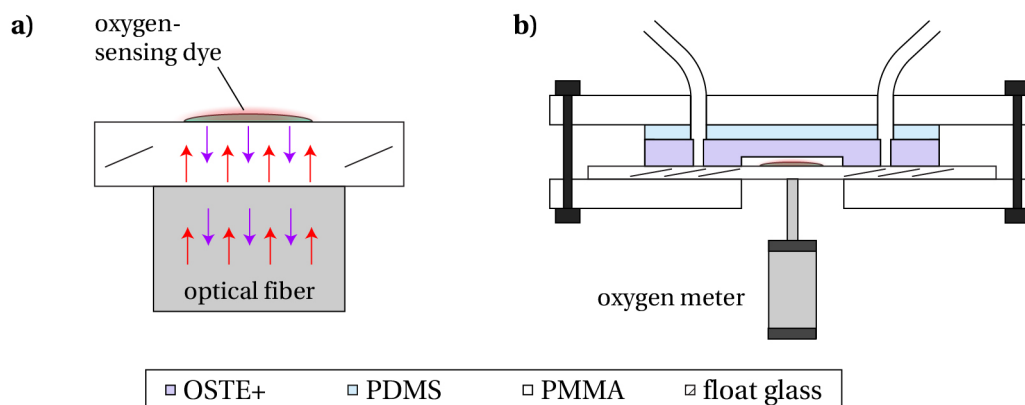


Figure 3.5 – On-chip luminescence-based oxygen sensing method. **a)** Light emitted from the LED of the Piccolo2 oxygen meter is guided through an optical fiber and the glass slide onto the oxygen sensing dye, where it excites the dye and generates oxygen concentration dependent re-emission of NIR light. The re-emitted light is guided back through the optical fiber and is detected in the oxygen meter. **b)** The final chip assembly with fluidic connections and an opening in a PMMA clamp for accommodating the optical fiber.

3.4.3 Microfabrication

To fabricate microfluidic chips from the OSTe+ polymer, replication molding from SU-8 photoresist patterns on Si molds was used. For details on the mask and SU-8 replica mold fabrication, see sections 2.4.1/2.4.2 and Fig. 2.6/2.7.

OSTe+ replication molding

Ostemer 322 Crystal Clear (OSTe+) resin was obtained from Mercene Labs AB (Stockholm, Sweden) [142]. An 80 μm high SU-8 on Si mold was fabricated and diced using standard methods. Subsequently, the SU-8 on Si patterns were silanized with TMCS in a vacuum chamber for at least 15 min. For the replica molding of OSTe+, the SU-8 mold was inserted into a custom mold, comprising of Al, nitrile butadiene rubber (NBR) and UV light transmitting PMMA that defines the final chip height of 2 mm (Fig. 3.6a and b). A uniform chip height is important in the molding process in order to guarantee uniform UV exposure of the resin. The Al part of the mold guarantees that heat generated in the UV curing reaction is efficiently dissipated to prevent early initiation of a second heat curing step.

Inlet holes for the connection of microfluidic tubing are made by inserting thin metal pins through holes in the PMMA cover part of the mold. After mixing the two components of the OSTe+ resin in the ratio which was provided by the manufacturer (1.09:1) and degassing in a vacuum chamber for about 15 min, the resin was injected into the mold, where the OSTe+ was UV-cured afterwards for 35 min using a UV lamp (GV2M20, Syngene, United Kingdom).

3.4. Microfluidic approach for oxygen sensing

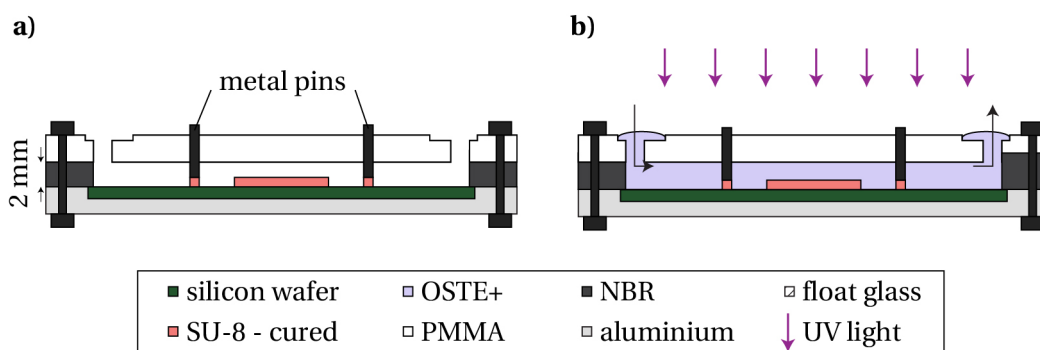


Figure 3.6 – Illustration of the OSTE+ replica molding process. **a)** The diced SU-8 on Si wafer is clamped into the custom Al, NBR and UV-transmitting PMMA mold that fixes the chip height to 2 mm. Metal pins are inserted through the PMMA to make inlet holes for connecting microfluidic tubing. **b)** OSTE+ prepolymer is gently injected through holes in the PMMA using a syringe. Small reservoirs around the injection holes are filled with excess prepolymer to account for the expected shrinkage during the UV curing step.

Chip assembly

After unmolding of the cured, flexible OSTE+ chip that contains the microfluidic channels, the chip was aligned to a glass slide that contains a spot of the oxygen sensing nanoparticle (see section 3.4.2) and bonded at 110 °C for 2 h under pressure in a metal clamp (Fig. 3.7a and Fig. 3.7b). An OSTE+ release liner (Mercene Labs AB, Stockholm, Sweden) was used to prevent bonding of the OSTE+ resin to the metal clamp. After this second curing step, the material is now fully polymerized and rigid. It is also permanently bonded to the glass slide (Fig. 3.7c). A photograph of the fully cured and bonded OSTE+ chip is shown in Fig. 3.8a. To make leakage free connections using microfluidic tubing to the now rigid OSTE+, a slab of cured PDMS (thickness \approx 3 mm) with 1.5 mm diameter punched inlet holes corresponding to the positions of the inlet holes was first manufactured. A custom laser-cut PMMA mold was used to align and tightly clamp the PDMS slab to the OSTE+ to form the final chip assembly (Fig. 3.7d). A photograph of the clamped chip assembly is shown in Fig. 3.8b.

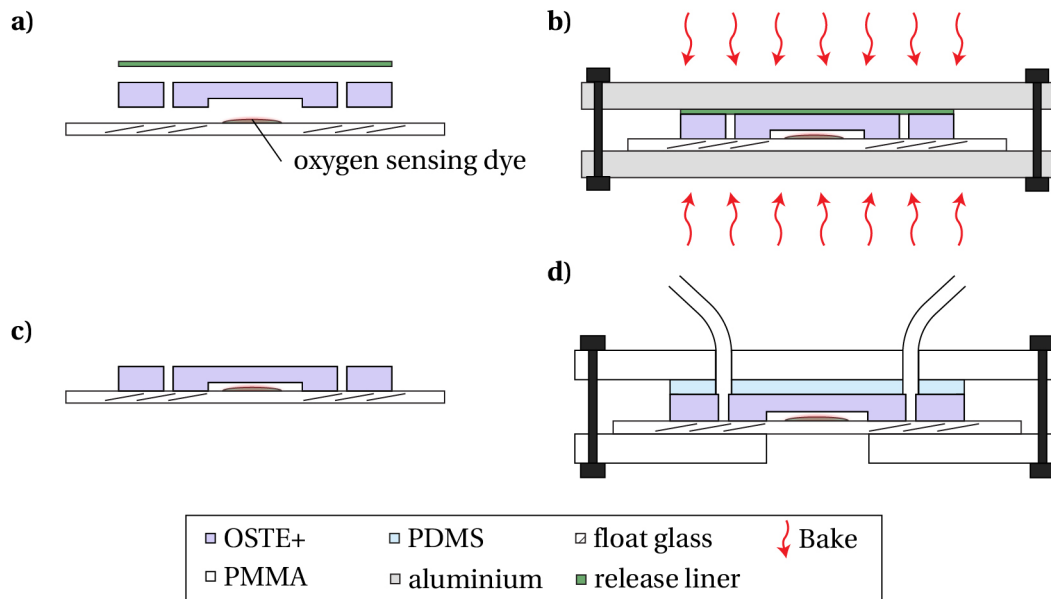


Figure 3.7 – Illustration of the OSTE+ chip assembly process. **a)** Alignment of the flexible, molded OSTE+ microfluidic chamber to the glass slide containing a spot of oxygen sensing dye. A piece of release liner foil is used to protect the top side of the chip from bonding to the metal required during the following curing step. **b)** Heat curing of the chip in a metal pressure clamp at 110 °C for 2 h. **c)** Bonded chip. **d)** Chip assembly including fluidic connections in a custom laser-cut PMMA mold, where a PDMS slab with the microfluidic tubing connections is clamped against the OSTE+ chip.

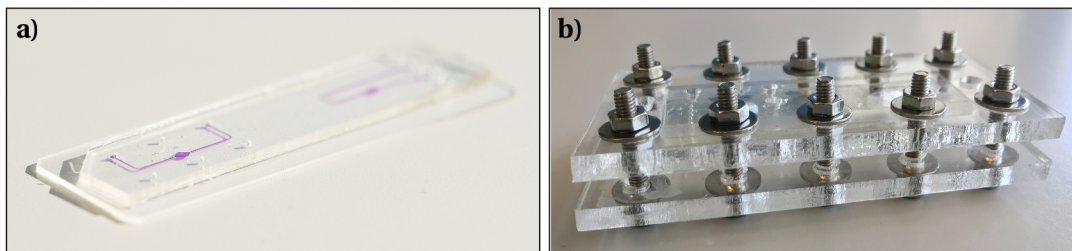


Figure 3.8 – Photographs of the final OSTE+ chips and chip assembly. **a)** Photograph of the finished OSTE+ chip with two culture chambers, without PMMA clamp and fluidic connections (corresponding to Fig. 3.7c). The channels are highlighted with a purple liquid. **b)** Photograph of the final chip assembly (corresponding to Fig. 3.7d).

3.5 Experimental

3.5.1 Experimental setup

The experimental setup for imaging, culture and oxygen sensing of on-chip worms is shown in Fig. 3.9. For imaging, the mold containing the chip was directly integrated onto an inverted microscope (Axio Observer, Zeiss, Germany) with a LED illumination system (Visitron Systems GmbH, Germany), a B/W CCD camera (ORCA-ER, Hamamatsu, Japan) and a motorized xyz stage (Visitron Systems GmbH, Germany). The camera and stage were controlled with the VisiView imaging software (Visitron Systems GmbH, Germany). On-chip oxygen concentration sensing is performed with a Piccolo2 oxygen meter (described in section 3.4.2). During OCR measurements, the chip assembly is transferred directly on top of the oxygen meter. The control and read-out of the device is performed with the Pyro Oxygen Logger software (pyroscience, Germany). Flows applied to the microfluidic chip were controlled with external programmable high-precision syringe pumps (neMESYS Low Pressure syringe pump, Cetoni GmbH, Germany), which were controlled with the Nemesys UserInterface software (Cetoni GmbH, Germany). The syringes were equipped with a custom magnetic stirring system to prevent sedimentation of *E. coli* HT115 that is used for on-chip feeding of the worms. The stirrer consists of a magnet attached to a DC motor (Arduino, Ivrea, Italy) fixed in proximity of the syringe containing the bacteria suspension and a small magnet. An Arduino microcontroller (Arduino UNO, Ivrea, Italy) was programmed to switch the on motor every few minutes for a couple of seconds to agitate the magnet for stirring the bacterial suspension.

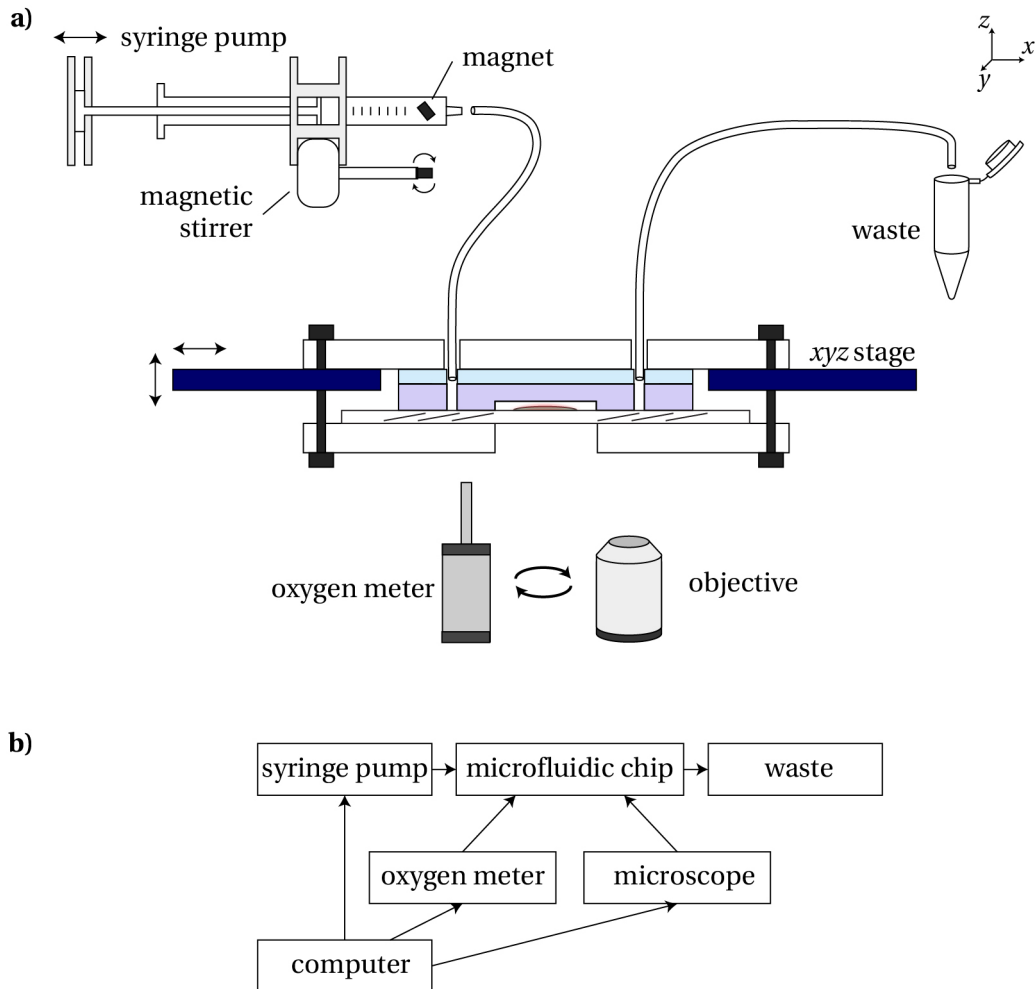


Figure 3.9 – Setup for microfluidic culture of *C. elegans* worms and OCR experiments. **a)** Illustration of the main components of the setup. The microfluidic chip containing the culture chamber is mounted with the custom mold (center). Fluidic connections on the inlet side are made to the syringe pump. A rotating magnet actuated by a microcontrolled DC motor induces stirring of the syringe contents by a small magnet in the syringe. The fluidic connection on the outlet side is connected to a waste reservoir. The chip assembly is mounted directly into the motorized *xyz* stage of an inverted microscope. Access for the microscope lens and the optical fiber of the oxygen meter is provided by an opening in the chip assembly. During OCR measurements, the chip assembly is transferred on top of the oxygen meter. **b)** Schematic diagram of the main components of the setup. A computer is used to control imaging, syringe pumps and the oxygen meter read-out.

3.5.2 Worm chip design and worm loading

The OSTE+ microfluidic chip with integrated luminescence-based oxygen sensing for long-term culture and for OCR quantification of *C. elegans* nematodes is shown in Fig. 3.10a. It comprises a single worm chamber (height $h = 80 \mu\text{m}$) with a media inlet and a media outlet. The shape of the chamber is circular (diameter $d = 2 \text{ mm}$) and tapers towards the inlet and outlet to prevent bubble formation during perfusion of the channels. The total volume of the chamber is approximately $0.25 \mu\text{l}$. The oxygen sensing dye, visible in black in the bright-field microscopy image in Fig. 3.10b, is integrated in the center of the microchamber. Filter structures for the trapping of L4 worms are integrated near the inlet and outlet sides of the chamber. The shape and dimensions of these filters are illustrated in Fig. 3.10c and microscopy images are shown in Fig. 3.10d. A filter spacing of $24 \mu\text{m}$ near the chip inlet ensures that L4 worms may pass unharmed during worm loading when flows are applied towards the outlet, but prevents the organism from escaping with its own force in stopped flow conditions. Near the outlet, a filter spacing of $15 \mu\text{m}$ was implemented to prevent L4 worms from passing, but large enough to flush away dust particles and bacteria, thereby preventing clogging of the microchamber. The initial loading procedure of a single worm before on-chip culture in the chamber is performed manually by picking a worm from an agar plate and sucking it into a piece of fluidic tubing using a syringe. Subsequently the tube is connected to the inlet channel of the chip and the liquid is injected until the worm passes the inlet-side filter structures.

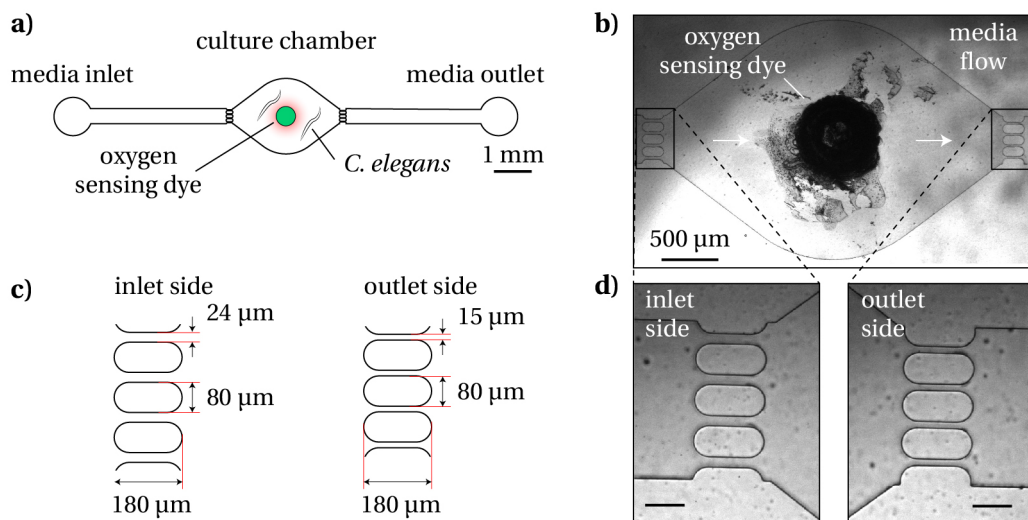


Figure 3.10 – Microfluidic culture chamber with integrated luminescence-based oxygen sensing for the culture of *C. elegans* worms. **a)** Microfluidic channel layout of the culture chamber. Filter structures on both the inlet and outlet side allow the loading and trapping of individual L4 *C. elegans* worms. In the center of the chamber, a spot of oxygen sensing dye is integrated. **b)** Bright-field microscopy image of the culture chamber with the oxygen sensing dye (black deposit in the center). **c)** Illustration of the filter dimensions on the inlet and outlet side of the chamber for trapping of L4 worms. **d)** Zoomed views of the filter structures (scale bar of the zoomed images $100 \mu\text{m}$).

3.5.3 Sensor calibration

Oxygen sensor spots need to be calibrated individually to ensure precise measurement of dissolved oxygen levels on-chip. Hereby, it is important that the calibration and all measurements are performed at constant ambient temperature, as the luminescence of the sensors is temperature-sensitive. We used a 2-point calibration procedure that is directly executed in the Pyro Oxygen Logger software [152]. Two calibration standards (at 0 % and 100 % dissolved oxygen) in water were chosen and prepared for injection on the chip with the sensor spot. The 0 % standard was obtained by adding 30 g/l Na₂SO₃ to DI water. Na₂SO₃ is a strong reductant that 'scavenges' oxygen molecules in a chemical reaction. The saturated 100 % dissolved oxygen in water calibration solution was obtained by vigorously shaking S-medium in a Falcon tube, while repeatedly opening the lid to permit fresh air to enter the headspace. Following the chip assembly, the chips were thoroughly perfused with 70 % ethanol solution to clean and sterilize the channels. Additionally, ethanol flushes potential air bubbles from the channels. A rinsing step with DI water was performed to remove all remaining ethanol from the chip. To calibrate, the 0 % standard was injected and the zero-point was set manually in the custom calibration panel of the Pyro Oxygen Logger software after residual on-chip flows had stopped and the sensor readings in the software had stabilized. Subsequently, the 100 % oxygen saturated S-medium was injected to remove the Na₂SO₃ solution from the chip and to define the point of complete oxygen saturation in the software, again after residual flows have stopped and sensor reading have stabilized. After thorough rinsing and completing the calibration procedure, the chip is ready for experimentation, *i.e.* loading of the worms on chip for culture.

3.5.4 Materials for metabolic assays and on-chip worm culture

C. elegans N2 wild type worms were obtained from the CGC. Standard NGM agar plates were provided by the EPFL Solution Preparation Facility (EPFL-SV-IN). *E. coli* OP50, S-basal medium and S-medium were prepared following standard protocols [22]. An *E. coli* OP50 bacterial lawn was added to the center of the NGM agar plates, on which worm populations were subsequently grown at room temperature [2]. Age-synchronized worm populations were obtained by a worm bleaching protocol (adapted from Stiernagle *et al.* [22], described in Krenger *et al.* [154]), followed by incubation of the embryos at room temperature until L1 hatching. Subsequently, 500 to 1000 L1 larvae were seeded on fresh NGM plates. The plates were then incubated for a duration of approximately 28 h at room temperature or until L4 larvae or YA worms were obtained for experiments. For on-chip feeding of the worms, a suspension of tetracycline-resistant *E. coli* HT115 bacteria was prepared by inoculation of a frozen stock into L-broth medium containing 10 µg/mL tetracycline and shaking overnight at 37 °C. Afterwards, the L-broth was removed by centrifugation, then the *E. coli* HT115 pellet was resuspended in freshly filtered S-medium and vortexed until a uniform bacteria suspension was obtained. Optical density measurements (OD600) were used for the determination of the bacteria concentration in the medium and for preparing a stock concentration of 4×10^9 /mL *E.*

coli HT115. For metabolic assays of the worms, FCCP powder, DMSO and a 100 mmol/l sodium azide solution were purchased from Sigma Aldrich (Switzerland). S-medium containing 30 μ mol/l FCCP was prepared by first diluting FCCP powder in DMSO to a 10 mmol/l stock solution, then diluting the stock in S-medium to obtain the final concentration. Sodium azide solution was directly diluted in S-medium to a concentration of 40 mmol/l. Luer lock dosing needles (Dosiernadel Gr. 22, H. Sigrist & Partner AG, Switzerland) were used for the connection of the Tygon flexible plastic tubing (ID 0.5 mm, OD 1.5 mm, AAD04103, Saint-Gobain Performance Plastics, France) to the syringes (Luer-Lok 1 mL, Becton Dickinson, USA).

3.5.5 Assay protocols

A microfluidic chip-based system for automated on-chip culture of *C. elegans* worms and for on-chip quantification of worm oxygen consumption from L4 stage to adulthood was developed (section 3.5.2 and Fig. 3.10). The experiments were performed after perfusion and debubbling of the chip and calibration of the oxygen sensing dye (section 3.5.3) using the custom experimental setup that was described in section 3.5.1 and Fig. 3.9.

Metabolic assay of *C. elegans*

Worms were washed from a synchronized population on a NGM agar plate and collected in a piece of fluidic tubing that was connected to a syringe filled with bacterial feeding solution, and then gently injected through the chip inlet. Basal respiration of the trapped worm was assayed in stopped flow conditions, during which data acquisition of the on-chip oxygen levels $cO_2(t)$ occurred during 20 min, after which cO_2 levels were replenished by perfusion of the culture chamber with fresh S-medium. Subsequently, S-medium containing 30 μ mol/l FCCP was injected to measure maximal respiration rates during uncoupled respiration. Lastly, 40 mmol/l sodium azide was used to inhibit respiration in worms and to obtain baseline OCR values similar to control consumption rates. OCR measurements for each condition were repeated $n = 3$ times. The protocol corresponds to a standard metabolic assay as illustrated in section 1.2/ Fig. 1.5.

Automated on-chip culture of *C. elegans*

A single L4 or adult worm was loaded in the culture chamber according to the manual protocol described in the previous experimental protocol (section 3.5.5). During the culture experiment, the worm stayed trapped in the microchamber due to the filter structures blocking the inlet and outlet channels. After the worm loading, the automated culture protocol was initiated. The syringe pump of the setup was programmed to continuously repeat a culture/feeding phase with a duration of 30 min, followed by a OCR measurement phase with a duration of 30 min. This cycle with a total duration of 1 h was repeated until the end of each experiment. A schematic of the exact flow protocol for the culture is shown in Fig. 3.11. The figure shows

3 full cycles with the feeding and measuring phases. More specifically, the feeding phase consists of an initial 15 s flow pulse in order to eject hatched larval worms from the culture chamber. Then, a slower continuous flow of bacterial food solution (20 nl/s) was applied for a duration of 30 min. This phase is the main feeding phase and serves also for replenishing on-chip oxygen for respiration. Subsequently, a 30 min long measurement phase, where no flows are applied to the chip, is performed. Even in stopped flow conditions, on-chip oxygen concentration levels in the culture chamber might still be replenished by diffusion through the filter structures from adjacent microchannels. The oxygen diffusion rate Q was estimated using:

$$Q = D \times \frac{\Delta c O_2}{l} \times A, \quad (3.4)$$

with the diffusion coefficient D , the oxygen concentration difference $\Delta c O_2$ between culture chamber and adjacent microchannels, length l of the filter structures and the total cross-sectional area of the gaps between the filter structures A . In our case, for oxygen diffusion originating from 2 microchannels into a culture chamber with zero O_2 levels, $Q \approx 1.7 \times 10^{-3}$ pmol/min. As a consequence, we can deduce that diffusion through the filters is negligible.

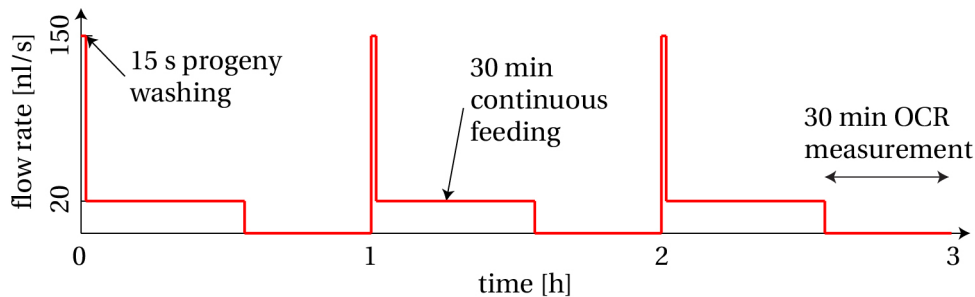


Figure 3.11 – Flow protocol for on-chip culture of L4 and adult worms. Food in form of bacteria was injected into the chip in cycles with a duration of 1 h over the full duration of the experiment (3 cycles shown). Each cycle comprises a purging pulse to wash hatched progeny out of the culture chamber, 30 min continuous feeding and replenishment of the on-chip oxygen supply, and 30 min of stopped flow for the measurement of the worms OCR.

3.5.6 On-chip OCR measurement protocol

The measurement of the oxygen concentration in the culture chamber occurs during the culture protocol in an automated manner. As illustrated in Fig. 3.11, each culture phase is followed by a 30 min stopped flow measurement window, where the oxygen supply into the chamber containing the worm is stopped. In Fig. 3.12a, on-chip dissolved oxygen (DO) concentrations $c_{O_2}(t)$ during 3 culture/measurement cycles are shown for a control measurement (blue curve) and for a single worm OCR measurement (black curve). For the control measurement, the culture chamber was perfused with a concentration of 2×10^9 /ml units of *E. coli* HT115 in S-medium. During perfusion phases of the cycles, where slow flows are applied to provide a continuous influx of nutrients, the on-chip DO concentration in the experiment control (no worm) stays constant with maximal values at $250 \mu\text{mol/l}$, meaning that oxygen is supplied in addition to nutrients. During the measurement windows, DO is decreasing in a linear manner due to O_2 uptake by the *E. coli* HT115 bacteria, as well as the OSTE+ material itself (see Discussion 3.7). To extract the corresponding OCR value from the time-dependent $c_{O_2}(t)$ curves (baseline), a linear fit over a duration of 1500 s was automatically performed over all measured cycles using a custom MATLAB fitting algorithm. The OCR corresponds to the slope of the fitted line in units of $\mu\text{mol}/(1\text{s})$. Using the chamber volume of $\approx 0.25 \mu\text{l}$, the data was converted to units of pmol/min for easier comparison to reference data.

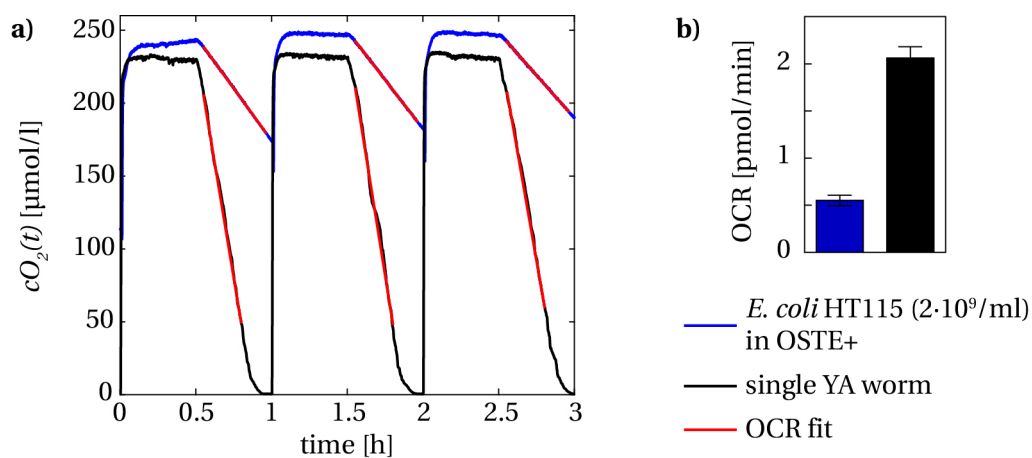


Figure 3.12 – On-chip OCR control measurements and representative single-worm experimental oxygen concentration curves. **a)** The graph shows the on-chip oxygen concentration of an OSTE+ chip during the culture/measurement cycles of control measurements (blue curve) and single YA worm (38 h) (black curve). During the control measurements, the chip was filled with the feeding suspension of living but inactive *E. coli* HT115 bacteria (2×10^9 /l) in S-medium. During the OCR measurement periods, the flow was stopped. A linear fit was used to determine the OCR of both the OSTE+chip and bacteria suspension (red curves). The experimental curves, where a nematode is present on-chip together with the bacteria suspension, show a larger OCR compared to the control measurements. **b)** OCR values extracted from a) representing the slopes of the linear fits of the oxygen concentration measurements. The bars represent the mean \pm SD of the three cycles for the control and the experimental curve (corrected by subtraction of the control measurement).

Chapter 3. Indirect calorimetry of *Caenorhabditis elegans* worms

For OCR measurements containing worms in the culture chamber, the same culture/measurement cycle-based protocol was applied. Here, the microchamber contained the bacterial suspension and the worms. As for the control, OCR values were obtained by linear fitting of the measurement portion of the cycle (fit duration 900 s in the presented case). Subsequently, the baseline OCR value obtained from the control measurements was subtracted from these OCR values, to obtain exclusively the OCR-contribution of the sample of interest. In Fig. 3.12b, the mean \pm SD values for the control, as well as the mean \pm SD OCR values of an approximately 38 h old nematode are shown (averaged over three cycles). For longer experiments starting from L4 worms that continue for several days until the worm reaches old age, up to 1 day lasting culture/measurement cycles were implemented before the bacterial food source in the syringe was depleted and needed to be manually refilled. For imaging, the chip assembly is transferred manually to the inverted microscope.

3.6 Results

3.6.1 Optimization of OSTE+ fabrication

Excluding the fabrication of the SU-8 master, the OSTE+ microfluidic chips were fabricated outside of the cleanroom using only standard equipment including an UV lamp and an oven. As the polymer remains elastic after the first curing step, the chips were directly molded from the SU-8 master. However, two main limitations during the custom replica molding process, concerning especially the smallest features of the filter structures, had to be addressed. Small gas bubbles get trapped in the negative filter patterns in the SU-8 master after filling the Al, NBR and PMMA mold with uncured OSTE+ polymer (Fig. 3.6), even after complete outgassing of the polymer. The resulting filter structures can not be used (Fig. 3.13a). To prevent such defects, the SU-8 masters were silanized with TMCS prior to OSTE+ molding. Microchips fabricated using silanized wafers showed high-quality filter structures (Fig. 3.13b). Second, the size of the filters was critical for successful demolding. OSTE+ pillars with a width $w \leq 25 \mu\text{m}$ remained attached in the master during demolding, rendering the fabricated chips as well as the master useless. Filters with larger pillar size ($w = 80 \mu\text{m}$) demolded without problem, even for small spacings ($5 \mu\text{m}$) of the pillars.

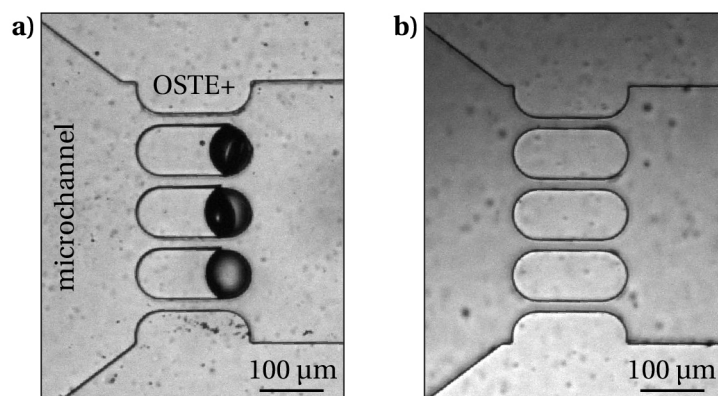


Figure 3.13 – Optimization of OSTE+ microfluidic chip fabrication. **a)** Microfluidic OSTE+ filter structures (spacing = $15 \mu\text{m}$) fabricated without silanization of the SU-8 replica mold. Air bubbles have been captured in the filter structure. **b)** Microfluidic filter structures (spacing = $15 \mu\text{m}$) using a silanized replica mold. Scale bar = $100 \mu\text{m}$.

Microfluidic chip fabrication in the OSTE+ polymer system offers the possibility for easy scaling-up of the process after initial prototyping. After optimization of the fabrication process, the OSTE+ microchips offer similar quality as PDMS chips, however small features are more difficult to fabricate.

As discussed in section 3.4.1, OSTE+ chips are biocompatible and have a low oxygen permeability. However, it is known that OSTE+ chips have oxygen scavenging properties that depend on curing time and temperature of the second curing step and on the chip surface to volume ratio [155] (see Discussion 3.7). Therefore, these parameters (detailed information in section 3.4.3) were carefully controlled during the fabrication of our chips.

3.6.2 On-chip metabolic assay of *C. elegans*

Our integrated microfluidic approach enables sensitive OCR measurements down to single-worm resolution. To evaluate basal- and maximal respiration rates during coupled and uncoupled respiration of *C. elegans* worms on-chip, we recorded $cO_2(t)$ curves of worms in untreated and FCCP treated conditions. The assay was performed according to the protocol described in the experimental section of this chapter (section 3.5.5). Fig. 3.14a shows experimental $cO_2(t)$ curves recorded with an on-chip population of 2 L4 worms in 4 different conditions (mean \pm SD of $n = 3$ repetitions of the OCR measurement on the same worm populations). OCR values are determined by the slope of a linear fit of the corresponding $cO_2(t)$ curve (section 3.5.6).

In a control condition without on-chip worm population (blue curve), the OCR contribution of the OSTE+ material and any potential contributions from the culture media are determined. After trapping the worms in the culture chamber filled with S-medium, on-chip DO is consumed rapidly in a time span of ≈ 15 min (black curve), indicating the dominant contribution of the two worm to the DO depletion. After FCCP treatment, on-chip oxygen levels decreased even faster with respect to the untreated worm condition, as is expected for worms during *uncoupled respiration*. As a further control experiment, worms were exposed to high concentrations of sodium azide in order to inhibit worm respiration. The depletion rate of DO reverts back to control conditions, indicating stopped respiration.

In Fig. 3.14b, mean \pm SD OCR values extracted by linear regression of the experimental data from Fig. 3.14a are shown. The presented data has been adjusted to account for the oxygen scavenging rate of OSTE+ (blue curve) by subtraction of the control OCR value obtained without worms on-chip. Specifically, control OCR values of the OSTE+ microchip perfused with S-medium result in a consumption rate of (1.3 ± 0.3) pmol/min. Mean values after subtraction of the consumption were normalized by the worm number ($n = 2$). For a single untreated L4 worm in basal respiration conditions, we found an OCR value of (1.8 ± 0.3) pmol/min per worm. The value increased by a factor of ≈ 2 to (3.4 ± 0.6) pmol/min per worm during uncoupled respiration after treatment with FCCP. After killing the 2 worms with sodium azide, OCR values returned back to control conditions, *i.e.* approach ≈ 0 , indicating no contributions from non-mitochondrial respiration ((-0.10 ± 0.04) pmol/min). Fig. 3.14c shows a bright-field microscope image of the 2 L4 worm population trapped in the microfluidic culture chamber.

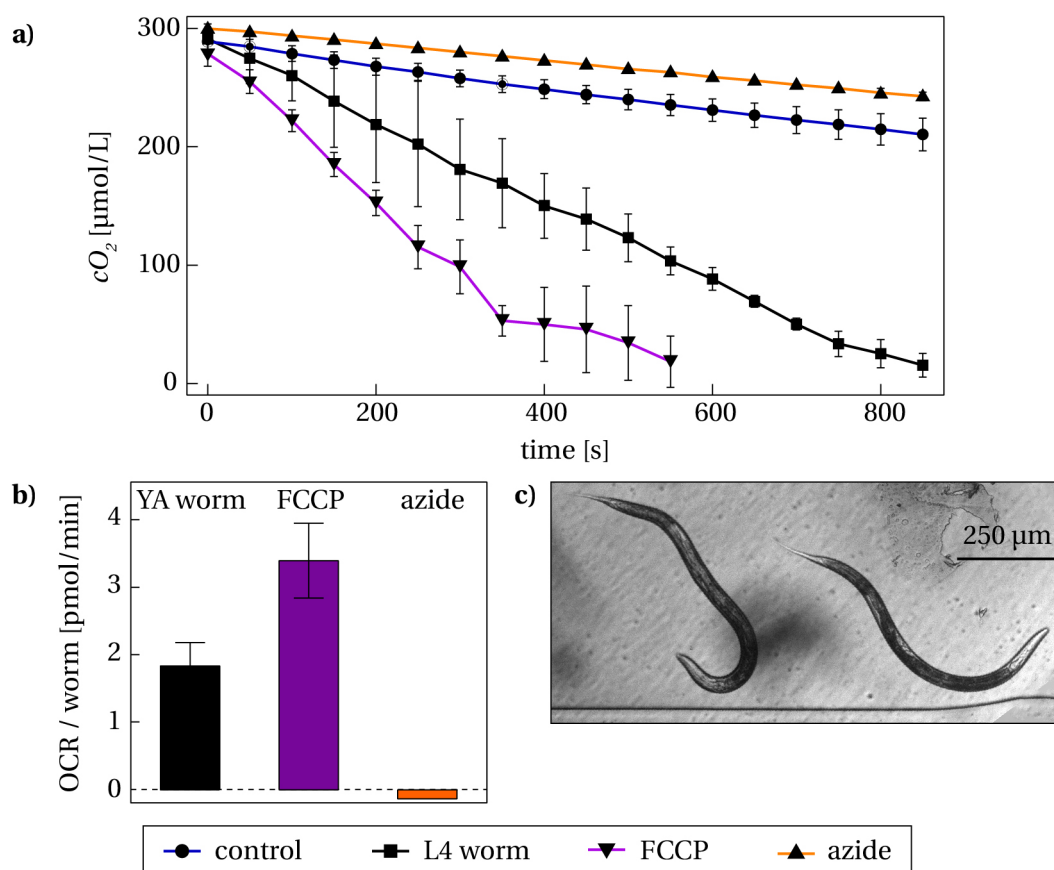


Figure 3.14 – Metabolic assay of L4 worms using FCCP and sodium azide. **a)** Mean \pm SD experimental $cO_2(t)$ curves during a metabolic assay with 2 L4 worms in the microfluidic culture chamber, and a control experiment without worm (blue curve) ($n = 3$ for all conditions). Upon FCCP treatment (purple curve), $cO_2(t)$ depletes faster than in the untreated condition (black curve), indicating maximal respiratory capacity during uncoupled respiration. After treatment of the worm population with sodium azide, $cO_2(t)$ approaches the control condition, indicating worm death. **b)** Extracted OCR values by linear regression of the $cO_2(t)$ experimental data. After fitting, control OCR values were subtracted from the resulting slopes of the experimental curves, and the values were normalized by the worm number. Single worm OCR increased by a factor of ≈ 2 after FCCP treatment, and decreased to ≈ 0 after azide treatment. **c)** Bright-field microscope image of the two L4 worms on-chip.

3.6.3 OCR measurements during long term culture of *C. elegans* on-chip

A further proof-of-concept study related to long term on-chip culture of a single worm has been performed in our microfluidic system. In this assay, a single L4 worm was trapped in the culture chamber for 7 days with a constant supply of a *E. coli* HT115 bacterial food source to allow development of the nematode. At the same time, OCR measurements using our integrated sensor were performed in regular intervals. Detailed information on the worm culture protocol and OCR measurement cycles is provided in sections 3.5.5 / 3.5.6 and Fig. 3.11 / 3.12. In Fig. 3.15, bright-field microscopy images of the aging worm are shown. The L4 larval worm was loaded on the chip at an age of 40 h after seeding L1-arrested worms on a NGM plate containing bacterial food (Fig. 3.15a). At a worm age of 58 h, the worm developed to a YA worm (Fig. 3.15b), and at an age of 74 h the worm was an egg-laying adult (Fig. 3.15c). In Fig. 3.15d, an image with larger magnification shows the worm pharynx and an embryo in the late twitching stage a few moments before hatching. Using the microfluidic trap in combination with the custom automated flow profile allows offspring to be washed away from the culture chamber after hatching, thus preventing contributions to OCR measurements.

Compared to nematodes growing on standard NGM agar plates, lagging development of the single on-chip worm was observed during our proof-of-concept assay, likely due to lower on-chip oxygen levels (see Discussion 3.7). Results of OCR quantification during long term culture of the worm on-chip are shown in Fig. 3.16. The plot shows all OCR values (red dots) obtained by fitting $cO_2(t)$ depletion by linear regression to extract the slopes of the curves (according to the protocol explained in detail in section 3.5.6 and Fig. 3.12). To compute the OCR profile of the worm (black curve), single OCR data points were averaged over 12 h ($n = 12$ data points) and plotted with corresponding SD (black curve). The OCR profile of the single worm shows an expected increase of respiration rates from larval to adult worm, and a decrease when the worm reaches old age. Initial mean OCR values at worm age = 46 h are equal to (2.2 ± 0.3) pmol/min per worm and increase to a maximum value of (3.4 ± 0.7) pmol/min at worm age = 70 h. From this point forward, an overall decrease of OCR values is observed. The lowest OCR value (1.5 ± 0.7) pmol/min was measured in an old worm (age = 166 h).

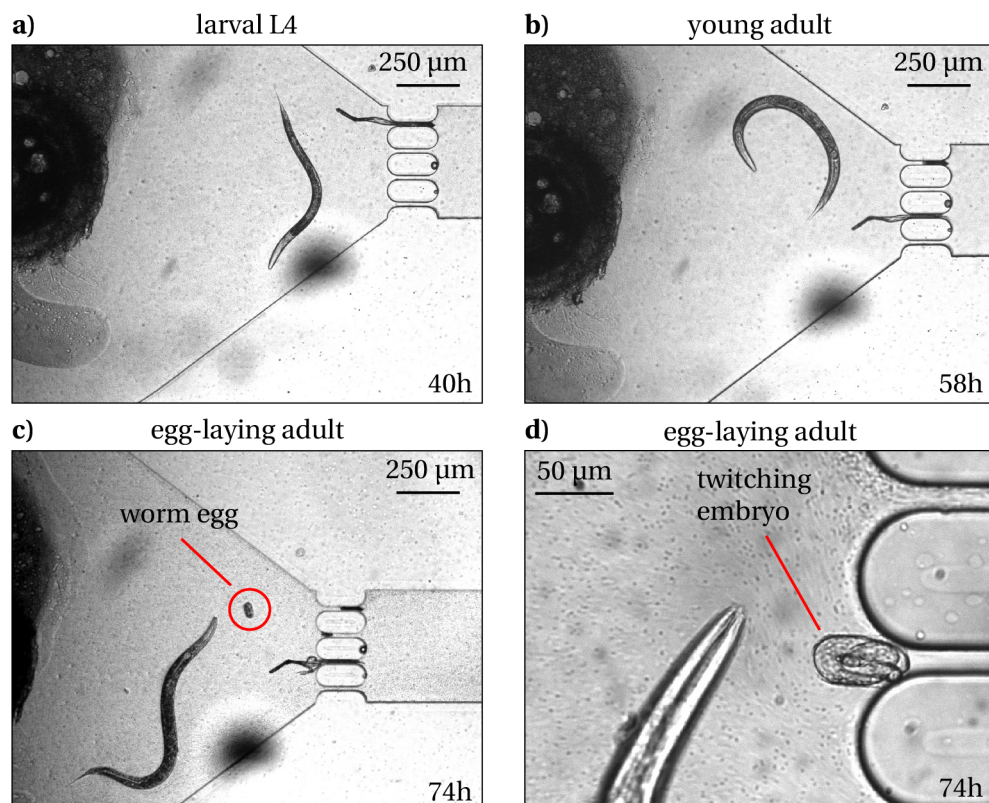


Figure 3.15 – Bright-field microscopy images during single worm culture on-chip. **a)** Freshly loaded L4 larval worm (age \approx 40 h) in the culture chamber, where it is trapped by the filter structures near the inlet and outlet channels. **b)** The larvae developed into a YA worm (age \approx 58 h). **c)** Egg-laying adult (age \approx 74 h). **d)** Zoomed view on the pharynx of the worm (age \approx 74 h) and an offspring embryo in the twitching stage. The presence of *E. coli* HT115 bacteria is clearly visible in this image.

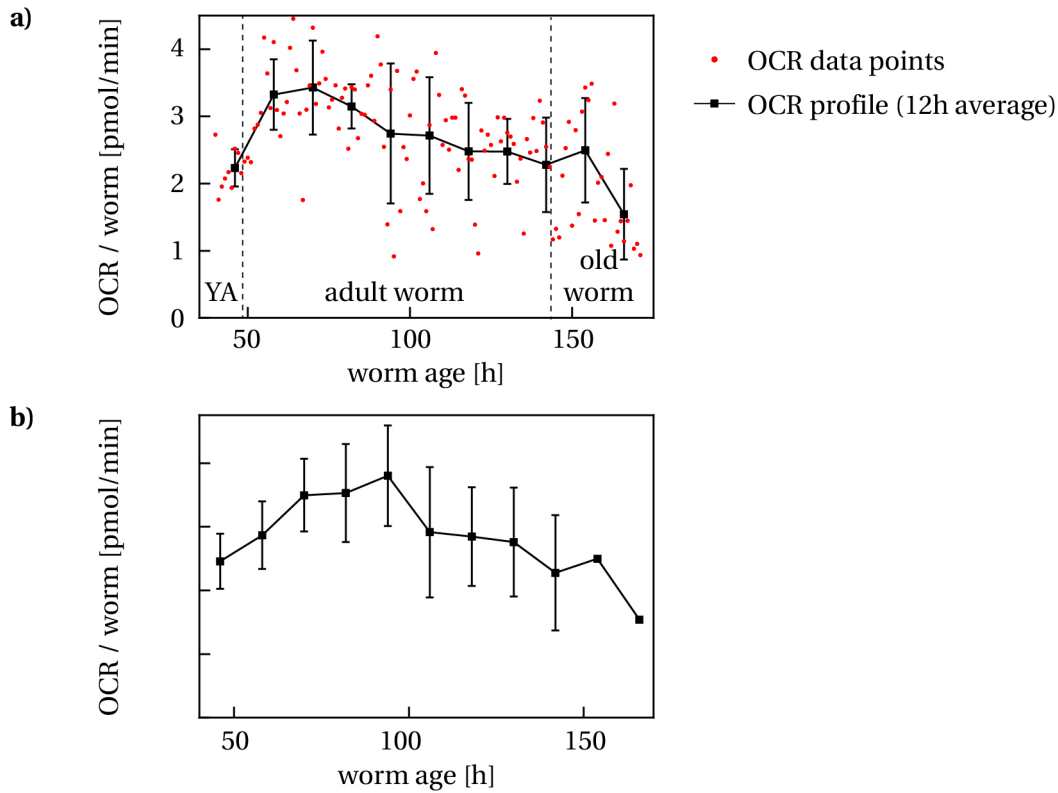


Figure 3.16 – Single worm long term measurements of OCR on-chip. **a)** A 40 h old YA worm was cultured in the OSTE+ chip according to the protocols explained in section 3.5.5 and Fig. 3.11. The OCR values (red dots) were obtained during the 30 min stopped-flow oxygen detection phase of every feeding/measurement cycle (cycle duration of 1 h), where the worm consumes the oxygen available on-chip. OCR values were averaged over 12 cycles and presented as mean \pm SD (black curve). The data shows an increase in the single worm OCR from the YA stage to the adult egg-laying worm. After peak consumption rates are reached, values decreased continuously. A large OCR drop was measured in worms older than 150 h. **b)** Averaged OCR profiles from single worm assays ($n = 3$ up to ≈ 100 h.)

3.7 Discussion

We took advantage of the off-stoichiometry dual-cure thiol-ene-epoxy OSTE+ for the fabrication of microfluidic devices for on-chip luminescence-based OCR measurements of *C. elegans*. OSTE+ is a versatile and cheap material for fast prototyping of microchips with feature sizes in the μm -range. We implemented a new protocol for the fabrication of OSTE+ microchips for *C. elegans* culture. In contrast to highly gas-permeable PDMS chips, OSTE+ has a very low gas permeability and does not immediately replenish on-chip oxygen levels. We took advantage of these material properties when measuring the depletion of diluted oxygen in a microfluidic chamber, and we were able to determine the variation of the oxygen concentration that corresponds to the OCR of the biological sample in the microchip. For the quantification of the OCR of living organisms in OSTE+ microfluidic chips, one must consider the oxygen scavenging properties of this polymer. In a recent study, Sticker *et al.* used oxygen scavenging of OSTE+ for oxygen depletion in biochips for culture of anaerobic bacteria [155]. The authors performed a series of experiments for characterizing oxygen scavenging by the material and discovered that this property strongly depends on the curing time and temperature of the resin, as well as on the surface-to-volume ratio of the chip itself, defined by the geometry. High curing temperatures of up to 130 °C and long curing durations of up to 6 h decreased the oxygen absorption of OSTE+, mainly because of a reduction of the number of free thiols on the chip surface, reduced bulk polymer oxidation and an increase of the polymer density. In our work, we carefully adjusted fabrication parameters in this range in order to minimize the effect of oxygen absorption of OSTE+. We therefore could exclude any adverse effect on the reliability and reproducibility of our on-chip OCR experiments with living samples.

Using our microfluidic platform, we were able to quantify the variation of respiration rates of *C. elegans* worms upon treatment with the uncoupling agent FCCP and the metabolic inhibitor sodium azide. Similar assays have also been performed by Huang *et al.* in a microdevice and in the Seahorse XF96 respirometer [106, 132]. However, their system, as well as the device described by Suda *et al.* and Seahorse respirometers, were not suitable for long term culturing applications (section 3.3) [131, 106, 132]. In these studies, coupled respiration rates increased by a factor of ≈ 2 upon treatment with FCCP, *i.e.* during the state of uncoupled respiration, where maximal cellular respiration in mitochondria occurs (section 1.2). After treatment with sodium azide, the authors could measure small OCR values related to residual non-mitochondrial respiration. Our assays confirm increased OCR of *C. elegans* worms on-chip after FCCP exposure (Fig. 3.14). Measured basal respiration rates also increased by a factor of ≈ 2 during uncoupled respiration. In our case, however, measured respiration values approached zero level after inhibiting respiration with sodium azide, indicating no contribution of non-mitochondrial respiration. This might be due excessive on-chip sodium azide concentrations causing death of the worms.

In this work, we presented OCR measurements of *C. elegans* from larval L4 stages to late adulthood, requiring long term on-chip culture of the worms (Fig. 3.15 and Fig. 3.16). In principle, worms developed normally on-chip, however, we observed delayed adulthood,

where egg laying started only at a worm age of 74 h, *i.e.* approximately 1 day later than is expected for worms growing on standard agar culture plates (refer to worm life cycle in Fig. 1.2). Peak respiratory activity was measured during egg laying. We attribute this fact to the design of the experimental protocol, where the worms experience regular fluctuations of dissolved oxygen concentrations in the culturing environment. Specifically, DO is replenished only during a period of 30 min in the 1 h lasting culturing/measurement cycle. During the OCR measurement phase of the cycle, no oxygen is resupplied to the worm culturing chamber. Oxygen is consumed by the worms, resulting in complete depletion of DO in the chamber after about 15 min to 25 min (*i.e.* \approx 5 min to 15 min before refreshing the culture medium). Moreover, the concentration of dissolved carbon dioxide increases simultaneously. It has been shown that worms growing in oxygen-deficient conditions experience a slowdown in development and an increased life span [156, 157]. Additionally, *C. elegans* worms are sensitive to CO₂ and avoid elevated concentrations of it. Similar to hypoxic conditions, hypercapnia (elevated CO₂ levels) slows down development and increases life span [158]. Lower motility and reduced fertility were also observed in these conditions. Our observations are in line with results shown in these studies. We believe that the culturing protocol for this proof-of-concept study is working well for single worm assays, however, on-chip O₂ concentrations should be better controlled in future experiments. Especially when using more than one worm per chamber, hypoxic and hypercapnic conditions might become more critical. Nevertheless, this issue can be easily circumvented by optimizing the assay protocol, in particular by shortening the OCR quantification phases and extending the culture phases in fresh medium. A rough estimation reveals that oxygen molecules take approximately $t = 4$ min to diffuse over a typical chamber dimension of $l = 1$ mm (using equation 1.6 with a diffusion coefficient $D = 1.9 \times 10^{-9}$ m²/s for molecular oxygen in water [159]). We can therefore assume that during a typical measurement cycle of 30 min, oxygen in the whole chamber is consumed, not only in the proximity of the sensor spot.

When comparing our on-chip single-worm respiration rates to reference values, obtained with a commercial Seahorse XF96 respirometer (Fig. 3.2a), we notice that our OCR values are significantly lower, *i.e.* by factors ranging from approximately 2 to 5 depending on the age of the worm [106]. However, we observe a comparable overall age-dependent evolution of the OCR rates, namely with lower respiration rates during the L4 and YA stages, and for worms at old age. In both cases, the peak OCR value is measured during the reproduction phase in adult worms. Interestingly, in the Seahorse study OCR measurements had to be performed separately for each development stage, whereas in our study we were able to culture worms and measure OCR rates over the whole life span continuously. Using direct calorimetry, Braeckman *et al.* have shown that worms growing in liquid culture produce less metabolic heat (by a factor of \approx 1.6) than worms growing on NGM agar plates [58]. We expect OCR values to reduce in a similar manner in our microfluidic chip, because worms in Seahorse XF96 measurements were always taken from agar plates for experiments. This, in combination with partially hypoxic conditions, could possibly explain the discrepancy in our measured values.

3.8 Conclusion

The work presented in this chapter described a new, versatile microfluidic platform with integrated luminescence-based oxygen detection capability using an oxygen-sensing dye. The microfluidic chips were fabricated in OSTE+, a polymer that is particularly suitable for the present application thanks to its very low oxygen permeability. The fabrication process of OSTE+ microfluidic chips was optimized by developing a custom molding process, allowing reliable and scalable fabrication of rigid biocompatible chips with features in the μm -range. A microfluidic culture chamber was fabricated and optimized for the trapping and culture of *C. elegans* worms at the L4 stage. We implemented an automated feeding protocol, which at the same time enables the quantification of the oxygen consumption rate of a single living worm on the chip. We performed a proof-of-concept metabolic assay, where we quantified the effect of the mitochondrial uncoupling agent FCCP on the basal respiration rate of *C. elegans* worms in the YA stage, and compared our results to reference values obtained by a commercial Seahorse XF96 respirometer. In a second study, we measured the respiration rate of a single worm trapped on-chip during its growth from the L4 stage to an old age of 7 days.

Our system offers several advantages over standard commercial equipment for oxygen consumption measurements, *e.g.* confinement of the sample in close proximity to the oxygen sensing dye, continuous controlled feeding conditions, feasibility of long term studies, washing away of progeny and metabolic waste products, reversible injection of drugs and treatment compounds, and imaging capabilities. This is a promising technology that may be combined with other analytical methods, *e.g.* direct calorimetry, to gain new insights on the coupling of anabolic and catabolic processes in living organisms.

4 Force microscopy of *Caenorhabditis elegans* embryos

Assays focusing on emerging biological phenomena in an animal's life can be performed during embryogenesis. While the embryo of C. elegans has been extensively studied, its biomechanical properties are largely unknown. Here, we demonstrate that cellular force microscopy (CFM), a recently developed technique that combines micro-indentation with high-resolution force sensing approaching that of atomic force microscopy, can be successfully applied to C. elegans embryos. We performed, for the first time, a quantitative study of the mechanical properties of the eggshell of living C. elegans embryos and demonstrate the capability of the system to detect alterations of its mechanical parameters and shell defects upon chemical treatments: in addition to investigating natural eggshells, we exposed the eggshell to sodium hypochlorite and chitinase solutions, respectively, that selectively modified the multilayer eggshell structure, in order to evaluate the role of the different layers on the mechanical integrity of the embryo. Finite element method simulations based on a simple embryo model were used to extract characteristic eggshell parameters from the experimental micro-indentation force-displacement curves. We found a strong correlation between the severity of the chemical treatment and the rigidity of the shell. Furthermore, our results showed, in contrast to previous assumptions, that short bleach treatments not only selectively remove the outermost vitelline layer of the eggshell, but also significantly degenerate the underlying chitin layer, which is primarily responsible for the mechanical stability of the egg.

Chapter 4 was adapted from the following publications:

- **R. Krenger**, J.T. Burri, T. Lehnert, B.J. Nelson and M.A.M. Gijs, “Force-microscopy of *Caenorhabditis elegans* embryos”, in revision at Nature Microsystems & Nanoengineering.
- **R. Krenger**, J.T. Burri, T. Lehnert, B.J. Nelson and M.A.M. Gijs, “Biomechanical study of *Caenorhabditis elegans* embryos using cellular force microscopy”, Proc. of 20th International Conference on Miniaturized Systems for Chemistry and Life Sciences (microTAS 2019), Basel, Switzerland, October 2019.

4.1 Introduction

The nematode *C. elegans* is an important model for biomedical research. The mechanisms of several human diseases, including drug-target interactions, may be studied using this organism since many human disease genes and disease pathways have been conserved between *C. elegans* and humans [19, 160, 20]. The *C. elegans* embryo is also an interesting model system to study biological processes at a very early stage, e.g. the formation of functional neuronal networks [161] and fundamental cellular mechanisms, in particular asymmetric cell division [162]. The development of new therapeutic drug agents can benefit from the use of *C. elegans* as well [163].

The eggshell of its embryo has a direct impact on many early developmental events [164]. This 300 nm to 400 nm thick multilayer composite structure provides physical support and protection of the developing organism from external cues, prevents small molecules from permeating it, and blocks polyspermy [165]. For several decades, the eggshell of a nematode was thought to consist of three main layers [166, 167]. Recently two additional inner layers have been identified through electron micrographs and by diagnostic biochemical treatments. The first of the two layers was referred to as either the embryonic layer, perivitelline space, or extra-embryonic matrix [168, 169, 164, 165]. The innermost layer is called the permeability barrier layer, as it appears to be responsible for preventing small molecules from permeating [169]. Here, we focus on the three main morphologically distinct strata of the eggshell, *i.e.* an outermost thin vitelline layer (VL), a thicker middle chitin layer (CL), and an underlying chondroitin proteoglycan layer (CPGL) [165]. Each of these layers has a specific function. The VL mediates sperm-oocyte binding, CL provides the structural strength of the eggshell, and the CPGL prevents cytoplasm membrane adhesion to the CL and is required to assemble the inner permeability barrier [169]. Although one of the main functions of the eggshell is to mechanically protect the embryo, its biomechanical properties are largely unknown. Accurate sensing of changes in its mechanical integrity could offer a new way to identify genes that may up- or downregulate the synthesis of specific shell layers. To date, such biomechanical alterations have only been observed qualitatively by eye, e.g. by the loss of the ovoid egg shape, or by evaluating egg breakage rates while exiting the uterus [165].

In this work, we present an extensive and quantitative micro-indentation study of living *C. elegans* embryos using CFM to extract the biomechanical properties of the eggshell. CFM is done using a microrobotic platform for mechanical stimulation and characterization of living entities of different sizes, ranging from individual cells and tissues to full organs [170, 171]. Compared to other mechanical characterization tools used for biological samples, such as atomic force microscopy [172, 173, 174], CFM offers the possibility to apply multi-scale loads in the nN- and mN-range with significantly higher displacement, *i.e.* indentation depths in the range of several micrometers with nm-resolution. Previously, CFM has been successfully used for the characterization of the cell wall of growing pollen tubes [175, 176, 177, 178, 179, 180]. CFM is a particularly suitable tool for the mechanical characterization of *C. elegans* embryos, as it allows substantial bending and stretching of the hard eggshell with high spatial and

force resolution. To demonstrate the versatility of our method, we applied different chemical treatments to the embryos that are known to affect the eggshell multilayer structure, but are still regularly used in standard worm maintenance procedures. Embryos were exposed to sodium hypochlorite (NaOCl), a chemical used to obtain age-synchronized *C. elegans* worm populations, which selectively removes the VL [181, 182, 165], and to chitinase, an enzyme that digests the CL. Our micro-indentation study revealed that these shell-degrading treatments have a drastic effect on the mechanical integrity of the eggshell. We established a biomechanical finite element method (FEM) model of the embryo, enabling accurate fitting of the experimental force-displacement curves in order to estimate the Young's modulus of the eggshell layers under different conditions.

4.2 Cellular force microscopy setup

4.2.1 MEMS capacitive force sensors

The CFM system presented in this work is based on MEMS capacitive force sensors. This type of force sensor can be fabricated with force sensitivities from the mN- down to the pN-range, which results in a large spectrum of possible applications including biological studies, especially. Alternatives to capacitive force sensors, such as cantilever-based sensors, optical tweezers or methods involving magnetic beads, are often limited in measuring large force ranges, sensitivity, or the capability of being manufactured on a large scale [183].

The sensors used in this work (FT-S100, FemtoTools, Switzerland) consist of a probe that is suspended by a system of springs that are compliant in one direction. A bright-field microscope image of the commercial capacitive force sensor is shown in Fig. 4.1a. Capacitive force sensing is based on a comb-drive. In Fig. 4.1b, a schematic of the working principle of the sensors is shown. A force acting on the sensing probe in z direction is deflecting the springs, which causes movement of the inner movable capacitor plates connected to the probe against outer fixed capacitor plates connected to the sensor frame. When an AC voltage V_{AC} is applied between the upper and lower side of the outer sensor frame, an output voltage V_{out} can be measured at the probe. V_{out} can be calculated as follows [184]:

$$V_{out} = V_{AC} \left(\frac{C_1 - C_2}{C_1 + C_2} \right), \quad (4.1)$$

$$\text{with capacities } C_1 = \epsilon_0 \epsilon_r \left(\frac{A_1}{d_1} + \frac{A_1}{d_3} \right) \text{ and } C_2 = \epsilon_0 \epsilon_r \left(\frac{A_2}{d_2} + \frac{A_2}{d_3} \right),$$

where ϵ_r is the dielectric constant of the surrounding medium ($\epsilon_r = 1$ in air), ϵ_0 is the permittivity of free space, A_1 and A_2 the overlapping areas of the capacitor plates, and d_{1-3} the distances between capacitor plates as indicated in Fig. 4.1b. V_{out} is proportional to the inner plate displacement Δd :

$$V_{out} = V_{AC} \left(\frac{\Delta d}{d_0} \right), \quad (4.2)$$

with the plate spacing d_0 .

A standard model for two fixed beams with a central point load is used to calculate the deflection of the beams that form the spring:

$$\Delta d = \frac{F_z l^3}{4Ew^3 h}, \quad (4.3)$$

with the applied force in z direction F_z , the Young's modulus $E = 100$ GPa for silicon, and length l , width w , height h of the beams. A microscopy image of a tungsten sensor tip is shown in Fig. 4.1c.

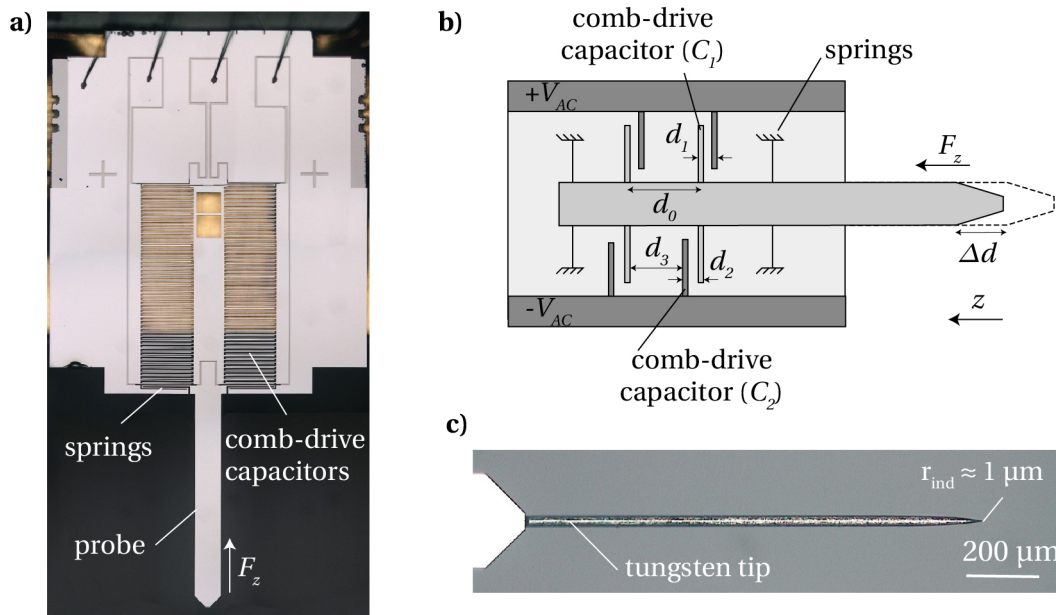


Figure 4.1 – MEMS-based capacitive force sensor. **a)** Bright-field microscope image of the FemtoTools FT-S100 capacitive force sensor with a single measurement axis. **b)** Schematics of the single-axis force sensor. Two comb-drive capacitors are suspended by a system of unidirectional springs. Upon displacement of the inner capacitor plates against the fixed outer capacitor plates due to an applied force, an output voltage V_{out} is produced. **c)** Bright-field microscope image of the tungsten tip that is fixed to the force sensor. This tip has a radius of approximately $1 \mu\text{m}$ and is in direct contact with the sample. This figure is based on [185] and [184].

4.2.2 CFM system

The CFM used for micro-indentation is shown in Fig. 4.2a and Fig. 4.2b [177, 178]. One of the main features of the CFM system is a commercially available MEMS-based capacitive force sensor (FT-S100, FemtoTools AG, Switzerland) to which the micro-indenter is attached, consisting of a tungsten wire with a shaft diameter of 22 μm and a tip radius $r_{ind} \leq 1 \mu\text{m}$ (T-4-22 Picoprobe, GGB Industries INC., USA). A schematic of the micro-indenter is shown in Fig. 4.2c. The force sensor encompasses a measurement range of $\pm 100 \mu\text{N}$ with a resolution of 15 nN, recording at a sampling rate of 500 Hz. The working principle of the force sensor is described in detail by Sun *et al.* [184]. The force sensor is fixed to the PMMA arm of an *xyz* positioner with a travel range of several cm and a closed-loop resolution of 50 nm (a stack of three SLC-2475-S, SmarAct, Germany). This *xyz* positioner is used to place the sensor probe in close proximity to the *C. elegans* embryos prior to the indentation experiment. Fine control of micro-indentation is performed by means of a piezo flexure-guided nanomanipulation system (P-563.3CD PIMars, Physik Instrumente GmbH (PI), Karlsruhe, Germany). The piezo stage allows for continuous and high-precision control of the indenter tip position with a spatial closed-loop resolution of 2 nm in *xyz* direction and a full travel range of 300 μm . The CFM system is mounted on an inverted microscope (IX71, Olympus K.K., Japan) using a 20x objective lens (LUCPlanFL N x20, Olympus K.K., Japan) and a CCD camera (Orca-D2, Hamamatsu Photonics K.K., Japan) for high-resolution bright-field imaging of the embryo samples. The microscope features a motorized *xy* stage system (M-687 PILine XY, PI, Germany) with a large travel range of 100 mm \times 75 mm and 0.1 μm resolution. Data acquisition and control was implemented in LabVIEW (National Instruments (NI), USA) and executed using a real-time computer with an integrated field programmable gate array (FPGA) (NI cRIO 9024, NI, USA). An analog output module (NI-9022, NI, USA) powers all three axes of the CFM piezo stage, and two analog input modules (NI 9215, NI, USA) monitor the *xyz* positions as well as the force signal. The accuracy of the CFM was previously tested using a Si-traceable force-standard (FS-C 15, Si-METRICS, Germany) that was calibrated and certified by the Physikalisch-Technische Bundesanstalt (PTB), the National Metrology Institute of Germany [177, 178].

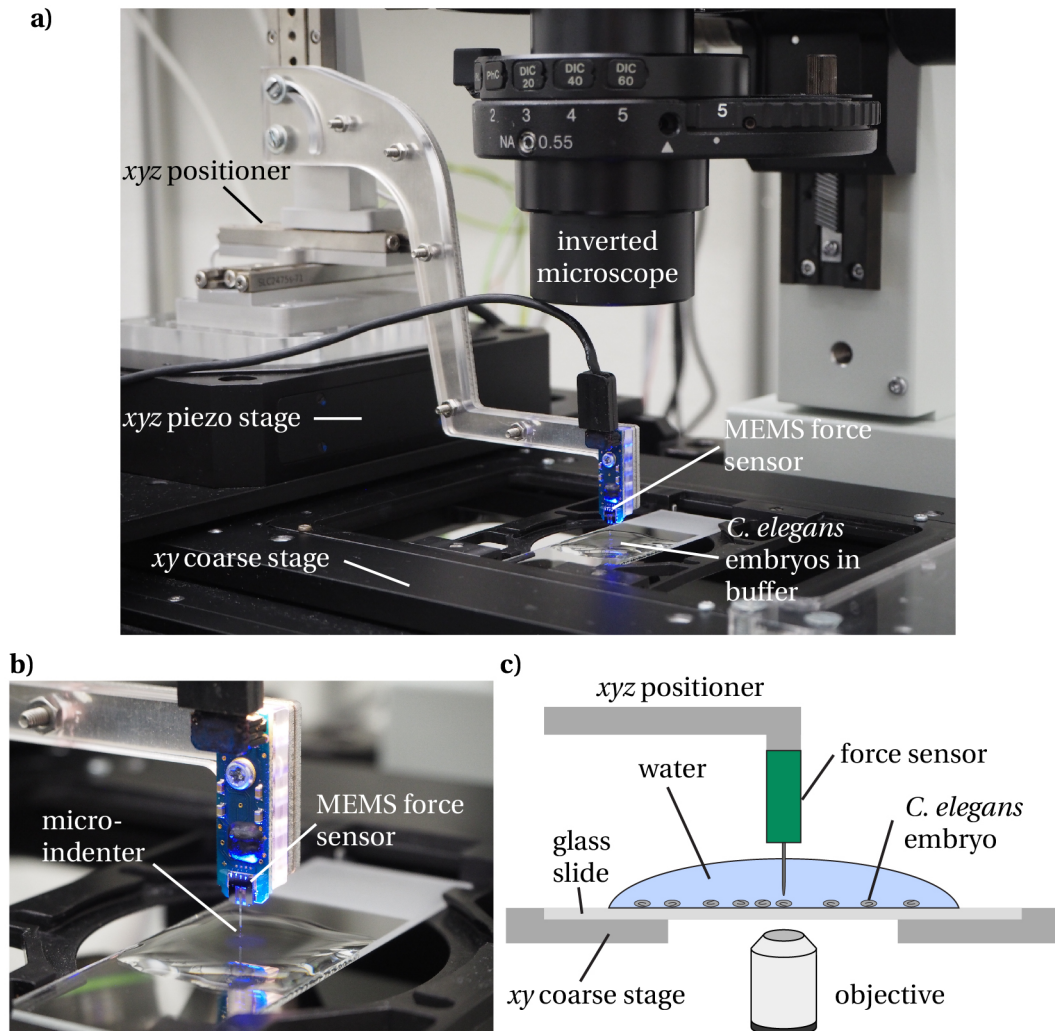


Figure 4.2 – System for micro-indentation measurements on *C. elegans* embryos. **a)** The photograph shows the CFM system, integrated with an inverted microscope for high-resolution imaging. The configuration, combining *xyz* precision linear positioners and a piezo system, allows manipulation of the MEMS-based force sensor (blue) with an attached micro-indenter with nanometer resolution and centimeter travel range. **b)** Closer view of the force sensor hovering over the samples in buffer solution. **c)** Schematics of the CFM. The sample, in this case *C. elegans* embryos, are dispensed on a standard microscopy glass slide. The micro-indenter is positioned into close proximity of the sample by means of the *xy* coarse stage of the microscope and the *xyz* positioner.

4.3 Experimental

4.3.1 Age-synchronized *C. elegans* culture and embryo harvesting

C. elegans N2 wild type worms were obtained from the CGC. Standard NGM agar plates were provided by the EPFL-SV-IN. *E. coli* OP50 and S-Basal media were prepared following standard protocols [22]. An *E. coli* OP50 bacterial lawn was added to the center of the NGM agar plates, on which worm populations were subsequently grown at room temperature [2]. Age-synchronized worm populations were obtained by a worm bleaching protocol (adapted from Stiernagle *et al.* [22], described in Krenger *et al.* [154]), followed by seeding of 500 to 1000 isolated eggs on fresh NGM plates. The plates were then incubated for a duration of approximately 64 h at room temperature until gravid adult worms were obtained. Freshly laid eggs were then harvested by scraping the surface of the agar plate with a cell scraper (Sarstedt, Germany) and collected in an Eppendorf tube. Eggs were separated from adult worms by sedimentation for 30 s and subsequent isolation of the egg-containing supernatant.

4.3.2 Eggshell treatment protocols

Fig. 4.3 shows an overview illustration of the eggshell treatment protocol that was used to obtain 4 distinct eggshell conditions using chemical treatments.

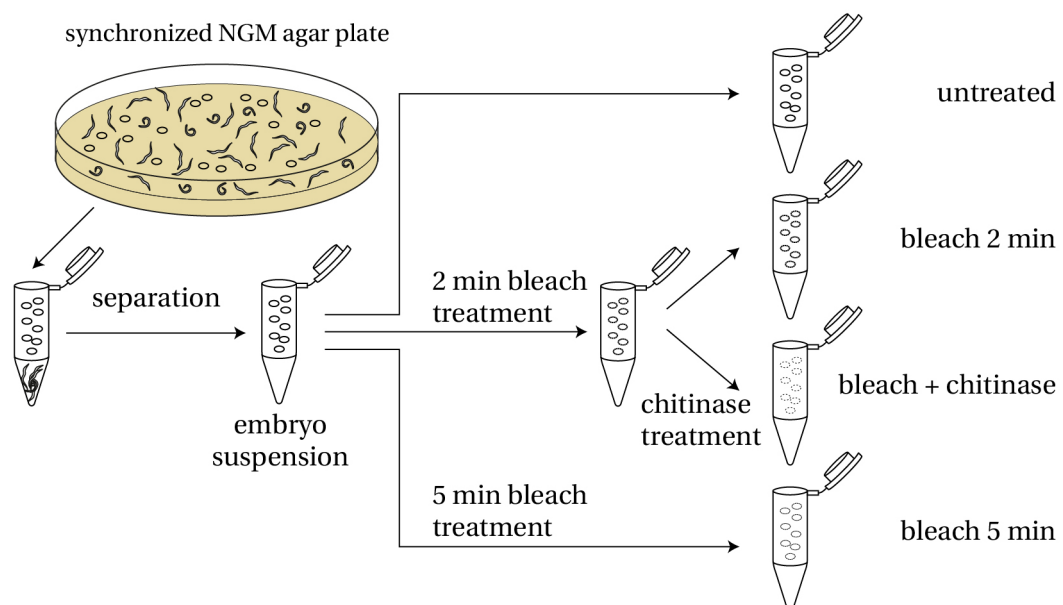


Figure 4.3 – Illustration of the eggshell treatment protocol. After collection of the adult worms and embryos from a synchronized NGM agar plate, the adults were removed from the suspension by means of sedimentation. The 2 min and 5 min bleach treatments were applied to the collected embryo suspension. The chitinase treatment was applied to 2 min bleach-treated embryos. The workflow yields a total of 4 eggshell conditions.

Chapter 4. Force microscopy of *Caenorhabditis elegans* embryos

Eggs were suspended in egg buffer (118 mmol/l NaCl, 48 mmol/l KCl, 2 mmol/L CaCl₂, 2 mmol/l MgCl₂, 25 mmol/l HEPES, pH 7.3) before applying shell treatments [186]. Untreated eggs were taken directly from this suspension. Bleach treatment was performed in a 0.27 mol/l NaOH + 2 % NaOCl solution (bleach) for 2 or 5 min, respectively. Egg samples were then washed 3 times by repeated centrifugation (≈ 1680 rcf for 60 s) and resuspended in egg buffer by vortexing. Chitinase-treated shells were obtained by suspending 2 min bleach-treated eggs in egg buffer containing 5 mg/ml chitinase from *Streptomyces griseus* (Sigma-Aldrich, Buchs, Switzerland) until the start of the experiments (*i.e.* for approximately 15 min).

4.3.3 CFM micro-indentation protocol

Micro-indentation assays were performed by means of the custom CFM system that was integrated with an optical microscope for high-resolution imaging (section 4.2.2, Fig. 4.2). Nematode embryos in egg buffer were first spotted on a standard microscopy slide, which was inserted into the sample holder of the inverted microscope. After alignment of the sensor tip above the center position and in proximity to the eggshell of a selected embryo, a series of consecutive loading cycles was performed. A micro-indentation measurement consists in controlling the indentation depth Δ_z of the sensing microprobe via the *xyz* piezo stage while simultaneously measuring the force F_z generated by the eggshell deformation (Fig. 4.4).

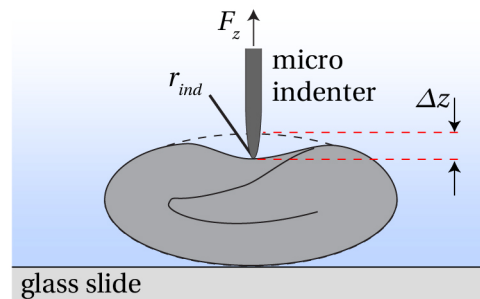


Figure 4.4 – Schematics of eggshell indentation. The indentation of the eggshell is performed by downward motion (*z* direction) of the micro-indenter, controlled *via* the *xyz* piezo stage, resulting in eggshell indentation of a distance Δ_z . The indenter tip position and the resulting force F_z are recorded simultaneously.

As a reference for measuring the indentation depth Δ_z , the *z* coordinate of the initial shell contact of the sensor tip during loading, determined at a force threshold level of 0.1 μ N, was used. The resulting force-displacement curves $F_z(\Delta_z)$ were used to extract several mechanical parameters of eggshells subjected to different chemical treatment protocols. Once a preset maximal force F_z^{max} value is reached (loading curve), indentation is stopped and the indenter is automatically retracted. Multiple successive measurements with gradually increasing F_z^{max} values were carried out up to F_z^{punct} , corresponding to the force level, where irreversible eggshell puncture occurred, typically ranging from approximately 5 μ N to 70 μ N depending on the egg treatment. A baseline drift due to viscous friction of water surrounding the sensor tip was taken into account by subtracting a linear fit of the $F_z(\Delta_z)$ curve during sensor tip

approach of the eggshell. Video sequences were recorded during indentation to monitor the morphological changes of the embryos and ImageJ was used for quantification of the morphological parameters.

4.4 Results

4.4.1 Structural and morphological changes upon indentation for different shell treatments

We performed indentation assays on untreated embryos and embryos exposed to three different conditions (2 min bleach without/with subsequent chitinase treatment, and 5 min bleach, respectively). The chemical treatments affect the structure and mechanical properties of the eggshell membrane, as is schematically indicated in Fig. 4.5.

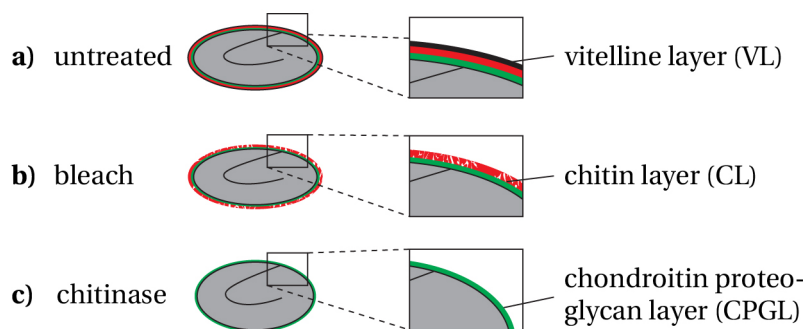


Figure 4.5 – Structural changes of the eggshell upon chemical treatments. The schematic cross-sectional views show the eggshell in its untreated and degraded forms. **a)** The untreated eggshell has a trilaminar structure, consisting of an outer vitelline layer, a middle chitin layer and an inner chondroitin proteoglycan layer. **b)** Treatment with sodium hypochlorite solution (bleach) selectively removes the VL, but may also attack the underlying CL. **c)** Chitinase treatment is applied after bleach treatment to strip away the CL from the embryo shell. The embryo loses its ellipsoidal shape and approaches a circular shape.

The untreated eggshell comprises the full trilaminar structure, consisting of the VL, CL and CPGL. According to the literature, treatment with bleach solution selectively removes the VL [165]. However, our results show that this treatment also attacks and degrades the CL even after a short incubation time (see Discussion 4.5). Chitinase treatment is applied after a bleach treatment to strip the CL away from the embryo. Furthermore, measurements were carried out using eggs at different embryonic development stages, *i.e.* in the gastrulation, bean, and twitching stages, respectively. The gastrulation stage corresponds to the first stage of freshly laid embryos (2.5 h to 6 h after fertilization), followed by the bean stage (6 h to 9 h after fertilization), and the twitching stage prior to hatching, during which the embryo starts moving (9 h to 13 h after fertilization) [187].

In a first approach, we experimentally quantified the deformation of the spheroid-shaped embryos during indentation by analysis of microscopy bright field images for all conditions. For increasing indentation depth Δz , eggs elongate by Δl and widen by Δw with respect to the initial unloaded shape as is schematically illustrated in Fig. 4.6a (length l and width w , typically $50\ \mu\text{m}$ and $35\ \mu\text{m}$, respectively). Fig. 4.6b shows representative high-resolution bright field images of bleach-treated embryo in the gastrulation, bean and twitching stages, in the relaxed and in a poked states with increased egg widths. The embryos, which can be observed through the transparent eggshell, exhibit normal motility after treatment and during indentation. Values for Δl and Δw were determined at a preset indentation force value $F_z = 5.0\ \mu\text{N}$ for untreated and bleach-treated samples.

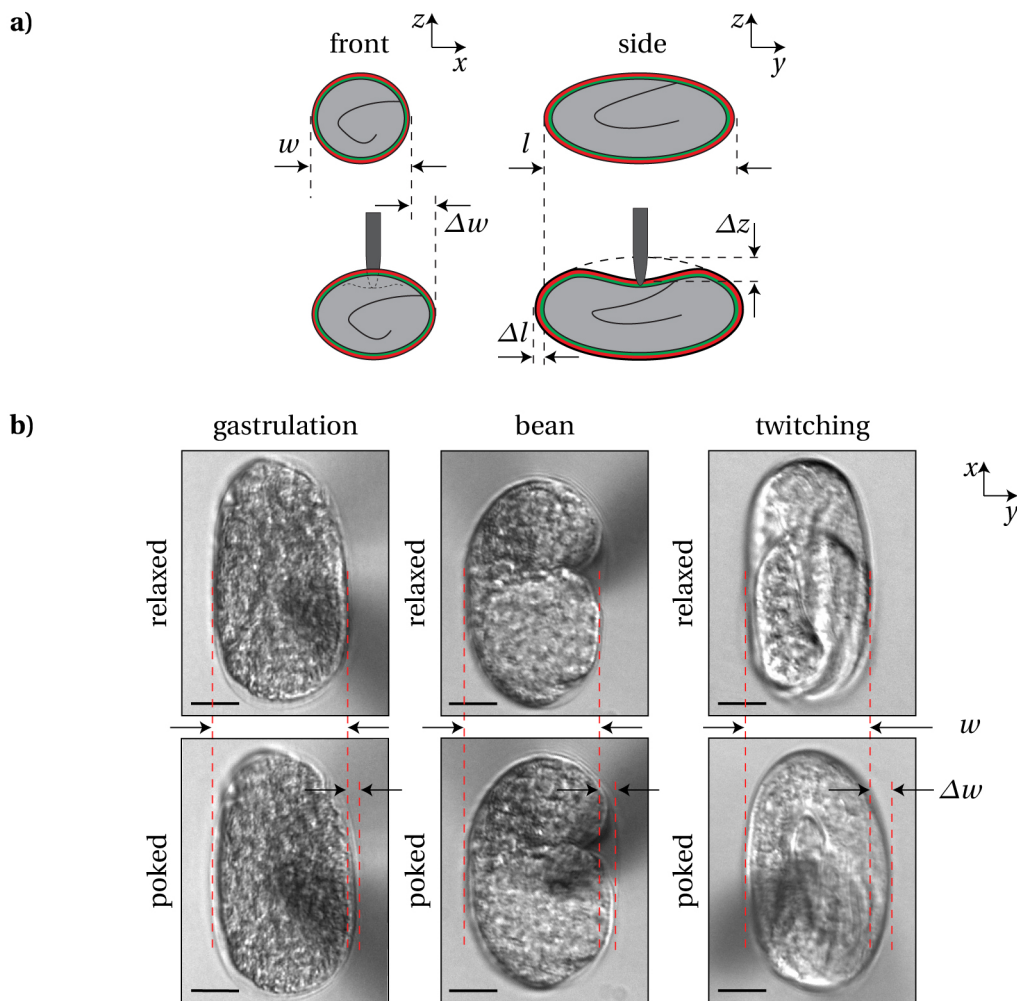


Figure 4.6 – Morphological changes of the eggshell upon chemical treatment and indentation. **a)** Frontal and lateral schematic cross-sections of an embryo, illustrating the shape changes in width Δw and length Δl upon indentation with a depth Δz . **b)** Bright field microscopy images in relaxed and poked states of a live, bleach-treated embryo in the gastrulation, bean and twitching stages. A lateral extension Δw upon indentation with respect to the relaxed egg width w is well visible ($F_z = 5\ \mu\text{N}$). Scale bar = $10\ \mu\text{m}$.

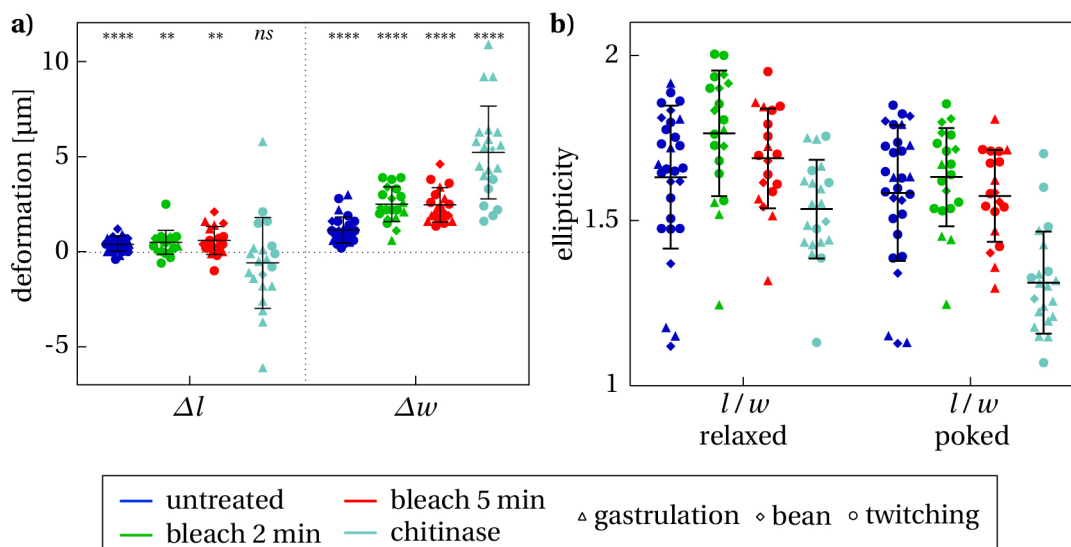


Figure 4.7 – Morphological changes as derived from microscopy images upon indentation. **a)** Scatter plot of embryo elongation Δl and widening Δw for treated and untreated conditions. Widening is more prominent than the elongation changes for all eggs and conditions. Chitinase-treated eggs show larger deviation from mean values than untreated and bleached eggs. Paired t-test was applied to calculate p between l & $l + \Delta l$ and w & $w + \Delta w$, respectively (**: $p \leq 0.01$; ****: $p \leq 0.0001$; ns : not significant). **b)** Scatter plot of the embryo ellipticity (ratio l/w) in relaxed and poked states for treated and untreated conditions. Very soft chitinase-treated eggs tend to assume a more spherical shape compared to untreated and bleached shells. Force values are $F_z = 5 \mu\text{N}$ for untreated and bleached eggs and $F_z = 0.5 \mu\text{N}$ for chitinase-treated eggs in a) and b).

Scatter plots for morphological results in all conditions are presented in Fig. 4.7. The embryo deformation is shown in Fig. 4.7a. A small elongation $\Delta l = (0.3 \pm 0.4) \mu\text{m}$ along the major axis of the spheroid was found for untreated eggs, which was only slightly higher for bleach-treated eggshells. As expected, widening Δw of the prolate spheroid was more pronounced upon indentation, *i.e.* $\Delta w = (1.1 \pm 0.7) \mu\text{m}$ for untreated samples and about twice that value for bleached embryos. The duration of bleach treatment did not affect this parameter. Nevertheless, elongation and widening of the embryos was always small compared to the indentation depth ($\Delta_z \approx 10 \mu\text{m}$ to $15 \mu\text{m}$). Chitinase-treated shells are significantly less resistant to mechanical stress and eggshell puncture occurred already at $F_z \leq 1 \mu\text{N}$, thus Δl and Δw values for these samples had to be evaluated at a one order of magnitude lower force value ($F_z = 0.5 \mu\text{N}$). No measurable deformation was observed for untreated or bleach-treated eggs in this case. Furthermore, we calculated the ellipticity of the individual samples (ratio l/w) in relaxed and poked conditions. The results are displayed in Fig. 4.7b for all conditions. Mean l/w values remain in the range between 1.6 and 1.8 for untreated and bleached conditions. Interestingly, chitinase-treated eggs tend to shorten, *i.e.* to adopt a more spherical shape ($\Delta l = (-0.6 \pm 2.4) \mu\text{m}$), even if the variation of the measured values is large. Conversely, the widening Δw of chitinase-treated eggs was stronger than for untreated samples ($\Delta w = (5.2 \pm 2.4) \mu\text{m}$). In the relaxed condition, chitinase-treated eggs are more circular than untreated or bleached eggs ($l/w = 1.5$), and in the poked condition, eggs become even rounder ($l/w = 1.3$). Fig. 4.7 also

provide information about the measurements performed at different embryonic development stages, however, calculated mean values did not show a significant dependence on embryonic stages. Detailed values are summarized in Tab. 4.2 at the end of the Results section.

4.4.2 Experimental indentation curve analysis

Fig. 4.8a shows a set of representative force-indentation curves $F_z(\Delta_z)$ for untreated, as well as for bleach- and chitinase-treated embryos, respectively.

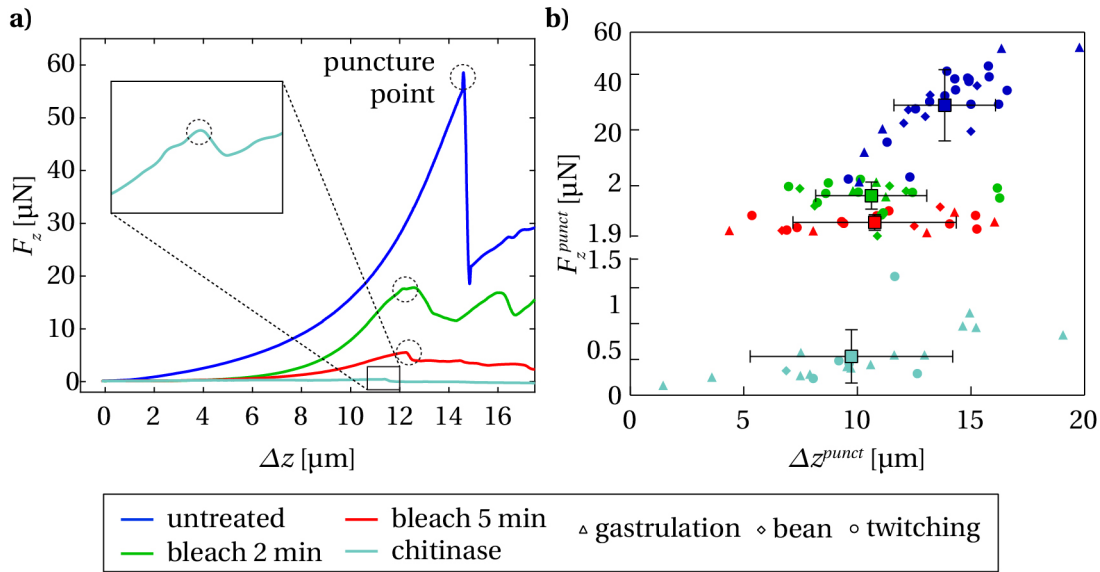


Figure 4.8 – Force-displacement measurements of *C. elegans* embryos. **a)** Representative micro-indentation loading curves (after baseline correction), *i.e.* measured force response F_z of the eggshell *vs.* sensor tip indentation depth Δ_z , for untreated and treated eggs, including displacements beyond eggshell rupture. F_z increases in a nonlinear way with respect to Δ_z , indicating increasing an effective stiffness of the eggshell up to the puncture point. Force response to loading is strongest for untreated eggs (dark blue) and becomes very weak for bleach+chitinase treated eggshells (light blue), where complete removal of the vitelline layer and the chitin layer is expected. Shell puncture events are marked as dotted circles in the plots. **b)** The critical force value F_z^{punct} where eggshell puncture occurs is plotted *vs.* the corresponding indentation depth Δ_z^{punct} , for different treatments and for all embryonic stages (gastrulation, bean and twitching stage). F_z^{punct} decreases drastically with the severity of the treatment. Very low values in the range of $0.5 \mu\text{N}$ are found after bleach+chitinase treatment, where only the innermost chondroitin proteoglycan layer of the eggshell remains. Untreated eggs can sustain the highest indentation depth Δ_z^{punct} , whereas the limit of eggshell deformation is lower but comparable after different treatments.

The graph illustrates that the mechanical resistance of an embryo with respect to puncture strongly weakens for increasingly shell-degrading treatments. Shell puncture events, corresponding to an abrupt drop in the $F_z(\Delta_z)$ curves, are marked as black dotted circles. The shell puncture force F_z^{punct} was defined as the maximum force F_z that the shell could sustain before rupture. After the sharp drop of F_z at the shell puncture point, the curves proceed at non-zero force levels, most likely due to residual friction forces of the shell and the embryo body on the

indenter tip. Notably, the slope of the $F_z(\Delta_z)$ curves for chitinase-treated eggs is much smaller compared to the other treated and untreated eggs, indicating that the shell itself is generating only a very weak resistance to the indenter in this case and that most of the chitin which provides the mechanical stability has been dissolved. Fig. 4.8b summarizes experimental F_z^{punct} values and the corresponding tip indentation depth Δ_z^{punct} , *i.e.* the maximal depth by which the sensor tip may deform the eggshell before irreversible rupture occurred. Data points for the different treatments and embryonic stages are shown. The scatter plot indicates that F_z^{punct} mean values clearly diminished with increasing eggshell degradation, *i.e.* by a factor of ≈ 2.9 after bleach treatment for 2 min and by a factor of ≈ 7.2 after bleach treatment for 5 min with respect to untreated shells ($F_z^{punct} = (49 \pm 13) \mu\text{N}$). Chitinase treatment after 2 min bleach resulted in a substantial decay of the puncture force, *i.e.* by a factor of ≈ 98 , compared to untreated embryos. The critical tip indentation depth Δ_z^{punct} was $(14 \pm 3) \mu\text{m}$ for untreated eggs and somewhat less after bleach treatment ($(11 \pm 4) \mu\text{m}$ and $(10 \pm 4) \mu\text{m}$ after treatment for 2 min or 5 min, respectively). Chitinase exposure did only slightly affect this parameter with respect to bleach treatment ($\Delta_z^{punct} = (10 \pm 4) \mu\text{m}$). To deduce potential mechanical changes of the eggshell in different embryonic stages, mean values were calculated for each stage. We did not, however, observe a clear variation of the shell puncture resistance with respect to the larval development stage. Detailed results for these parameters are presented in Tab. 4.2 at the end of the results section.

$F_z(\Delta_z)$ curves for all conditions showed a nonlinear force response, indicating a general trend of increasing effective eggshell stiffness $k(\Delta_z)$ for stronger indentation. $k(\Delta_z)$, corresponds to the slope of $F_z(\Delta_z)$ at a point Δ_z . In Fig. 4.9a, the extraction of the parameter $k(F_z^{punct})$ using a linear fit near the F_z^{punct} value of the indentation curves is illustrated. For stronger eggshell treatments, the $F_z(\Delta_z)$ curves become flatter, *i.e.* $k(\Delta_z)$, as well as the effective stiffness at the shell puncture point $k(F_z^{punct})$, decreased. $k(F_z^{punct})$ values were extracted from the experimental data for all conditions and larval stages and plotted in Fig. 4.9b. $k(F_z^{punct})$ values drop significantly with respect to untreated embryos, specifically by a factor of ≈ 2.9 for 2 min bleach-treated embryos, by a factor of ≈ 8.7 for 5 min bleach-treated embryos, and by a factor of ≈ 192 for bleach + chitinase-treated embryos, compared to untreated embryos. Detailed numerical values are indicated in Tab. 4.2 at the end of the results section. As $k(\Delta_z)$, corresponding to the slope of $F_z(\Delta_z)$ at a point Δ_z , is a parameter that is directly extracted from the experimental curve, its value is determined not only by the egg sample properties, but also by the entire indenter system.

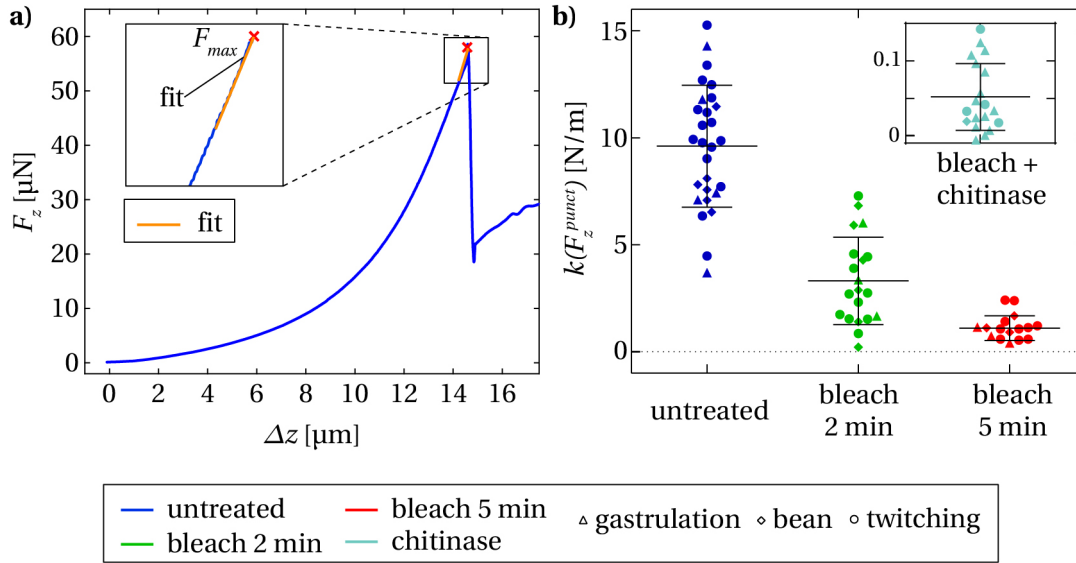


Figure 4.9 – Effective stiffness of *C. elegans* embryos. **a)** $k(F_z^{punct})$ values represent the slope of the $F_z(\Delta_z)$ curve near F_z^{punct} and were extracted using a linear fit (orange line) of the experimental data (blue curve) just before eggshell puncture. **b)** Scatter plot of extracted $k(F_z^{punct})$ mean \pm SD values separated by embryonic stages for all treatments. Mean values significantly decrease after treatment, reflecting decreasing rigidity of the eggshell. $k(F_z^{punct})$ is approaching extremely low values after chitinase treatment, where only the inner layer of the eggshell remains.

4.4.3 Viscoelastic behavior

For the calculation of the moduli in the subsequent sections (4.4.4, 4.4.5), the force response of the embryo was considered as purely elastic. But the embryo is a complex sample showing viscoelastic behavior, which can be seen from experimental $F_z(\Delta_z)$ curves recorded in the range $F_z^{thresh} < F_z^{punct}$, where F_z^{thresh} is too small to burst the shell of the egg. When F_z acting on the sample was recorded during full indentation and retraction cycles, indentation curves do not overlap retraction curves. These curves show a hysteresis loop, the area of which corresponds to the energy dissipated by internal friction and viscous damping. In the analysis, we did not take into account adhesion interactions between the micro-indenter tip and the shell membrane. The viscoelastic energy loss E_{visco} can be quantitatively characterized by calculating the hysteresis area in the $F_z(\Delta_z)$ curves. In addition to the experimental $F_z(\Delta_z)$ curves shown previously, multiple full indentation and retraction cycles with increasing threshold force F_z^{thresh} were recorded for each embryo.

In Fig. 4.10a, a typical indentation measurement of an untreated embryo, is shown. E_{visco} corresponds to the area in between the indentation and retraction portions of the measurements. Normalized E_{visco} values are plotted in Fig. 4.10b, separated by treatment and embryo stage. Here, E_{visco} has been divided by the maximal force F_z^{max} of an $F_z(\Delta_z)$ curve after baseline correction, to account for different indentation force ranges (F_z^{thresh} from 5 μ N to 20 μ N) and F_z^{max} variations arising from viscous friction effects (section 4.3.3). The presented

mean values do not show significant differences in the treatments or the embryonic stage, except for the 5 min bleach-treated embryos in the gastrulation change, which show a higher E_{visco} than the corresponding bean and twitching stages. This may be due to the fact that long bleach treatments degrade the shell sufficiently so that the indenter may feel changes of the embryo inside. Actually, a transformation from an accumulation of cells in the gastrulation stage into a moving organism in the twitching stage takes place in this phase of embryo growth. According to our observation, a cell cluster exhibits higher viscoelasticity than a L1 worm before hatching.

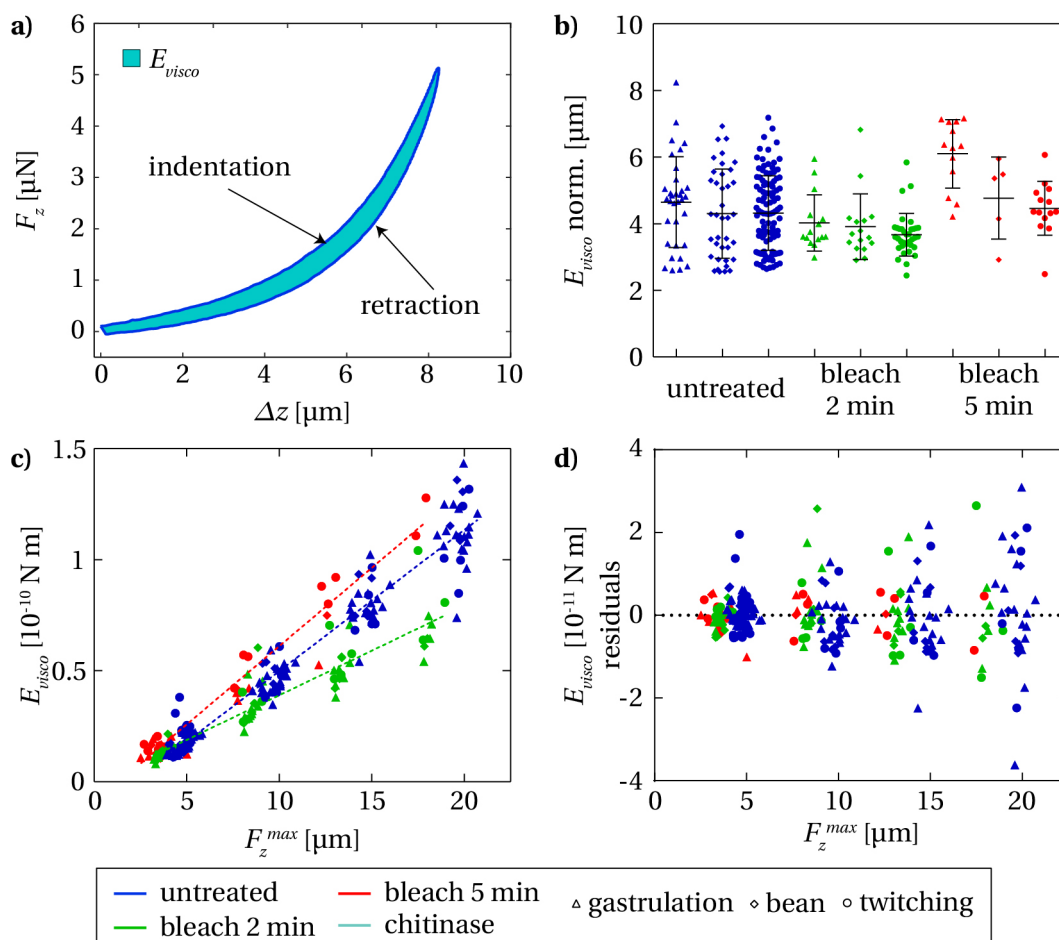


Figure 4.10 – Hysteresis area of the force indentation loading cycles. **a)** Example of a complete indentation loading cycle of an untreated embryo up to a threshold force $F_z^{thresh} = 5 \mu\text{N}$. **b)** Grouped scatter plot of the calculated hysteresis area E_{visco} values normalized by the corrected F_z^{thresh} and separated by gastrulation, bean and twitching stages. Mean values do not vary significantly between treatments and stages, except for 5 min bleach-treated embryos in the gastrulation stage, where a larger hysteresis loop is observed. **c)** Hysteresis area as a function of the corrected F_z^{thresh} fitted by linear regression of the untreated and bleached treatment conditions. Interestingly, the untreated and 5 min bleach-treated conditions show higher hysteresis than the 2 min bleach-treated condition. **d)** Residuals of the linear fit ($n_{untreated} = 175$, $n_{bleached2min} = 66$, $n_{bleached5min} = 32$).

Furthermore, E_{visco} is plotted *vs.* F_z^{thresh} in Fig. 4.10c. E_{visco} follows a linear trend with respect to F_z^{thresh} , indicated by linear regression superimposed on the scattered values. The slopes hereby quantify the viscoelastic energy loss per applied force, allowing a comparison of E_{visco} between the different treatment conditions. Interestingly, untreated and 5 min bleach-treated embryos have significantly higher E_{visco} compared to 2 min bleach-treated samples. In Fig. 4.10d, the residuals of the linear regression of E_{visco} are shown. The small values of the randomly dispersed data points indicate a good fit of the linear regression model for the extraction of the slopes.

	slope [N]	R^{22}	n
untreated	$(6.35 \pm 0.11) \times 10^{-6}$	0.95	175
bleach 2min	$(4.01 \pm 0.21) \times 10^{-6}$	0.86	66
bleach 5min	$(7.05 \pm 0.29) \times 10^{-6}$	0.95	32

Table 4.1 – Linear regression of E_{visco} as a function of F_z^{max} . Summary of values obtained by linear regression of $E_{visco}(F_z^{max})$ sets for different shell treatments corresponding to Fig. 4.10c.

4.4.4 Model for FEM simulations of embryo indentation

To extract the mechanical properties of the embryo eggshell itself from experimental $F_z(\Delta_z)$ measurements, parameters such as shape and thickness of the shell, as well as the micro-indenter tip size and shape, must be considered. The complexity of the problem makes analytical calculations difficult. Hence, we applied a FEM simulation to model *C. elegans* egg indentation and to calculate $F_z(\Delta_z)$ loading curves numerically. For this purpose, we model the elastic force component related to membrane deformation and the force generated by the internal egg pressure build-up pint upon indentation. Comparing simulated and experimental data allowed the Young's moduli E_{shell} of the eggshells to be determined for different conditions.

Our simulations are based on an isotropic linear elastic material model, which is in general a good assumption for small material deformations. This approach requires only two independent eggshell material parameters, *i.e.* E_{shell} and the Poisson's ratio ν_{shell} , to relate stress $\sigma_{i,j}$ and $\epsilon_{i,j}$ components in 3 dimensions ($i, j = x, y, z$) according to the equations:

$$\begin{bmatrix} \epsilon_{xx} \\ \epsilon_{yy} \\ \epsilon_{zz} \\ 2\epsilon_{yz} \\ 2\epsilon_{xz} \\ 2\epsilon_{xy} \end{bmatrix} = \frac{1}{E_{shell}} \begin{bmatrix} 1 & -\nu_{shell} & -\nu_{shell} & 0 & 0 & 0 \\ -\nu_{shell} & 1 & -\nu_{shell} & 0 & 0 & 0 \\ -\nu_{shell} & -\nu_{shell} & 1 & 0 & 0 & 0 \\ 0 & 0 & 0 & 2(1+\nu_{shell}) & 0 & 0 \\ 0 & 0 & 0 & 0 & 2(1+\nu_{shell}) & 0 \\ 0 & 0 & 0 & 0 & 0 & 2(1+\nu_{shell}) \end{bmatrix} \begin{bmatrix} \sigma_{xx} \\ \sigma_{yy} \\ \sigma_{zz} \\ \sigma_{yz} \\ \sigma_{xz} \\ \sigma_{xy} \end{bmatrix} \quad (4.4)$$

We assume a value of $\nu_{shell} = 0.3$, which is a generally accepted compromise for biomaterials with largely undefined material properties, but which can be considered as neither fully compressible ($\nu_{shell} = 0$) nor perfectly incompressible ($\nu_{shell} = 0.5$). The eggshell geometry

was approximated as a prolate spheroid, which coincides well with the actual *C. elegans* egg shape. The shell thickness was taken as $t = 300$ nm, based on transmission electron microscopy (TEM) images from Olsen *et al.* (2012), using uniform material parameters. The egg is considered to be filled with an incompressible fluid, *i.e.* the internal egg volume is considered constant during indentation. A spherical tungsten indenter with tip radius $r_{ind} = 1$ μm presses against the embryo from the top, which lies on a glass baseplate. Standard material parameters of tungsten and glass were used for the rigid components of the model setup. A representative example of the numerical model applied to the embryo is shown in Fig. 4.11. The computed stress that builds up in the deformed shell is displayed by a color scheme, assuming an indentation depth $\Delta_z = 15$ μm (*i.e.* the largest value considered for the simulations), a representative shell modulus $E_{shell} = 0.12$ GPa and $p_{int} = 1.6 \times 10^5$ Pa. The highest stress arises directly under the indenter tip, corresponding to the shell rupture point for $F_z > F_z^{punct}$. Stress in the membrane is negligible at locations more than a few micrometers away from the indentation point.

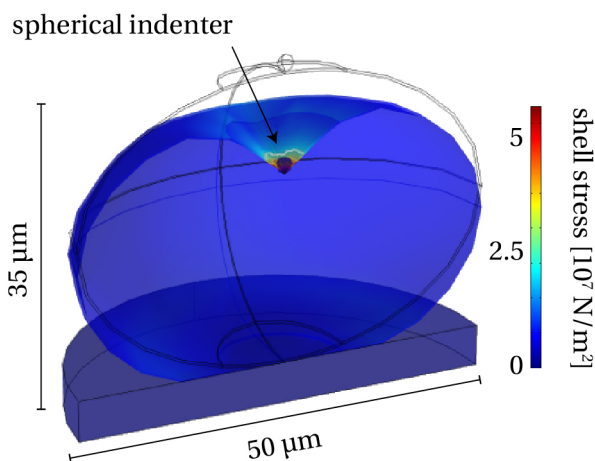


Figure 4.11 – FEM model of *C. elegans* embryo indentation experiments. A spheroidal, fluid-filled elastic shell is used as model for indentation simulations and data fitting. Eggshell deformation and resulting membrane stress upon indentation by a spherical indenter are shown for $\Delta_z = 15$ μm (tip radius $r_{ind} = 1$ μm , shell thickness $t = 300$ nm, shell modulus $E_{shell} = 0.12$ GPa, $p_{int} = 1.6 \times 10^5$ Pa). The initial embryo shape in the relaxed state is indicated by grey lines (egg length $l = 50$ μm , width $w = 35$ μm).

From the simulation, we extracted simulated values for embryo elongation and widening Δ_l^{sim} and Δ_w^{sim} , dependent on the indentation depth Δ_z . The data is shown in Fig. 4.12a. The model predicts a nonlinear increase of the deformation values with respect to the indentation depth, with Δ_w^{sim} values significantly higher than Δ_l^{sim} . For the comparison with experimentally obtained values by microscopy during indentation, mean Δ_z values of experimental $F_z(\Delta_z)$ curves at $F_z = 5$ μN were extracted ($\Delta_z = (13 \pm 10)$ μm). These values were used to extract $\Delta_l^{sim} = 0.17$ μm and $\Delta_w^{sim} = 2.76$ μm after linear interpolation of the simulated deformation points. When comparing to corresponding actual mean values of untreated embryos $\Delta_l = (0.4 \pm 0.4)$ μm and $\Delta_w = (1.1 \pm 0.7)$ μm at $F_z = 5$ μN , we recognize that the model underestimates Δ_l by a factor of ≈ 2 , and overestimates Δ_w by a factor of ≈ 2.5 . Geometrical

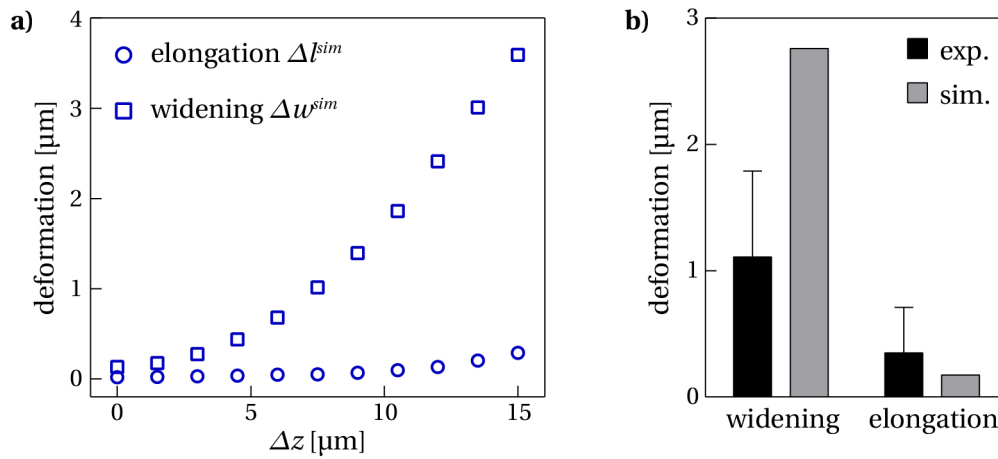


Figure 4.12 – FEM simulation of the embryo deformation. **a)** Simulated deformation Δl^{sim} and Δw^{sim} of the eggshell upon indentation as a function of the indentation depth Δz . Both Δl^{sim} and Δw^{sim} show a nonlinear dependence on Δz , with Δw^{sim} significantly higher than Δl^{sim} . **b)** Comparison of experimentally obtained Δl and Δw vs. simulated Δl^{sim} and Δw^{sim} .

constraints in the simulation could influence the obtained simulated results, but the discrepancy is assumed to predominately originate from viscoelastic effects of the embryo in the egg, which for the purpose of these simulations was assumed to be filled with water. Fig. 4.12b shows a bar graph of the comparison of experimentally obtained Δl and Δw vs. simulated Δl^{sim} and Δw^{sim} .

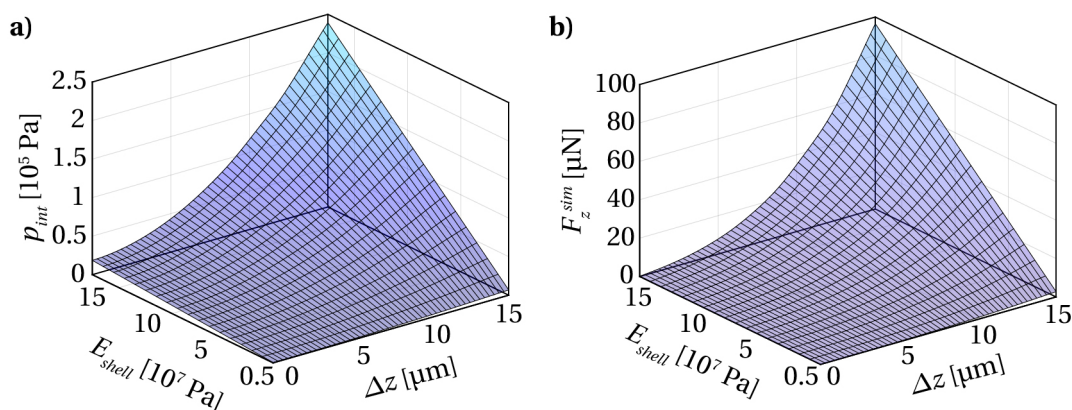


Figure 4.13 – FEM simulation of the internal pressure and force on the indenter. **a)** 3D representation of the simulated p_{int} - Δz - E_{shell} parameter space. p_{int} , the internal egg pressure that builds up as a function of the indentation depth Δz , is an important parameter required for accurate fitting of the experimental $F_z(\Delta z)$ curves. **b)** Simulated and interpolated F_z^{sim} - Δz - E_{shell} parameter space. The total force F_z^{sim} exerted on the micro-indenter by the eggshell comprises an elastic membrane component and the force related to the internal egg pressure p_{int} .

4.4.5 Determination of the eggshell Young's moduli

In order to extract the Young's modulus E_{shell} of the *C. elegans* embryonic eggshell for a specific condition from the experimental indentation curves, first the internal egg pressure p_{int} that builds up as a function of the indentation depth Δz was derived by means of our model. p_{int} not only deforms the spheroidal egg along the minor and major axes but is also an important parameter for accurate fitting of the experimental $F_z(\Delta z)$ curves, as both, pressure and elastic membrane forces, contribute to the measured indentation force. The total simulated force F_z^{sim} exerted on the micro-indenter by the eggshell was then calculated by integrating the membrane stress components in z direction, under consideration of the internal pressure force. A parametric sweep for E_{shell} values from 5×10^6 Pa to 1.8×10^8 Pa (incremented by $\Delta E_{shell} = 1 \times 10^7$ Pa) was used in the simulations to cover the relevant p_{int} - Δz - E_{shell} and F_z^{sim} - Δz - E_{shell} spaces. The interior pressure surface $p_{int}(\Delta z, E_{shell})$, shown in Fig. 4.13a, as well as the simulated indentation force surface $F_z^{sim}(\Delta z, E_{shell})$, plotted in Fig. 4.13b, were obtained by interpolation using a cubic spline algorithm.

The quality of our model can be evaluated by means of Fig. 4.14a, where a direct comparison of a representative experimental indentation loading curve for an untreated embryo, and the corresponding best-fitting computed $F_z^{sim}(\Delta z, E_{shell})$ curve (with $E_{shell} = 0.12$ GPa) is plotted.

The model reproduces well the nonlinear force response to indentation, and excellent congruence of the two curves over the full Δz range up to the puncture point at $\Delta z \approx 13 \mu\text{m}$ can be observed. In order to determine the E_{shell} value corresponding to a particular experimental

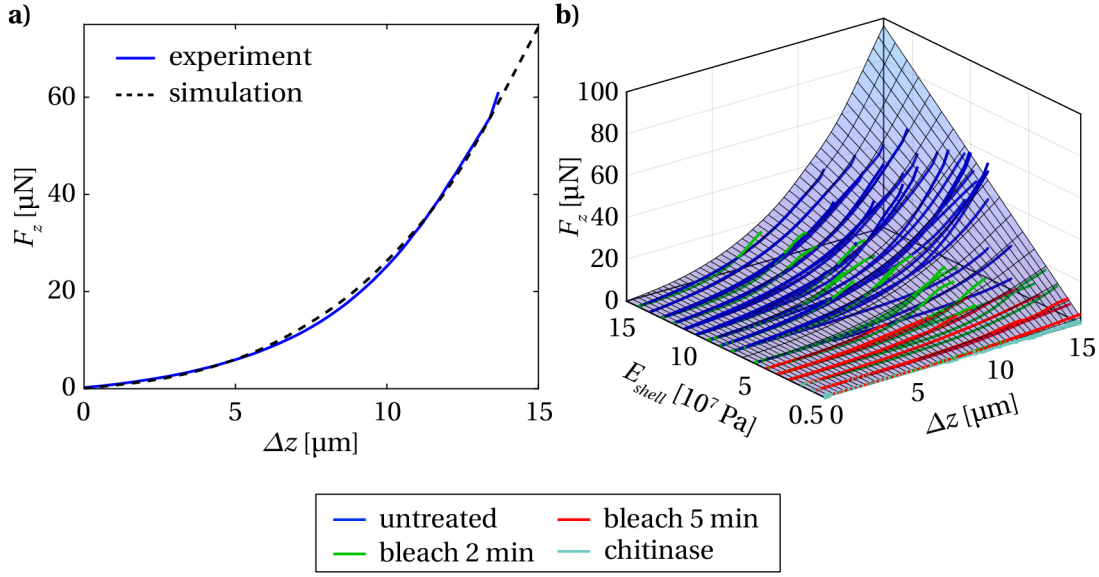


Figure 4.14 – Evaluation of specific mechanical properties of *C. elegans* embryos. **a)** Representative force-indentation measurement $F_z(\Delta_z)$ of an untreated embryo and the best-fitting simulated $F_z^{sim}(\Delta_z, E_{shell})$ curve. Good agreement of both curves is achieved by using a value of $E_{shell} = 0.12$ GPa for the eggshell modulus. **b)** The full set of experimental $F_z(\Delta_z)$ loading curves (solid lines) for all treatments and embryo development stages is superposed to the simulated $F_z^{sim}-\Delta_z-E_{shell}$ parameter space. $F_z(\Delta_z)$ curves, displayed up to the puncture point, are arranged with respect to the corresponding E_{shell} value derived from the best-fitting simulated curve.

$F_z(\Delta_z)$ curve, the best-fitting simulated curve from the $F_z^{sim}(\Delta_z, E_{shell})$ set was identified by minimizing the sum of squares of the force value difference of a simulated trace and the experimental data, considering the full set of simulated F_z^{sim} curves, using the equation:

$$S = \sum (F_z^{sim} - F_z)^2, \quad (4.5)$$

where S is the sum of squares. This protocol was performed for all recorded indentation curves. The results are displayed in Fig. 4.14b, where the entire set of experimental curves for all conditions and embryo stages is superposed to the simulated and interpolated indentation force surface $F_z^{sim}(\Delta_z, E_{shell})$. Here, the $F_z(\Delta_z)$ curves are arranged according to the corresponding extracted E_{shell} values based on our model assumptions (incremented by $\Delta E_{shell} = 1 \times 10^7$ Pa).

The scatter plot in Fig. 4.15a groups all extracted E_{shell} values for the different eggshell treatments. Deterioration of the shell mechanical properties, *i.e.* decreasing mean E_{shell} values, depending on type and duration of the treatment, can be clearly observed. For untreated samples, a value $E_{shell} = (0.12 \pm 0.03)$ GPa was found, which decreased considerably, *i.e.* by a factor of ≈ 1.3 , ≈ 2.4 and ≈ 17.2 for 2 min, 5 min bleach and chitinase-treated samples, respectively. Furthermore, we analyzed the maximal internal pressure p_{int}^{max} characterizing the pressure value just before shell rupture, which could be extracted from the $p_{int}-\Delta_z-E_{shell}$ space

(Fig. 4.13a) by means of the corresponding maximum indentation depth Δ_z^{punct} (Fig. 4.8b) and E_{shell} values of each embryo. Since treated shells have lower mean E_{shell} and Δ_z^{punct} values, resulting p_{int}^{max} values are lower in treated cases. These results are plotted in Fig. 4.15b for the four eggshell treatment conditions. For untreated embryos a value $p_{int}^{max} = 1.2 \times 10^5$ Pa was found, whereas p_{int}^{max} decreased by a factor of ≈ 2.4 , ≈ 5.2 and ≈ 32 for 2 min or 5 min bleach-treated, and chitinase-treated samples, respectively. Mean values for E_{shell} and p_{int}^{max} parameters have also been determined for the different embryo developmental stages, but no significant stage dependence was found. Details are summarized in Tab. 4.2 at the end of the results section.

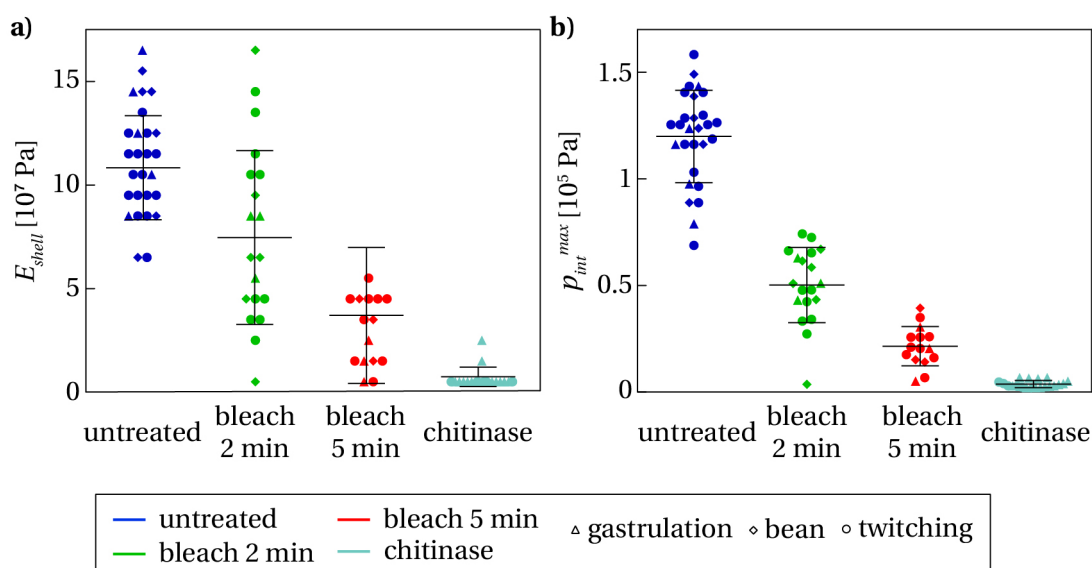


Figure 4.15 – Results of the evaluation of the mechanical properties of *C. elegans* embryos. **a)** E_{shell} values extracted from the experimental data by applying the described model for all embryonic stages, separated with respect to the corresponding eggshell treatment. The mean value of the Young's modulus of the shell decreases significantly after bleaching and becomes extremely low after additional chitinase exposure. **d)** Maximum values p_{int}^{max} of the internal egg pressure just before shell rupture for all treatments and embryonic stages.

Chapter 4. Force microscopy of *Caenorhabditis elegans* embryos

Lastly, we examined the dependence of the shell elastic modulus E_{shell} on the shell thickness t . For this study, F_z^{sim} parameter spaces were simulated using several shell thicknesses ranging from 250 nm to 750 nm. Data fitting to obtain E_{shell} from experimental $F_z(\Delta_z)$ curves for untreated embryos was done as described before. Fig. 4.16 shows the resulting E_{shell} values as a function of shell thickness t . The data shows a non-linear thickness dependent decay of E_{shell} according to $E_{shell} = 5.3 \times 10^{-4} \cdot t^{-1.735}$. The data is useful if shells of different thicknesses are investigated.

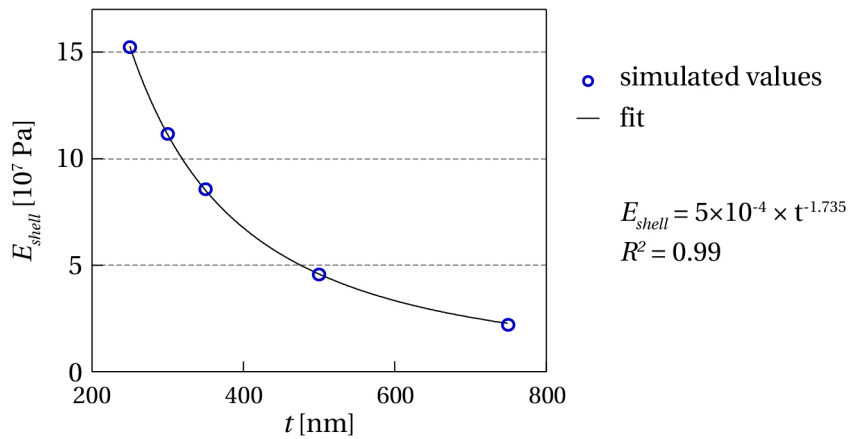


Figure 4.16 – Simulated E_{shell} values as a function of the eggshell thickness t .

4.4.6 Summary of the results

The clustergram in Fig. 4.17 and Tab. 4.2 summarize all experimental results. The following parameters are considered: the shell puncture force F_z^{punct} , the maximal effective stiffness at shell rupture $k(F_z^{punct})$ and indentation depth at shell puncture Δ_z^{punct} (see section 4.4.2), embryo elongation Δ_l and embryo widening Δ_w upon indentation with a given force F_z (see section 4.4.1), and the shell elastic modulus E_{shell} and the maximal interior pressure at shell rupture p_{int}^{max} (see section 4.4.5). For the clustergram representation (Fig. 4.17), the parameters of interest (P_{IN}) were normalized with respect to the control parameters (P_{CNT}) corresponding to those of the untreated embryo according to:

$$P_{OI} = \frac{P_{IN}}{P_{CNT}} - 1, \quad (4.6)$$

where P_{OI} is the normalized parameter of interest plotted in the clustergram.

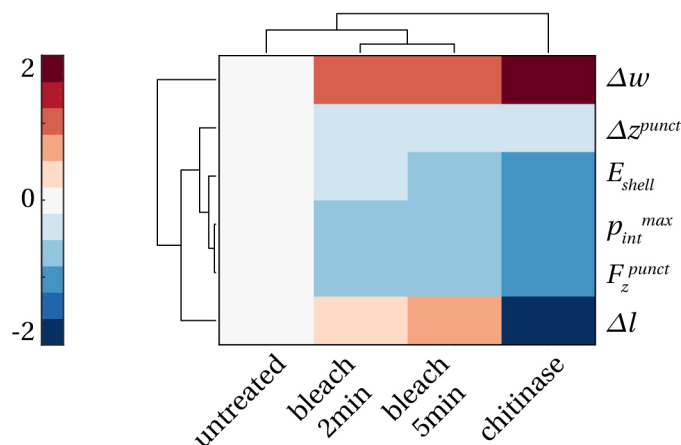


Figure 4.17 – Clustergram representation of force-indentation results.

The plot was made in MATLABs Bioinformatics Toolbox using the clustergram function. This way of plotting the data clearly visualizes the difference of the treated embryos with respect to the controls and how the specific phenotypes can be used to identify the impact of the treatment. For example, for all treated conditions there was a significant widening Δ_w compared to untreated conditions, hence this value can be used most reliably to determine whether a weakening treatment was applied to a shell with unknown mechanical parameters. Interestingly, elongation Δ_l can be used to distinguish between bleach-treated and chitinase treated eggshells. Embryos with different bleach durations are related closest to each other but can be easily separated from untreated embryos. Chitinase treatment results in the most drastic changes of measured parameters. A parameter remaining constant for all treatment conditions is Δ_z^{punct} , meaning that it is unsuitable to separate different treatment conditions. Tab. 4.2 summarizes the numerical mean values \pm SD for all mechanical parameters, separated by larval development stages and average values for all stages.

Untreated	All stages		Gastrulation		Bean		Twitching	
	Mean	SD	Mean	SD	Mean	SD	Mean	SD
F_z^{punct}	48.9	12.8	46.5	22.0	47.0	6.2	50.2	12.2
Δ_z^{punct}	13.9	2.3	13.5	4.4	13.5	1.4	14.1	1.8
Δ_l	0.35	0.36	0.33	0.42	0.52	0.46	0.3	0.3
Δ_w	1.11	0.68	1.38	1.0	0.87	0.43	1.10	0.63
E_{shell}^{max}	1.12×10^8	2.6×10^7	1.25×10^8	3.16×10^7	1.20×10^8	3.67×10^7	1.04×10^8	1.81×10^7
p_{int}^{max}	1.2×10^5	2.16×10^4	1.12×10^5	2.47×10^4	1.24×10^5	2.08×10^4	1.21×10^5	2.18×10^4
Bleached 2 min	All stages		Gastrulation		Bean		Twitching	
	Mean	SD	Mean	SD	Mean	SD	Mean	SD
F_z^{punct}	16.9	5.3	18.5	2.6	16.5	8.6	16.7	4.1
Δ_z^{punct}	11.3	3.9	10.6	0.8	12.7	6.8	10.9	2.9
Δ_l	0.46	0.63	0.55	0.21	0.40	0.37	0.45	0.83
Δ_w	2.47	0.82	1.45	0.85	2.26	0.90	2.81	0.84
E_{shell}^{max}	8.65×10^7	6.15×10^7	7.50×10^7	1.73×10^7	7.33×10^7	5.38×10^7	9.68×10^7	7.36×10^7
p_{int}^{max}	5.02×10^4	1.76×10^4	5.24×10^4	9.97×10^3	4.75×10^4	2.30×10^4	5.11×10^4	1.73×10^4
Bleached 5 min	All stages		Gastrulation		Bean		Twitching	
	Mean	SD	Mean	SD	Mean	SD	Mean	SD
F_z^{punct}	6.8	2.8	5.7	3.1	7.3	4.5	7.2	2.4
Δ_z^{punct}	10.8	3.6	11.2	4.3	11.0	2.2	10.5	1.1
Δ_l	0.56	0.74	0.73	0.31	1.33	0.50	0.22	0.16
Δ_w	2.43	0.90	2.23	0.30	2.83	0.88	2.42	0.27
E_{shell}^{max}	4.67×10^7	5.16×10^7	1.50×10^7	1.00×10^7	3.17×10^7	1.53×10^7	5.10×10^7	5.66×10^7
p_{int}^{max}	2.33×10^4	1.17×10^4	1.87×10^4	1.28×10^4	2.29×10^4	1.43×10^4	2.48×10^4	1.24×10^4
Chitinase	All stages		Gastrulation		Bean		Twitching	
	Mean	SD	Mean	SD	Mean	SD	Mean	SD
F_z^{punct}	0.5	0.4	0.6	0.3	0.3	0	0.6	0.6
Δ_z^{punct}	10.2	4.1	10.5	4.8	6.9	0	10.2	1.9
Δ_l	-0.62	2.39	-1.18	2.65	-1.20	0	0.77	1.13
Δ_w	5.19	2.44	6.31	2.07	5.40	0	2.53	0.85
E_{shell}^{max}	6.50×10^6	4.89×10^6	7.14×10^6	5.79×10^6	5.00×10^6	0	5.00×10^6	0
p_{int}^{max}	3.77×10^3	1.72×10^3	4.06×10^3	1.89×10^3	1.80×10^3	0	3.35×10^3	1.00×10^3

 Table 4.2 – Experimental results of all force-indentation measurements (mean values \pm SD, n = number of embryos).

4.5 Discussion

Although there are various studies looking at the biomechanical properties of adult *C. elegans* worms [188, 189, 190], the embryonic stage of this nematode has not been mechanically characterized. Here, we took advantage of the versatility of an integrated CFM-optical microscope setup for measuring the mechanical properties of embryonic eggshells by means of micro-indentation. The system does not require complicated sample preparation protocols and manipulations. Since the sensor tip can operate in a liquid environment, live embryos can be readily probed in a non-invasive manner under physiological conditions by simply locating an egg suspension on a glass slide. We demonstrated that our system enables detecting impairment of the embryo eggshells under various (bio-)chemical conditions. To extract mechanical shell parameters from experimental force-displacement curves $F_z(\Delta_z)$, a FEM model was used, where the egg in its unloaded state is considered as a non-pressurized ellipsoidal capsule, undergoing an increasing internal pressure build-up during indentation. Available analytical solutions for spherical or ellipsoidal shell structures are not easily applicable for our assays, as these solutions address only the non-pressurized or highly pressurized state without taking into account possible variations of the internal pressure as a function of an external parameter, such as the indentation depth Δ_z [191, 192, 193, 194, 195]. Furthermore, the pressure increases during the indentation (since the volume inside the egg stays constant), which affects the measured force and adds another layer of complexity. However, very good agreement of experimental and simulated indentation curves was observed in Fig. 4.14a and revealed that the simple egg model developed in this work was sufficient to reliably extract fundamental biomechanical properties of the *C. elegans* embryo.

Force response of the shell to loading was strongest for untreated eggs and became weak for bleach+chitinase treated eggshells. It is generally assumed that the relatively thick intermediate CL mainly determines the mechanical properties and stability of the eggshell trilayer structure [196, 165]. For example, we found a value of $E_{shell} = 0.12$ GPa for the Young's modulus of the untreated embryonic eggshell. Interestingly, this value falls into the range of the Young's moduli reported for chitin-protein networks measured in the beak of the squid *Dosidicus gigas*, *i.e.* 0.03 GPa to 5 GPa, depending on hydration and protein content [197]. Reported values for pure chitin structures, such as crystalline chitin in dry state ($E = 40$ GPa) [198] or chitin nanofibers (estimated $E = 150$ GPa) [199], however, are up to three orders of magnitude higher than the E_{shell} value in the present case. For the time being, nothing is known about the exact structure and composition of the CL, nevertheless, our results indicate that chitin in the *C. elegans* eggshell is probably present in a mixture with proteins.

Moreover, we applied NaOCl (bleach) for selectively removing the outermost VL, and chitinase, which dissolves the underlying CL, and measured the impact of these treatments on the mechanical integrity of the shell. Since the CL provides the mechanical stability to the egg, bleach treatments should not significantly modify the recorded $F_z(\Delta_z)$ curves, and thereby the mechanical shell parameters, with respect to untreated embryos. On the contrary, our experiments revealed a clear effect of bleach treatment. Even a short treatment drastically

changed the mechanical integrity of the embryonic egg, resulting in lower resistance to puncture or lower Young's moduli E_{shell} compared to untreated embryos. Furthermore, as shown qualitatively in Fig. 4.7 and quantitatively in Fig. 4.8, Fig. 4.9 and Fig. 4.15, the impact increased for longer incubation times (*i.e.* 2 min *vs.* 5 min). Our observations indicate that the CL is partially removed or at least weakened under these conditions, a fact that disagrees with previous claims in literature, assuming that NaOCl only attacks the VL [181, 182, 165]. Subsequent treatment with chitinase is expected to completely remove the CL structural backbone of the eggshell, which can indeed be concluded from our measurements, showing extremely low Young's moduli and puncture forces in this case.

Staining of the CL in *C. elegans* embryos at different developmental stages, using either immunogold-labeled chitin-binding domain probe or wheat germ agglutinin labelling, indicated that the CL undergoes modifications during embryo development, but it is unclear how exactly the CL changes [200, 201]. In our study, we performed extensive measurements at all embryo development stages, nonetheless, we could not determine a significant variation of the mechanical properties for a given treatment. These findings indicate that the biomolecular modifications occurring in the shell during ex-uterus embryogenesis of wild-type *C. elegans* do not affect its mechanical properties. Nevertheless, the capability of the CFM to detect mechanical alterations of the eggshell structure with high sensitivity possibly might be applied in the future to identify genes that are responsible for up- and downregulating layer synthesis in the shell stratum during embryogenesis. Eggshell synthesis begins at fertilization through modifications of the extracellular matrix surrounding the oocyte and proceeds sequentially starting from the outer VL. Interestingly, over 100 genes have been identified by ribonucleic acid (RNA) interference, whose suppression generates phenotypes showing an osmotic integrity defect (OID) [202, 203, 204]. Thus, a depletion of genes playing a crucial role in the formation of the successive eggshell layers eventually may lead to the disruption of the inner permeability barrier. Nevertheless, the specific function of most of these genes is largely unknown. Some exceptions are the *chs-1* gene, which is likely to be the responsible for chitin synthesis in the CL [200], *cbd-1*, encoding a component of the VL, and *cpg-1*, synthesizing chondroitin proteoglycan for the CPGL [203]. Furthermore, Carvalho *et al.* identified 310 more gene candidates using bioinformatics that might play a role in eggshell synthesis with 20 of them showing the OID phenotype [163]. Even, if most of these genes are not related to the OID phenotype, they could still have a notable impact on eggshell synthesis. Tools that enable assessing the significance of such genes based on other phenotypic criteria are therefore of interest, especially the micro-indentation technique presented in this paper that accurately probes the biomechanical integrity of the eggshell.

4.6 Conclusion

In this work, we conducted a quantitative study of the mechanical properties of the *C. elegans* eggshell. The assays were performed by micro-indentation measurements, taking advantage of a custom CFM setup that was integrated with an optical microscope for high-resolution imaging of the embryos during indentation. We performed micro-indentation assays of *C. elegans* embryos in an untreated state and in three modified conditions, *i.e.* exposure to two different bleach treatments with subsequent chitinase exposure. Application of these protocols was expected to selectively remove the outermost vitelline layer and the underlying chitin layer of the eggshell. We concluded from our experiments, however, that the chitin layer is also affected by the bleach treatment. Experimental micro-indentation curves revealed that the eggshell elastic force F_z increased in a nonlinear way as a function of the indentation depth Δ_z for all four conditions. Mechanical parameters, specifically the Young's modulus E_{shell} of the shell, were extracted from experimental data by means of a simple numerical ellipsoid-indentation model. Our results clearly indicate that the mechanical integrity of the eggshell is strongly affected by the applied chemical treatments, especially after removal of the chitin layer by successive bleach/chitinase exposure. With our study, we demonstrate that CFM is an accurate and versatile tool to determine the mechanical properties of natural *C. elegans* eggshells, as well as of chemically modified shells. This approach opens the way for more advanced embryo assays in view of correlating mechanical properties with other phenotypic or genetic parameters.

5 Conclusion and outlook

Despite being an invertebrate organism lacking many organs and a dedicated respiratory system and an appearance very far from human beings, *C. elegans* remains a powerful model organism for metabolic studies and human disease research. A high degree of homology between the genome of the worm and the human being leads to conservation of molecular pathways and thus the possibility of modelling human diseases in worms to unravel their mechanisms of action. Drug discovery on the whole-organism level allows identifying drug candidates and their efficiency in a more comprehensive way than *in vitro* or with cell- and tissue-based studies. Hereby, assessment of complete biological responses with consideration of many different phenotypes at the same time, such as behaviour, food uptake, life span, body heat or respiration rate, strongly increases the information content of an assay and its interpretation with respect to the impact of a potential drug candidate in a higher-order vertebrate organism. *C. elegans* is a simple but still complete organism for *in vivo* testing, allowing results to be obtained fast and in a cost-efficient manner without ethical constraints. The principal objective of this work was the development of new tools for *in vivo* metabolic studies of *C. elegans*. For the implementation of the devices, we took advantage of microfluidics and MEMS sensors. Our approach allowed the manipulation and culture of the organisms on-chip, while simultaneously measuring the metabolic heat production or the respiration rate for the assessment of an animal's metabolic activity.

For direct calorimetry of *C. elegans* (Chapter 2), we developed a system to investigate the heat signatures of larval populations confined in a microfluidic chamber. Hereby, microfabricated thermopile sensors were integrated with PDMS microfluidics using a new fabrication approach. Sealing of the microchannels with a thin PDMS membrane and placing the resulting chip directly on the sensing membrane of the thermopile allowed using regular soft lithography for processing the chips. In this way, heat-producing larval *C. elegans* populations were trapped in the microfluidic device close to the sensing surface, minimizing heat losses to the system. Our microfluidic calorimetry system allows versatile manipulation and treatment of the worm samples directly on-chip without disturbing the thermal stability of the device, a feature that was precluded in calorimeters so far. We used the device to characterize the

heat power of larval *C. elegans* populations in up to 50× smaller numbers than in previous studies using isothermal microcalorimetry. Our results, which are supported by volumetric growth data and mtDNA counts, indicate a phase of mitochondrial proliferation during the L3 stage. In a metabolic assay, where we induced *uncoupled respiration* in the worm populations using the mitochondrial uncoupling agent FCCP, the worms showed increased metabolic heat production (by a factor of 1.5 to 2, depending on larval stage) during maximal respiration. These results are supported by OCR measurements using our own custom-made microfluidic system (see following paragraph), as well as previous OCR measurements using commercial devices involving larger worm populations. To the best of our knowledge, an assay of metabolic heat production of *C. elegans* worms during *uncoupled respiration* has never been performed before.

For indirect calorimetry of *C. elegans* (Chapter 3), a microfluidic platform comprising a luminescence-based oxygen sensor was implemented. Our approach relied on an oxygen-sensitive dye deposited on glass, which we bonded to microchannels fabricated in OSTE+. The polymer is suitable for oxygen concentration measurements on-chip due to its low oxygen permeability and properties close to thermoplastics, as opposed to PDMS, which is highly gas-permeable. We optimized the OSTE+ microfluidic chip fabrication using a custom molding process that eventually allowed producing rigid, biocompatible chips with features in the μm -range, similar in quality as comparable PDMS structures. The oxygen measurement principle is based on the read-out of the oxygen-dependent luminescence of a sensing dye within the channels in a non-invasive way from the outside of the microchip. Using the new fabrication approach integrating the miniaturized oxygen sensor, we fabricated a culture chamber for the confinement of very small worm populations starting from the L4 stage. The small chamber volume even allowed to quantify the OCR of a single worm on-chip. We implemented an automated feeding protocol allowing the supply of nutrients and the measurement of the worm OCR every hour over several days. Compared to other approaches which are limited to short-term experiments, as they rely on periodically obtaining fresh samples from NGM agar plates, our approach allows continuous data acquisition in well-controlled experimental conditions. Similar to previously performed OCR studies on *C. elegans*, our assays showed an increase of OCR from the L4 stage to adulthood, and a decreasing OCR from adulthood to old age. In a metabolic assay that used the mitochondrial uncoupling agent FCCP, respiration rates during *uncoupled respiration* increased by a factor of ≈ 2 , which is supported by our assay of metabolic heat production (see previous paragraph), and other available data of *C. elegans* OCR measurements. In the future, a multiplexed approach (as presented in section 1.3.2, for example) may be of interest for drug development applications. Specifically, the implementation of an array of separate culture chambers on the same chip, each containing an oxygen-sensitive indicator dye, would allow the testing of multiple compounds affecting mitochondrial functioning of the worms at the same time. This approach would require a system for parallelizing microfluidic manipulations as well as a robotic system to displace the

oxygen read-out system to the culture chamber of interest. Automated imaging of the worms would allow the acquisition of several additional phenotypes to analyze physiological traits and behaviour, *e.g.* size, feeding, fertility and motility.

Furthermore (Chapter 4), we developed a method for characterizing the mechanical properties *C. elegans* eggs using a custom force microscope. For the first time, we applied CFM to living embryos and demonstrated the possibility to detect alterations of the mechanical parameters of the eggshell caused by chemical treatments. Due to the large-range displacements and multi-scale force sensitivity, it was possible to record force-displacement curves of embryos until rupture of the eggshell. Using a numerical model, we were able to extract characteristic eggshell parameters from the experimental indentation curves. Chemical shell-altering treatments using bleach and chitinase were derived from standard procedures used in laboratory settings working with *C. elegans* populations. We concluded that even short bleach treatments have a strong impact on the mechanical properties of the embryonic eggshell. So far, it was only possible to analyze shell alterations qualitatively, *e.g.* by evaluating egg breakage rates by exiting the uterus or by observing the loss of the ovoid egg shape. In the future, this project might benefit from the use of microfabricated structures optimized for confining embryos or even living worms in fixed locations, which would enable automation of force-indentation experiments in order to achieve higher-throughput measurements. Fig. 5.1a shows a preliminary approach for trapping *C. elegans* embryos in circular SU-8 wells with diameters of $\approx 50 \mu\text{m}$. Embryos trapped in this way can be probed automatically using the CFM. A further application could be the mechanical characterization of adult nematodes confined in an open structure accessible by the micro-indenter tip (Fig. 5.1b). This device consists of a SU-8 groove on glass that accommodates an adult worm, as well as a separate chip containing etched and backgrounded array of Si strips that can be used to confine the worm in the groove.

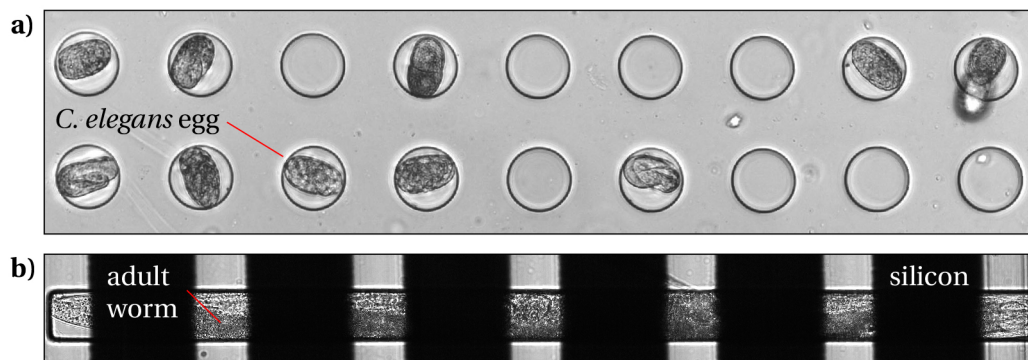


Figure 5.1 – Microtemplates for confining *C. elegans* embryos and worms. **a)** Bright-field microscope image of *C. elegans* embryos in circular wells. **b)** Bright-field microscope image of a *C. elegans* adult in a SU-8 groove, confined using an array of Si strips (black areas).

Chapter 5. Conclusion and outlook

In conclusion, we have developed microsystems to quantify phenotypes related to mitochondrial functioning and mechanical stability of *C. elegans* worms and embryos, respectively. Particularly interesting for future applications would be the combination of existing imaging-based phenotyping platforms with our approaches for assessing mitochondrial health based on metabolic heat or oxygen consumption rate measurements. Our oxygen sensing approach is especially suitable for the integration in a highly parallelized system. This method may possibly enable high-content drug screening assays using *C. elegans*, providing more holistic biological responses including mitochondrial functioning at a whole-organism level. This would be a significant improvement of the drug discovery pipeline, where compounds could be tested on *C. elegans* upstream of being tested on rodents. Evaluating the drug candidates in the worm model at initial and possibly more advanced stages of the drug development process eventually might diminish the requirement of drug testing on mice for instance, as selected lead compounds would have a higher chance of being efficient in more complex animals. Even if higher-order animal testing can probably not be completely avoided in the near future, the use of *C. elegans* as a promising alternative to mammalian models is not only beneficial from an economical point of view, but also from an ethical perspective.

A Appendix

Copyright licenses

This section contains copyright licenses for the reproduction of already published articles and figures that were adopted from published works.

Chapter 1

- **Figure 1.2:** Reprinted with permission from <https://www.wormatlas.org/>.
- **Figure 1.3:** WormBook content is licensed under a Creative Commons CC BY license.
Remarks: Information concerning ortholog number in the *C. elegans* genome was removed and the background color of the figure was changed to white.
- **Figure 1.6a:** The article containing the figure is licensed under a Creative Commons Attribution 4.0 International License.
- **Figure 1.6b:** The article containing the figure is licensed under a Creative Commons Attribution 4.0 International License.
- **Figure 1.6c:** License granted via RightsLink. License number: 4611320343270
Remarks: Reprinted from Lab on a Chip, Vol. 19, H.B. Atakan, M. Cornaglia, L. Mouchiroud, J. Auwerx, M.A.M. Gijs, Automated high-content phenotyping from the first larval stage till the onset of adulthood of the nematode *Caenorhabditis elegans*, p. 122, 2018, with permission from the Royal Society of Chemistry.

Chapter 2

- **Article:** The Royal Society of Chemistry (RSC) grants permission for the use of your paper in the printed version of your thesis.
Remarks: Reproduced by permission of The Royal Society of Chemistry. Link to the article: <https://pubs.rsc.org/en/content/articlehtml/2018/lc/c8lc00238j>

- **Figure 2.3:** License granted via RightsLink. License number: 4611241389927
Remarks: Reprinted from *Mechanisms of ageing and development*, Vol. 123, B.P. Braeckman, K. Houthoofd, A. De Vreese, J. R. Vanfleteren, Assaying metabolic activity in ageing *Caenorhabditis elegans*, p. 108, 2002, with permission from Elsevier.
- **Figure 2.4:** License granted via RightsLink. License number: 4611250513638
Remarks: Reprinted from *Experimental Gerontology*, Vol. 37, K. Houthoofd, B.P. Braeckman, I. Lenaerts, K. Brys, A. De Vreese, S. Van Eygen, J. R. Vanfleteren, Ageing is reversed, and metabolism is reset to young levels in recovering dauer larvae of *Caenorhabditis elegans*, p. 1018, 2002, with permission from Elsevier.

Chapter 3

- **Figure 3.3a:** License granted via RightsLink. License number: 4611251256471
Remarks: Reprinted from *Biochemical and Biophysical Research Communications*, Vol. 30, H. Suda, T. Shouyama, K. Yasuda, N. Ishii, Direct measurement of oxygen consumption rate on the nematode *Caenorhabditis elegans* by using an optical technique, p. 840, 2005, with permission from Elsevier.
- **Figure 3.3b:** The article containing the figure is licensed under a Creative Commons Attribution 4.0 International License.
- **Figure 3.4:** License granted via RightsLink. License number: 4611260252628
Remarks: Reprinted from *Nature Protocols*, Vol. 11, M. Koopman, H. Michels, B.M. Dancy, R. Kamble, L. Mouchiroud, J. Auwerx, E.A.A. Nollen, R.H. Houtkooper, A screening-based platform for the assessment of cellular respiration in *Caenorhabditis elegans*, p. 1803/1807, 2016, with permission from Springer.

Bibliography

- [1] Sydney Brenner. “Nature’s Gift to Science (Nobel Lecture)”. In: *ChemBioChem* 4.8 (2003), pp. 683–687.
- [2] S. Brenner. “The Genetics of CAENORHABDITIS ELEGANS”. In: *Genetics* 77.1 (1974), pp. 71–94.
- [3] Andrew Fire et al. “Potent and specific genetic interference by double-stranded RNA in *Caenorhabditis elegans*”. en. In: *Nature* 391.6669 (1998), pp. 806–811.
- [4] M. Chalfie et al. “Green fluorescent protein as a marker for gene expression”. en. In: *Science* 263.5148 (1994), pp. 802–805.
- [5] The C. elegans Sequencing Consortium*. “Genome Sequence of the Nematode C. elegans: A Platform for Investigating Biology”. en. In: *Science* 282.5396 (1998), pp. 2012–2018.
- [6] J. G. White et al. “The Structure of the Nervous System of the Nematode *Caenorhabditis elegans*”. en. In: *Philosophical Transactions of the Royal Society of London. Series B, Biological Sciences* 314.1165, (1986), pp. 1–340.
- [7] Lav R. Varshney et al. “Structural Properties of the *Caenorhabditis elegans* Neuronal Network”. en. In: *PLOS Computational Biology* 7.2 (2011), e1001066.
- [8] Maria Markaki and Nektarios Tavernarakis. “Modeling Human Diseases in *Caenorhabditis Elegans*”. eng. In: *Biotechnology Journal* 5.12 (2010), pp. 1261–1276.
- [9] E. L. Sonnhammer and R. Durbin. “Analysis of protein domain families in *Caenorhabditis elegans*”. eng. In: *Genomics* 46.2 (1997), pp. 200–216.
- [10] Adanna G. Alexander, Vanessa Marfil, and Chris Li. “Use of *Caenorhabditis elegans* as a model to study Alzheimer’s disease and other neurodegenerative diseases”. English. In: *Frontiers in Genetics* 5 (2014).
- [11] Xi Chen et al. “Using C. elegans to discover therapeutic compounds for ageing-associated neurodegenerative diseases”. In: *Chemistry Central Journal* 9 (2015).
- [12] Paul Fernyhough, Subir K. Roy Chowdhury, and Robert E. Schmidt. “Mitochondrial Stress and the Pathogenesis of Diabetic Neuropathy”. eng. In: *Expert Review of Endocrinology & Metabolism* 5.1 (2010), pp. 39–49.

Bibliography

- [13] I. L. Ferreira et al. "Multiple Defects in Energy Metabolism in Alzheimer's Disease". eng. In: *Current Drug Targets* 11.10 (2010), pp. 1193–1206.
- [14] Jun Ren et al. "Mitochondrial Biogenesis in the Metabolic Syndrome and Cardiovascular Disease". eng. In: *Journal of Molecular Medicine (Berlin, Germany)* 88.10 (2010), pp. 993–1001.
- [15] Tatiana R. Rosenstock, Ana I. Duarte, and A. Cristina Rego. "Mitochondrial-Associated Metabolic Changes and Neurodegeneration in Huntington's Disease - from Clinical Features to the Bench". eng. In: *Current Drug Targets* 11.10 (2010), pp. 1218–1236.
- [16] Richard Kones. "Parkinson's Disease: Mitochondrial Molecular Pathology, Inflammation, Statins, and Therapeutic Neuroprotective Nutrition". en. In: *Nutrition in Clinical Practice* 25.4 (2010), pp. 371–389.
- [17] Hibiki Kawamata and Giovanni Manfredi. "Mitochondrial Dysfunction and Intracellular Calcium Dysregulation in ALS". In: *Mechanisms of Ageing and Development. Mitochondria in Ageing* 131.7 (2010), pp. 517–526.
- [18] Scott B. Vafai and Vamsi K. Mootha. "Mitochondrial Disorders as Windows into an Ancient Organelle". eng. In: *Nature* 491.7424 (2012), pp. 374–383.
- [19] Titus Kaletta and Michael O. Hengartner. "Finding function in novel targets: *C. elegans* as a model organism". en. In: *Nature Reviews Drug Discovery* 5.5 (2006), nrd2031.
- [20] Linda P. O'Reilly et al. "C. elegans in high-throughput drug discovery". In: *Advanced Drug Delivery Reviews. Innovative tissue models for drug discovery and development* 69-70 (2014), pp. 247–253.
- [21] Li Dong et al. "Microfluidic Devices: Integrated Microfluidic Device for Drug Studies of Early C. Elegans Embryogenesis (Adv. Sci. 5/2018)". In: *Advanced Science* 5.5 (2018), p. 1870032.
- [22] Theresa Stiernagle. *Maintenance of C. elegans, WormBook*. 2016.
- [23] Z.F. Altun and D.H. Hall. "Introduction to C. elegans Anatomy". In: *WormAtlas* (2009).
- [24] Samuel Ward and John S. Carrel. "Fertilization and Sperm Competition in the nematode *Caenorhabditis Elegans*". In: *Developmental Biology* 73.2 (1979), pp. 304–321.
- [25] Andrew Jonathan Bretscher et al. "Temperature, Oxygen, and Salt-Sensing Neurons in C. Elegans Are Carbon Dioxide Sensors That Control Avoidance Behavior". In: *Neuron* 69.6-4 (2011), pp. 1099–1113.
- [26] Imre Vastrik et al. "Reactome: A Knowledge Base of Biologic Pathways and Processes". In: *Genome Biology* 8.3 (2007), R39.
- [27] Bart P. Braeckman. *Intermediary metabolism, WormBook*. 2009.
- [28] Joshua J. McElwee et al. "Diapause-Associated Metabolic Traits Reiterated in Long-Lived *Daf-2* Mutants in the Nematode *Caenorhabditis Elegans*". In: *Mechanisms of Ageing and Development* 127.5 (2006), pp. 458–472.
- [29] Jeremy M. Berg et al. *Biochemistry*. 5th. W H Freeman, 2002.

- [30] Verena Hirschberg, Tobias Fromme, and Martin Klingenspor. “Test Systems to Study the Structure and Function of Uncoupling Protein 1: A Critical Overview”. English. In: *Frontiers in Endocrinology* 2 (2011).
- [31] Agilent Technologies. *Seahorse XF Cell Mito Stress Test Kit*. Product Description. 2016.
- [32] Todd M. Squires and Stephen R. Quake. “Microfluidics: Fluid Physics at the Nanoliter Scale”. en. In: *Reviews of Modern Physics* 77.3 (2005), pp. 977–1026.
- [33] George M. Whitesides. “The Origins and the Future of Microfluidics”. En. In: *Nature* 442.7101 (2006), p. 368.
- [34] Henrik Bruus. *Theoretical Microfluidics*. Vol. 18. Oxford university press, 2008.
- [35] Eric K. Sackmann, Anna L. Fulton, and David J. Beebe. “The Present and Future Role of Microfluidics in Biomedical Research”. en. In: *Nature* 507.7491 (2014), pp. 181–189.
- [36] Nikos Chronis. “Worm Chips: Microtools for *C. Elegans* Biology”. eng. In: *Lab on a Chip* 10.4 (2010), pp. 432–437.
- [37] Matthew M. Crane et al. “Microfluidics-Enabled Phenotyping, Imaging, and Screening of Multicellular Organisms”. eng. In: *Lab on a Chip* 10.12 (2010), pp. 1509–1517.
- [38] Venkataragavalu Sivagnanam and Martin A. M. Gijs. “Exploring Living Multicellular Organisms, Organs, and Tissues Using Microfluidic Systems”. In: *Chemical Reviews* 113.5 (2013), pp. 3214–3247.
- [39] Natalia A. Bakhtina and Jan G. Korvink. “Microfluidic Laboratories for *C. Elegans* Enhance Fundamental Studies in Biology”. en. In: *RSC Advances* 4.9 (2013), pp. 4691–4709.
- [40] Matteo Cornaglia, Thomas Lehnert, and Martin A. M. Gijs. “Microfluidic Systems for High-Throughput and High-Content Screening Using the Nematode *Caenorhabditis Elegans*”. en. In: *Lab on a Chip* 17.22 (2017), pp. 3736–3759.
- [41] Maria Cristina Letizia et al. “Microfluidics-Enabled Phenotyping of a Whole Population of *C. Elegans* Worms over Their Embryonic and Post-Embryonic Development at Single-Organism Resolution”. En. In: *Microsystems & Nanoengineering* 4.1 (2018), p. 6.
- [42] Matteo Cornaglia et al. “An Automated Microfluidic Platform for *C. Elegans* Embryo Arraying, Phenotyping, and Long-Term Live Imaging”. en. In: *Scientific Reports* 5 (2015), p. 10192.
- [43] Huseyin Baris Atakan et al. “Automated High-Content Phenotyping from the First Larval Stage till the Onset of Adulthood of the Nematode *Caenorhabditis Elegans*”. en. In: *Lab on a Chip* 19.1 (2018), pp. 120–135.
- [44] Li Dong et al. “Versatile Size-Dependent Sorting of *C. Elegans* Nematodes and Embryos Using a Tunable Microfluidic Filter Structure”. en. In: *Lab on a Chip* 16.3 (2016), pp. 574–585.

Bibliography

- [45] Matthew A Churgin et al. “Longitudinal Imaging of *Caenorhabditis Elegans* in a Microfabricated Device Reveals Variation in Behavioral Decline during Aging”. In: *eLife* 6 (2017). Ed. by Piali Sengupta, e26652.
- [46] Li Dong et al. “Integrated Microfluidic Device for Drug Studies of Early *C. Elegans* Embryogenesis”. en. In: *Advanced Science* 5.5 (2018), p. 1700751.
- [47] Ingemar Wadsö. “Bio-calorimetry”. English. In: *Trends in Biotechnology* 4.2 (1986), pp. 45–51.
- [48] John E. Ladbury and Michael L. Doyle. *Bicalorimetry 2: Applications of Calorimetry in the Biological Sciences*. en. Google-Books-ID: WeWaVz8xraUC. John Wiley & Sons, 2004.
- [49] Jonathan B. Chaires. “Calorimetry and Thermodynamics in Drug Design”. en. In: *Annual Review of Biophysics* 37.1 (2008), pp. 135–151.
- [50] Olivier Braissant et al. “Use of isothermal microcalorimetry to monitor microbial activities”. en. In: *FEMS Microbiology Letters* 303.1 (2010), pp. 1–8.
- [51] Olivier Braissant et al. “Biomedical Use of Isothermal Microcalorimeters”. en. In: *Sensors* 10.10 (2010), pp. 9369–9383.
- [52] Laurent Dejean et al. “The calorimetric-respirometric ratio is an on-line marker of enthalpy efficiency of yeast cells growing on a non-fermentable carbon source”. In: *Biochimica et Biophysica Acta (BBA) - Bioenergetics* 1503.3 (2001), pp. 329–340.
- [53] B. Chance and G. R. Williams. “A simple and rapid assay of oxidative phosphorylation”. eng. In: *Nature* 175.4469 (1955), pp. 1120–1121.
- [54] Thomas Maskow et al. “What heat is telling us about microbial conversions in nature and technology: from chip- to megacalorimetry”. In: *Microbial biotechnology* 3.3 (2010), pp. 269–284.
- [55] Bruce Alberts et al. “Electron-Transport Chains and Their Proton Pumps”. In: *Molecular Biology of the Cell*. 4th edition. New York: Garland Science, 2002.
- [56] Leonard Guarente and Cynthia Kenyon. “Genetic pathways that regulate ageing in model organisms”. en. In: *Nature* 408.6809 (2000), pp. 255–262.
- [57] C. H. Lai et al. “Identification of novel human genes evolutionarily conserved in *Caenorhabditis elegans* by comparative proteomics”. eng. In: *Genome Research* 10.5 (2000), pp. 703–713.
- [58] Bart P Braeckman et al. “Assaying metabolic activity in ageing *Caenorhabditis elegans*”. In: *Mechanisms of Ageing and Development*. Genetic Effects on Aging III 123.2–3 (2002), pp. 105–119.
- [59] Koen Houthoofd et al. “Ageing is reversed, and metabolism is reset to young levels in recovering dauer larvae of *C. elegans*”. In: *Experimental Gerontology* 37.8–9 (2002), pp. 1015–1021.

- [60] R.B. Kemp. "Calorimetric Studies of Heat Flux in Animal Cells". en. In: *Thermochimica Acta* 193 (1991), pp. 253–267.
- [61] Thomas Maskow et al. "Potentials and limitations of miniaturized calorimeters for bioprocess monitoring". en. In: *Applied Microbiology and Biotechnology* 92.1 (2011), pp. 55–66.
- [62] Setaram Instrumentation. *C80 Calvet-Kalorimeter*. Product Description.
- [63] thermal hazard technology. *μRC Micro Reaction Calorimeter*. Product Description.
- [64] Stefan Mathias Sarge, Günther W. H. Höhne, and Wolfgang Hemminger. *Calorimetry: Fundamentals, Instrumentation and Applications*. en. John Wiley & Sons, 2014.
- [65] Texas Instruments. *Microcalorimetry: TAM IV & 48*. Product Description. 2015.
- [66] Ingemar Wadsö. "Isothermal Microcalorimetry in Applied Biology". In: *Thermochimica Acta*. Festschrift Dedicated to Dr. Richard B. Kemp on the Occasion of His 60th Birthday . Calorimetry : A Tool in Health and Environmental Studies . 394.1 (2002), pp. 305–311.
- [67] Johannes Lerchner, Thomas Maskow, and Gert Wolf. "Chip calorimetry and its use for biochemical and cell biological investigations". en. In: *Chemical Engineering and Processing: Process Intensification* 47.6 (2008), pp. 991–999.
- [68] Wonhee Lee, Jinyoung Lee, and Joonyoung Koh. "Development and applications of chip calorimeters as novel biosensors". en. In: *Nanobiosensors in Disease Diagnosis* (2012), pp. 17–29.
- [69] TA Instruments. *Microcalorimetry: TAM IV & 48*. 2015.
- [70] Symcel. *calScreener*. Product Description. 2019.
- [71] Olivier Braissant et al. "Isothermal microcalorimetry accurately detects bacteria, tumorous microtissues, and parasitic worms in a label-free well-plate assay". eng. In: *Biotechnology Journal* 10.3 (2015), pp. 460–468.
- [72] Suado M. Abdillahi et al. "Collagen VI Contains Multiple Host Defense Peptides with Potent In Vivo Activity". en. In: *The Journal of Immunology* 201.3 (2018), pp. 1007–1020.
- [73] Ingemar Wadsö et al. "A Well-Plate Format Isothermal Multi-Channel Microcalorimeter for Monitoring the Activity of Living Cells and Tissues". In: *Thermochimica Acta* 652 (2017), pp. 141–149.
- [74] S. Van Herwaarden. "Nano-Calorimetry". In: *Experimental Thermodynamics*. Ed. by K. N. Marsh and W. A. Wakeham A.R.H. Goodwin. Vol. 6. Measurement of the Thermodynamic Properties of Single Phases. Elsevier, 2003, pp. 368–385.
- [75] A.W. van Herwaarden. "Overview of calorimeter chips for various applications". en. In: *Thermochimica Acta* 432.2 (2005), pp. 192–201.
- [76] Francisco E. Torres et al. "Enthalpy arrays". In: *Proceedings of the National Academy of Sciences of the United States of America* 101.26 (2004), pp. 9517–9522.

Bibliography

- [77] E. B. Chancellor et al. "Heat conduction calorimeter for massively parallel high throughput measurements with picoliter sample volumes". In: *Applied Physics Letters* 85.12 (2004), pp. 2408–2410.
- [78] Rima Padovani et al. "Nanocalorimetric platform for accurate thermochemical studies in microliter volumes". en. In: *RSC Advances* 5.118 (2015), pp. 97133–97142.
- [79] Yuan Jia et al. "Isothermal titration calorimetry in a polymeric microdevice". en. In: *Microfluidics and Nanofluidics* 21.5 (2017), pp. 90–98.
- [80] M.K. Khaw, F. Mohd-Yasin, and N.T. Nguyen. "Microcalorimeter: Design considerations, materials and examples". en. In: *Microelectronic Engineering* (2016), pp. 107–117.
- [81] Shifeng Yu et al. "Review of MEMS differential scanning calorimetry for biomolecular study". en. In: *Frontiers of Mechanical Engineering* (2017), pp. 526–538.
- [82] Cindy Hany et al. "Thermal analysis of chemical reaction with a continuous microfluidic calorimeter". In: *Chemical Engineering Journal*. 10th International Conference on Microreaction Technology 160.3 (2010), pp. 814–822.
- [83] B. S. Kwak et al. "Dual thermopile integrated microfluidic calorimeter for biochemical thermodynamics". en. In: *Microfluidics and Nanofluidics* 5.2 (2007), pp. 255–262.
- [84] Wonhee Lee et al. "High-sensitivity microfluidic calorimeters for biological and chemical applications". en. In: *Proceedings of the National Academy of Sciences* 106.36 (2009), pp. 15225–15230.
- [85] J. Lerchner et al. "A New Micro-Fluid Chip Calorimeter for Biochemical Applications". en. In: *Thermochimica Acta* 445.2 (2006), pp. 144–150.
- [86] J. Lerchner et al. "Nano-calorimetry of small-sized biological samples". en. In: *Thermochimica Acta* 477.1-2 (2008), pp. 48–53.
- [87] J. Lerchner et al. "Miniaturized calorimetry — A new method for real-time biofilm activity analysis". en. In: *Journal of Microbiological Methods* 74.2-3 (2008), pp. 74–81.
- [88] F. Buchholz et al. "Chip Calorimetry for Fast and Reliable Evaluation of Bactericidal and Bacteriostatic Treatments of Biofilms". en. In: *Antimicrobial Agents and Chemotherapy* 54.1 (2010), pp. 312–319.
- [89] Frida Mariana et al. "Chip-Calorimetric Monitoring of Biofilm Eradication with Antibiotics Provides Mechanistic Information". In: *International Journal of Medical Microbiology* 303.3 (2013), pp. 158–165.
- [90] Frida Mariana Morais et al. "Chip-Calorimetric Monitoring of Biofilm Eradication with Bacteriophages Reveals an Unexpected Infection-Related Heat Profile". en. In: *Journal of Thermal Analysis and Calorimetry* 115.3 (2014), pp. 2203–2210.
- [91] T. Hartmann et al. "Thermopile chip based calorimeter for the study of aggregated biological samples in segmented flow". en. In: *Sensors and Actuators B: Chemical* 201 (2014), pp. 460–468.

- [92] A. Wolf et al. "Toward high-throughput chip calorimetry by use of segmented-flow technology". In: *Thermochimica Acta*. Chip Calorimetry 603 (2015), pp. 172–183.
- [93] Erik A. Johannessen et al. "Micromachined Nanocalorimetric Sensor for Ultra-Low-Volume Cell-Based Assays". In: *Analytical Chemistry* 74.9 (2002), pp. 2190–2197.
- [94] V. Baier et al. "Highly Sensitive Thermopile Heat Power Sensor for Micro-Fluid Calorimetry of Biochemical Processes". en. In: *Sensors and Actuators A: Physical* 123-124 (2005), pp. 354–359.
- [95] L. Wang et al. "A MEMS Thermal Biosensor for Metabolic Monitoring Applications". In: *Journal of Microelectromechanical Systems* 17.2 (2008), pp. 318–327.
- [96] T. J. Seebeck. "Ueber Die Magnetische Polarisation Der Metalle Und Erze Durch Temperaturdifferenz". en. In: *Annalen der Physik* 82.3 (1826), pp. 253–286.
- [97] E. Calvet and H. Prat. *Recent Progress in Microcalorimetry*. en. Elsevier, 1963.
- [98] Rima Padovani. "Thermal Microsensors for in Vitro and in Vivo Monitoring of Chemical and Biological Processes". PhD thesis. Lausanne: EPFL, 2016.
- [99] Sander Van Herwaarden. *Xensor Integration Liquid Nanocalorimeter Datasheet*. 2016.
- [100] R. F. Lama and Benjamin C.-Y. Lu. "Excess Thermodynamic Properties of Aqueous Alcohol Solutions." In: *Journal of Chemical & Engineering Data* 10.3 (1965), pp. 216–219.
- [101] Brad T. Moore, James M. Jordan, and L. Ryan Baugh. "WormSizer: High-throughput Analysis of Nematode Size and Shape". en. In: *PLOS ONE* 8.2 (2013), e57142.
- [102] William Y. Tsang and Bernard D. Lemire. "Mitochondrial Genome Content Is Regulated during Nematode Development". In: *Biochemical and Biophysical Research Communications* 291.1 (2002), pp. 8–16.
- [103] J. Lerchner et al. "Chip calorimeters for the investigation of liquid phase reactions: Design rules". In: *Thermochimica Acta*. Honour Issue on the Retirement of Prof. W. Hemminger 446.1 (2006), pp. 168–175.
- [104] David G. Nicholls et al. "Bioenergetic Profile Experiment using C2C12 Myoblast Cells". In: *Journal of Visualized Experiments : JoVE* 46.46 (2010), p. 2511.
- [105] Jin Zhang et al. "Measuring energy metabolism in cultured cells, including human pluripotent stem cells and differentiated cells". In: *Nature protocols* 7.6 (2012), pp. 1068–1085.
- [106] Mandy Koopman et al. "A screening-based platform for the assessment of cellular respiration in *Caenorhabditis elegans*". en. In: *Nature Protocols* 11.10 (2016), pp. 1798–1816.
- [107] Madhusudanarao Vuda and Ashwin Kamath. "Drug Induced Mitochondrial Dysfunction: Mechanisms and Adverse Clinical Consequences". In: *Mitochondrion* 31 (2016), pp. 63–74.

Bibliography

- [108] Martin D. Brand and David G. Nicholls. "Assessing Mitochondrial Dysfunction in Cells". In: *Biochemical Journal* 435.Pt 2 (2011), pp. 297–312.
- [109] Jenni Durieux, Suzanne Wolff, and Andrew Dillin. "The Cell-Non-Autonomous Nature of Electron Transport Chain-Mediated Longevity". In: *Cell* 144.1 (2011), pp. 79–91.
- [110] Virginija Jovaisaite, Laurent Mouchiroud, and Johan Auwerx. "The Mitochondrial Unfolded Protein Response, a Conserved Stress Response Pathway with Implications in Health and Disease". eng. In: *The Journal of Experimental Biology* 217.Pt 1 (2014), pp. 137–143.
- [111] Samantha M. Grist, Lukas Chrostowski, and Karen C. Cheung. "Optical Oxygen Sensors for Applications in Microfluidic Cell Culture". In: *Sensors (Basel, Switzerland)* 10.10 (2010), pp. 9286–9316.
- [112] L. C. Clark and C. Lyons. "Electrode Systems for Continuous Monitoring in Cardiovascular Surgery". eng. In: *Annals of the New York Academy of Sciences* 102 (1962), pp. 29–45.
- [113] Ching-Chou Wu et al. "Fabrication of Miniature Clark Oxygen Sensor Integrated with Microstructure". In: *Sensors and Actuators B: Chemical* 110.2 (2005), pp. 342–349.
- [114] S. Suresh, V. C. Srivastava, and I. M. Mishra. "Techniques for Oxygen Transfer Measurement in Bioreactors: A Review". en. In: *Journal of Chemical Technology & Biotechnology* 84.8 (2009), pp. 1091–1103.
- [115] Andrew Mills. "Optical Oxygen Sensors". en. In: *Platinum Metals Review* 41.3 (1997), pp. 115–127.
- [116] Paul Hartmann et al. "Oxygen Flux Fluorescence Lifetime Imaging". In: *Sensors and Actuators B: Chemical*. 3rd European Conference on Optical Chemical Sensors and Biosensors 38.1 (1997), pp. 110–115.
- [117] D. B. Papkovsky, T. O'Riordan, and A. Soini. "Phosphorescent Porphyrin Probes in Biosensors and Sensitive Bioassays". eng. In: *Biochemical Society Transactions* 28.2 (2000), pp. 74–77.
- [118] Otto Stern and Max Volmer. "Über Die Abklingungszeit Der Fluoreszenz". In: *Phys. Z.* 20 (1919), pp. 183–188.
- [119] I. Bergman. "Rapid-Response Atmospheric Oxygen Monitor Based on Fluorescence Quenching". En. In: *Nature* 218.5139 (1968), p. 396.
- [120] Mary-Ann Mycek, Brian W. Pogue, and Brian W. Pogue. *Handbook of Biomedical Fluorescence*. en. CRC Press, 2003.
- [121] Gregor Liebsch et al. "Luminescence Lifetime Imaging of Oxygen, pH, and Carbon Dioxide Distribution Using Optical Sensors". en. In: *Applied Spectroscopy* 54.4 (2000), pp. 548–559.
- [122] Joseph R. Lakowicz and Klaus W. Berndt. "Lifetime-selective Fluorescence Imaging Using an Rf Phase-sensitive Camera". In: *Review of Scientific Instruments* 62.7 (1991), pp. 1727–1734.

- [123] Agilent Technologies. *Seahorse XFe Analyzers*. Product Description. 2016.
- [124] Tara TeSlaa and Michael A. Teitell. “Techniques to Monitor Glycolysis”. In: *Methods in enzymology* 542 (2014), pp. 91–114.
- [125] Laurent Mouchiroud et al. “The NAD⁺/Sirtuin Pathway Modulates Longevity through Activation of Mitochondrial UPR and FOXO Signaling”. In: *Cell* 154.2 (2013), pp. 430–441.
- [126] Riekelt H. Houtkooper et al. “Mitonuclear Protein Imbalance as a Conserved Longevity Mechanism”. en. In: *Nature* 497.7450 (2013), pp. 451–457.
- [127] Pénélope A. Andreux et al. “A Method to Identify and Validate Mitochondrial Modulators Using Mammalian Cells and the Worm *C. Elegans*”. eng. In: *Scientific Reports* 4 (2014), p. 5285.
- [128] Norman Moullan et al. “Tetracyclines Disturb Mitochondrial Function across Eukaryotic Models: A Call for Caution in Biomedical Research”. In: *Cell Reports* 10.10 (2015), pp. 1681–1691.
- [129] Konstantinos Palikaras, Eirini Lionaki, and Nektarios Tavernarakis. “Coordination of Mitophagy and Mitochondrial Biogenesis during Ageing in *C. Elegans*”. en. In: *Nature* 521.7553 (2015), pp. 525–528.
- [130] Konstantinos Palikaras and Nektarios Tavernarakis. “Measuring Oxygen Consumption Rate in *Caenorhabditis Elegans*”. In: *Bio-protocol* 6.23 (2016).
- [131] Hitoshi Suda et al. “Direct Measurement of Oxygen Consumption Rate on the Nematode *Caenorhabditis Elegans* by Using an Optical Technique”. In: *Biochemical and Biophysical Research Communications* 330.3 (2005), pp. 839–843.
- [132] Shih-Hao Huang and Yu-Wei Lin. “Bioenergetic Health Assessment of a Single *Caenorhabditis Elegans* from Postembryonic Development to Aging Stages via Monitoring Changes in the Oxygen Consumption Rate within a Microfluidic Device”. en. In: *Sensors* 18.8 (2018), p. 2453.
- [133] Adriana San-Miguel and Hang Lu. “Microfluidics as a Tool for *C. Elegans* Research”. In: *WormBook* (2013), pp. 1–19.
- [134] Bhagwati P. Gupta and Pouya Rezai. “Microfluidic Approaches for Manipulating, Imaging, and Screening *C. Elegans*”. en. In: *Micromachines* 7.7 (2016), p. 123.
- [135] Muniesh Muthaiyan Shanmugam and Tuhin Subhra Santra. “Microfluidic Devices in Advanced *Caenorhabditis Elegans* Research”. eng. In: *Molecules (Basel, Switzerland)* 21.8 (2016).
- [136] Younan Xia and George M. Whitesides. “Soft Lithography”. In: *Annual Review of Materials Science* 28.1 (1998), pp. 153–184.
- [137] H. Yasuda and Kj Rosengren. “Isobaric Measurement of Gas Permeability of Polymers”. en. In: *Journal of Applied Polymer Science* 14.11 (1970), pp. 2839–2877.

Bibliography

- [138] K. S Houston, D. H Weinkauf, and F. F Stewart. "Gas Transport Characteristics of Plasma Treated Poly(Dimethylsiloxane) and Polyphosphazene Membrane Materials". In: *Journal of Membrane Science* 205.1 (2002), pp. 103–112.
- [139] Yutaka Amao. "Probes and Polymers for Optical Sensing of Oxygen". en. In: *Microchimica Acta* 143.1 (2003), pp. 1–12.
- [140] Christopher J. Ochs et al. "Oxygen Levels in Thermoplastic Microfluidic Devices during Cell Culture". In: *Lab on a chip* 14.3 (2014), pp. 459–462.
- [141] Kangning Ren, Jianhua Zhou, and Hongkai Wu. "Materials for Microfluidic Chip Fabrication". In: *Accounts of Chemical Research* 46.11 (2013), pp. 2396–2406.
- [142] Ostemers. *Ostemer 322 Crystal Clear*. Datasheet. 2018.
- [143] Che-Hsin Lin et al. "A Fast Prototyping Process for Fabrication of Microfluidic Systems on Soda-Lime Glass". en. In: *Journal of Micromechanics and Microengineering* 11.6 (2001), pp. 726–732.
- [144] Yuksel Temiz et al. "Lab-on-a-Chip Devices: How to Close and Plug the Lab?" In: *Microelectronic Engineering*. Micro and Nanofabrication Breakthroughs for Electronics, MEMS and Life Sciences 132 (2015), pp. 156–175.
- [145] Holger Becker and Claudia Gärtner. "Polymer Microfabrication Technologies for Microfluidic Systems". en. In: *Analytical and Bioanalytical Chemistry* 390.1 (2008), pp. 89–111.
- [146] David J. Guckenberger et al. "Micromilling: A Method for Ultra-Rapid Prototyping of Plastic Microfluidic Devices". In: *Lab on a chip* 15.11 (2015), pp. 2364–2378.
- [147] Charles E. Hoyle and Christopher N. Bowman. "Thiol–Ene Click Chemistry". en. In: *Angewandte Chemie International Edition* 49.9 (2010), pp. 1540–1573.
- [148] Carl Fredrik Carlborg et al. "Beyond PDMS: Off-Stoichiometry Thiol–Ene (OSTE) Based Soft Lithography for Rapid Prototyping of Microfluidic Devices". en. In: *Lab on a Chip* 11.18 (2011), pp. 3136–3147.
- [149] Josiane P. Lafleur et al. "Rapid Photochemical Surface Patterning of Proteins in Thiol–Ene Based Microfluidic Devices". en. In: *Analyst* 138.3 (2013), pp. 845–849.
- [150] Tommy Haraldsson, Carl Fredrik Carlborg, and Wouter van der Wijngaart. "OSTE: A New Material System for Labs-on-Chip". In: *Microfluidics, BioMEMS, and Medical Microsystems XII*. Vol. 8976. International Society for Optics and Photonics, 2014, p. 897608.
- [151] Carlos Errando-Herranz et al. "Biocompatibility of OSTE Polymers Studied by Cell Growth Experiments". eng. In: *The 17th International Conference on Miniaturized Systems for Chemistry and Life Sciences (MicroTAS 2013), Freiburg, 27-31 October 2013*. 2013.
- [152] Pyroscience Sensor Technology. *Piccolo2 Fiber-Optic Oxygen Meter*. User Manual 2.04.

- [153] Josef Ehgartner et al. "Online Analysis of Oxygen inside Silicon-Glass Microreactors with Integrated Optical Sensors". In: *Sensors and Actuators B: Chemical* 228 (2016), pp. 748–757.
- [154] Roger Krenger, Thomas Lehnert, and Martin A. M. Gijs. "Dynamic Microfluidic Nanocalorimetry System for Measuring *Caenorhabditis Elegans* Metabolic Heat". en. In: *Lab on a Chip* 18.11 (2018), pp. 1641–1651.
- [155] Drago Sticker et al. "Oxygen Management at the Microscale: A Functional Biochip Material with Long-Lasting and Tunable Oxygen Scavenging Properties for Cell Culture Applications". In: *ACS Applied Materials & Interfaces* 11.10 (2019), pp. 9730–9739.
- [156] Jo Anne Powell-Coffman. "Hypoxia Signaling and Resistance in *C. Elegans*". In: *Trends in Endocrinology & Metabolism* 21.7 (2010), pp. 435–440.
- [157] Scott F. Leiser et al. "Life-Span Extension From Hypoxia in *Caenorhabditis Elegans* Requires Both HIF-1 and DAF-16 and Is Antagonized by SKN-1". In: *The Journals of Gerontology Series A: Biological Sciences and Medical Sciences* 68.10 (2013), pp. 1135–1144.
- [158] Kfir Sharabi et al. "Elevated CO₂ Levels Affect Development, Motility, and Fertility and Extend Life Span in *Caenorhabditis Elegans*". en. In: *Proceedings of the National Academy of Sciences* 106.10 (2009), pp. 4024–4029.
- [159] C. R. Wilke and Pin Chang. "Correlation of Diffusion Coefficients in Dilute Solutions". en. In: *AIChE Journal* 1.2 (1955), pp. 264–270.
- [160] Daniel D. Shaye and Iva Greenwald. "OrthoList: A Compendium of *C. Elegans* Genes with Human Orthologs". en. In: *PLOS ONE* 6.5 (2011), e20085.
- [161] DevoWorm Group and Bradley J. Alicea. "The Emergent Connectome in *Caenorhabditis Elegans* Embryogenesis". en. In: *bioRxiv* (2018), p. 146035.
- [162] Pierre Gönczy. "Mechanisms of Asymmetric Cell Division: Flies and Worms Pave the Way". en. In: *Nature Reviews Molecular Cell Biology* 9.5 (2008), pp. 355–366.
- [163] Ana Carvalho et al. "Acute Drug Treatment in the Early *C. Elegans* Embryo". en. In: *PLOS ONE* 6.9 (2011), e24656.
- [164] Wendy L. Johnston and James W. Dennis. "The Eggshell in the *C. Elegans* Oocyte-to-Embryo Transition". en. In: *genesis* 50.4 (2012), pp. 333–349.
- [165] Kathryn K. Stein and Andy Golden. "The *C. Elegans* Eggshell". In: *WormBook, ed. The C. elegans Research Community* (2015), pp. 1–36.
- [166] Alan F. Bird and Jean Bird. *The Structure of Nematodes*. en. Academic Press, 1971.
- [167] David Wharton. "Nematode Egg-Shells". en. In: *Parasitology* 81.2 (1980), pp. 447–463.
- [168] Gaspare Benenati et al. "Two Cytochrome P450s in *Caenorhabditis Elegans* Are Essential for the Organization of Eggshell, Correct Execution of Meiosis and the Polarization of Embryo". In: *Mechanisms of Development* 126.5 (2009), pp. 382–393.

Bibliography

- [169] Sara K. Olson et al. “Hierarchical Assembly of the Eggshell and Permeability Barrier in *C. Elegans*”. en. In: *The Journal of Cell Biology* 198.4 (2012), pp. 731–748.
- [170] D. Felekis et al. “Quantifying Growth Mechanics of Living, Growing Plant Cells in Situ Using Microbotics”. In: *IET Micro Nano Letters* 6.5 (2011), pp. 311–316.
- [171] Alain Weber et al. “Measuring the Mechanical Properties of Plant Cells by Combining Micro-Indentation with Osmotic Treatments”. eng. In: *Journal of Experimental Botany* 66.11 (2015), pp. 3229–3241.
- [172] Judith Arfsten et al. “Atomic Force Microscopy Studies on the Nanomechanical Properties of *Saccharomyces Cerevisiae*”. In: *Colloids and Surfaces B: Biointerfaces* 79.1 (2010), pp. 284–290.
- [173] Yi Deng, Mingzhai Sun, and Joshua W. Shaevitz. “Direct Measurement of Cell Wall Stress Stiffening and Turgor Pressure in Live Bacterial Cells”. In: *Physical Review Letters* 107.15 (2011), p. 158101.
- [174] Francisco Moreno-Madrid et al. “Atomic Force Microscopy of Virus Shells”. eng. In: *Biochemical Society Transactions* 45.2 (2017), pp. 499–511.
- [175] Anne-Lise Routier-Kierzkowska et al. “Cellular Force Microscopy for in Vivo Measurements of Plant Tissue Mechanics”. en. In: *Plant Physiology* (2012), pp.111.191460.
- [176] Hannes Vogler et al. “The Pollen Tube: A Soft Shell with a Hard Core”. en. In: *The Plant Journal* 73.4 (2013), pp. 617–627.
- [177] Dimitrios Felekis et al. “Real-Time Automated Characterization of 3D Morphology and Mechanics of Developing Plant Cells”. en. In: *The International Journal of Robotics Research* 34.8 (2015), pp. 1136–1146.
- [178] Jan T. Burri et al. “Dual-Axis Cellular Force Microscope for Mechanical Characterization of Living Plant Cells”. In: IEEE, 2016, pp. 942–947.
- [179] Jan T. Burri et al. “Feeling the Force: How Pollen Tubes Deal with Obstacles”. en. In: *New Phytologist* 220.1 (2018), pp. 187–195.
- [180] J. T. Burri et al. “A Microrobotic System for Simultaneous Measurement of Turgor Pressure and Cell-Wall Elasticity of Individual Growing Plant Cells”. In: *IEEE Robotics and Automation Letters* 4.2 (2019), pp. 641–646.
- [181] Einhard Schierenberg and Bernd Junkersdorf. “The Role of Eggshell and Underlying Vitelline Membrane for Normal Pattern Formation in the Early *C. Elegans* Embryo”. eng. In: *Roux’s archives of developmental biology: the official organ of the EDBO* 202.1 (1992), pp. 10–16.
- [182] Chad A. Rappleye et al. “The Coronin-like Protein POD-1 Is Required for Anterior–Posterior Axis Formation and Cellular Architecture in the Nematode *Caenorhabditis Elegans*”. In: *Genes & Development* 13.21 (1999), pp. 2838–2851.
- [183] Yu Sun and Bradley J. Nelson. “MEMS Capacitive Force Sensors for Cellular and Flight Biomechanics”. eng. In: *Biomedical Materials (Bristol, England)* 2.1 (2007), S16–22.

- [184] Yu Sun et al. “Characterizing Fruit Fly Flight Behavior Using a Microforce Sensor with a New Comb-Drive Configuration”. en. In: *Journal of microelectromechanical systems* 14.1 (2005), pp. 4–11.
- [185] J. T. Burri et al. “Combining MEMS Force-Sensing and Microfluidics: Mechanical Characterization of Living Plant Cells”. In: *SystemsX Quantitative Network Biology*. Kandersteg, 2018.
- [186] Laura Bianchi and Monica Driscoll. *Culture of Embryonic C. Elegans Cells for Electrophysiological and Pharmacological Analyses*. en. WormBook, 2006.
- [187] William B. Wood. “Introduction to C. Elegans Biology”. In: *Cold Spring Harbor Monograph Archive* 17.0 (1988).
- [188] Sung-Jin Park, Miriam B. Goodman, and Beth L. Pruitt. “Analysis of Nematode Mechanics by Piezoresistive Displacement Clamp”. In: *Proceedings of the National Academy of Sciences of the United States of America* 104.44 (2007), pp. 17376–17381.
- [189] Joseph C. Doll et al. “SU-8 Force Sensing Pillar Arrays for Biological Measurements”. eng. In: *Lab on a Chip* 9.10 (2009), pp. 1449–1454.
- [190] Matilda Backholm, William S. Ryu, and Kari Dalnoki-Veress. “Viscoelastic Properties of the Nematode *Caenorhabditis Elegans*, a Self-Similar, Shear-Thinning Worm”. eng. In: *Proceedings of the National Academy of Sciences of the United States of America* 110.12 (2013), pp. 4528–4533.
- [191] L. A. Taber. “Large Deflection of a Fluid-Filled Spherical Shell Under a Point Load”. In: *Journal of Applied Mechanics* 49.1 (1982), pp. 121–128.
- [192] L. A. Taber. “Compression of Fluid-Filled Spherical Shells by Rigid Indenters”. In: *Journal of Applied Mechanics* 50.4a (1983), pp. 717–722.
- [193] Dominic Vella et al. “The Indentation of Pressurized Elastic Shells: From Polymeric Capsules to Yeast Cells”. en. In: *Journal of The Royal Society Interface* 9.68 (2012), pp. 448–455.
- [194] A. Lazarus, H. C. B. Florijn, and P. M. Reis. “Geometry-Induced Rigidity in Nonspherical Pressurized Elastic Shells”. In: *Physical Review Letters* 109.14 (2012), p. 144301.
- [195] Dominic Vella and Benny Davidovitch. “Indentation Metrology of Clamped, Ultra-Thin Elastic Sheets”. In: *Soft Matter* 13.11 (2017), pp. 2264–2278.
- [196] Hans Merzendorfer. “Insect Chitin Synthases: A Review”. eng. In: *Journal of Comparative Physiology. B, Biochemical, Systemic, and Environmental Physiology* 176.1 (2006), pp. 1–15.
- [197] Ali Miserez et al. “The Transition from Stiff to Compliant Materials in Squid Beaks”. In: *Science (New York, N.Y.)* 319.5871 (2008), pp. 1816–1819.
- [198] Takashi Nishino, Ryouusuke Matsui, and Katsuhiko Nakamae. “Elastic Modulus of the Crystalline Regions of Chitin and Chitosan”. en. In: *Journal of Polymer Science Part B: Polymer Physics* 37.11 (1999), pp. 1191–1196.

Bibliography

- [199] Shinsuke Ifuku and Hiroyuki Saimoto. “Chitin Nanofibers: Preparations, Modifications, and Applications”. en. In: *Nanoscale* 4.11 (2012), pp. 3308–3318.
- [200] Yinhua Zhang et al. “The Chitin Synthase Genes Chs-1 and Chs-2 Are Essential for *C. Elegans* Development and Responsible for Chitin Deposition in the Eggshell and Pharynx, Respectively”. eng. In: *Developmental Biology* 285.2 (2005), pp. 330–339.
- [201] Joshua N. Bembenek et al. “Cortical Granule Exocytosis in *C. Elegans* Is Regulated by Cell Cycle Components Including Separase”. en. In: *Development* 134.21 (2007), pp. 3837–3848.
- [202] Fabio Piano et al. “Gene Clustering Based on RNAi Phenotypes of Ovary-Enriched Genes in *C. Elegans*”. eng. In: *Current biology: CB* 12.22 (2002), pp. 1959–1964.
- [203] B. Sönnichsen et al. “Full-Genome RNAi Profiling of Early Embryogenesis in *Caenorhabditis Elegans*”. eng. In: *Nature* 434.7032 (2005), pp. 462–469.
- [204] Wendy L. Johnston, Aldis Krizus, and James W. Dennis. “Eggshell Chitin and Chitin-Interacting Proteins Prevent Polyspermy in *C. Elegans*”. eng. In: *Current biology: CB* 20.21 (2010), pp. 1932–1937.

Acronyms

2D	two-dimensional
3D	three-dimensional
acetyl-CoA	acetyl coenzyme A
ADP	adenosine diphosphate
AST	antimicrobial susceptibility testing
ATP	adenosine triphosphate
<i>C. elegans</i>	<i>Caenorhabditis elegans</i>
CFM	cellular force microscopy
CGC	Caenorhabditis Genetics Center
CL	chitin layer
CNC	computerized numerical control
CPGL	chondroitin proteoglycan layer
DI water	deionized water
DMSO	dimethyl sulfoxide
DO	dissolved oxygen
<i>E. coli</i>	<i>Escherichia coli</i>
ECAR	extracellular acidification rate
EPFL-ATPR	EPFL Atelier de l'Institut de microtechnique
EPFL-CMi	EPFL Center of MicroNanoTechnology
EPFL-SV-IN	EPFL Solution Preparation Facility
FADH ₂	flavin adenine dinucleotide
FCCP	carbonyl cyanide 4-(trifluoromethoxy)phenylhydrazone
FEM	finite element method
FPGA	field programmable gate array

Acronyms

GFP	green fluorescent protein
IMC	isothermal microcalorimetry
IPA	isopropyl alcohol
L1	larval stage 1
LED	light emitting diode
LOC	lab-on-a-chip
LOD	limit of detection
MEMS	microelectromechanical systems
mtDNA	mitochondrial deoxyribonucleic acid
N_3^-	azide
NADH	nicotinamide adenine dinucleotide
NBR	nitrile butadiene rubber
NGM	nematode growth medium
NIR	near infrared
OCR	oxygen consumption rate
OID	osmotic integrity defect
OSTE+	off-stoichiometry dual-cure thiol-ene-epoxy
OXPPOS	oxidative phosphorylation
PC	polycarbonate
PDMS	poly(dimethylsiloxane)
PET	polyethylene terephthalate
PGMEA	propylene glycol methyl ether acetate
PID	proportional-integral-derivative
PMMA	poly(methyl methacrylate)
PR	photoresist
RNA	ribonucleic acid
SD	standard deviation
SNR	signal-to-noise ratio

TCA	tricarboxylic acid
TEM	transmission electron microscopy
TMCS	trimethylchlorosilane
UPR ^{mt}	mitochondrial unfolded protein response
VL	vitelline layer
YA	young adult

Constants & Symbols

A	m^2	area
A_1	$cd*s$	acquisition window 1
A_2	$cd*s$	acquisition window 2
A_{TP}^M	1	V_{TP} peak area
D	m^2/s	diffusion coefficient
d_0	m	plate spacing
Δd	m	displacement of the sensing probe
Δ_l	m	elongation
Δ_l^{sim}	m	simulated elongation
ΔT	K	temperature difference
Δ_w	m	widening
Δ_w^{sim}	m	simulated widening
Δ_z	m	indentation distance
Δ_z^{punct}	m	maximal indentation depth
df	1	degrees of freedom
d	m	diameter
d_{1-3}	m	distance
Δt	s	time interval
E	N/m^2	Young's modulus
ϵ_0	F/m	permittivity of free space
ϵ_r	1	dielectric constant
E_{shell}	N/m^2	Young's modulus of the eggshell
η	m^2/s	dynamic viscosity
E_{visco}	N	viscoelastic energy loss
F_z	N	applied force in z direction
$F_z(\Delta_z)$	N	force indentation curve
F_z^{max}	N	maximal force of an $F_z(\Delta_z)$ curve after baseline correction
F_z^{punct}	N	shell puncturing force
F_z^{sim}	N	simulated applied force in z direction
$F_z^{sim}(\Delta_z, E_{shell})$	N/m^2	simulated indentation force surface
F_z^{thresh}	N	threshold force

Constants & Symbols

h	m	height
H_{exp}^M	J/mole	experimental molar mixing enthalpy
H_{lit}^M	J/mole	literature molar mixing enthalpy
I	cd	luminance intensity in presence of the quencher
I_0	cd	luminance intensity in absence of the quencher
$k(\Delta_z)$	N/m	effective eggshell stiffness
$k(F_z^{punct})$	N/m	effective stiffness at the shell puncture point
k_q	l/(mol*s)	quenching rate constant
λ	nm	wavelength of the light
l	m	length
n	1	number of values
cO_2	mol/l	oxygen concentration
ω	1/s	angular frequency
p	N/m ²	pressure
P	W	heat power
Pe	1	Peclet number
Φ	1	phase shift
p_{int}	N/m ²	interior pressure of the eggshell
p_{int}^{max}	N/m ²	maximal interior pressure of the eggshell at the shell puncture point
$p_{int}(\Delta_z, E_{shell})$	N/m ²	interior pressure surface
P_{pop}	W	metabolic heat power signal of an on-chip worm population
PS	V/W	heat power calibration factor
p	1	p -value
P_{vol}	W	normalized metabolic heat power per volume
$P_{vol/FCCP}$	W	absolute heat power per volume after FCCP treatment
P_{worm}	W	normalized metabolic heat power per worm
$P_{pop/FCCP}$	W	absolute heat power per worm population after FCCP treatment
$P_{worm/FCCP}$	W	absolute heat power per worm after FCCP treatment
Q	mol/s	oxygen diffusion rate
R^2	1	coefficient of determination
r	m	indenter radius
r_{ind}	m	indenter radius
Re	1	Reynolds number
ρ	kg/m ³	mass density
$\epsilon_{i,j}$	m	shell strain
$\sigma_{i,j}$	N/m ²	shell stress
S	1	sum of squares
t_1	s	time point 1
t_2	s	time point 2

τ	s	excited state lifetime in presence of the quencher
τ_0	s	excited state lifetime in absence of the quencher
t	m	thickness
V_{AC}	V	AC voltage
v_{mix}	nl/s	mixing flow rate
V_{out}	V	output voltage
V_{pop}	V	voltage signal of an on-chip worm population
ν_{shell}	1	Poisson's ratio of the eggshell
V_{TC}	V	thermocouple voltage
V_{TP}	V	thermopile voltage
w	m	width
X_{IPA}	1	mole fraction of IPA

Roger Krenger

Avenue de Milan 3
1007 Lausanne
+41 79 304 88 42
roger.krenger@gmail.com
Skype: rogerkrenger

LinkedIn:



STRENGTHS

- Specialist in microsystems with integrated MEMS sensors
- Strong interdisciplinary background

CAREER OBJECTIVES

I seek an opportunity for contributing my technological experience in the fields of microsystems and sensing applications in an international company.



EDUCATION

Ph.D. in Microsystems and Microelectronics

08/2015 - Present

Swiss Federal Institute of Technology (EPFL), Lausanne, Switzerland

M. Sc. in Nanosciences - Major in Physics

09/2012 - 09/2014

University of Basel, Switzerland

B. Sc. in Nanosciences

09/2009 - 07/2012

University of Basel, Switzerland

EXPERIENCE

Research Assistant and Engineer - Microsystems and Sensors

08/2015 - Present

Laboratory of Microsystems LMIS2, Swiss Federal Institute of Technology (EPFL), Lausanne, Switzerland

- Development of microengineered devices with integrated MEMS sensors for metabolic assays on biological model organisms
- Implementation of data processing algorithms and statistical analyses
- Teaching and mentoring of students
- Scientific writing and publishing in peer-reviewed journals, presenting at international conferences

Research Internships

09/2013 - 09/2014

C-CINA, Biozentrum, University of Basel, Switzerland

Quantum and Nanoelectronics Group, University of Basel, Switzerland

- Development of microfluidic, cantilever-based viscosity and mass density sensors
- Higher-mode analysis of microcantilevers vibrating close to a boundary in liquid
- Microfabrication of magnetic strips with physical vapor deposition using stencil lithography

TECHNICAL SKILLS

Microsystems & Engineering	<ul style="list-style-type: none">• Design, fabrication and testing of Lab on a Chip (LoC) devices in cleanroom facilities• Integration of MEMS sensors and nanoparticle-based oxygen sensing technology in benchtop and LoC devices• Application of MEMS-based and LoC devices in biological studies
Scientific Methods	<ul style="list-style-type: none">• Design, conduction and evaluation of scientific studies• Analysis, illustration and presentation of complex datasets• Scientific writing and publishing in peer-reviewed journals
Laboratory Equipment & Tools	<ul style="list-style-type: none">• Advanced: Microfluidics, MEMS sensors (thermopiles, microcantilevers and force sensors), luminescence-based oxygen sensors, cleanroom equipment• Basic: Microscopy (Optical, SEM, AFM), wet lab, cell culture, electronics
Software & Programming	<ul style="list-style-type: none">• Advanced: MATLAB, NI LabVIEW, GraphPad Prism, Adobe CC, MS Office• Basic: SolidWorks, COMSOL, Python, Arduino IDE, ImageJ
Project Management	<ul style="list-style-type: none">• PRINCE2 Foundation certification

SPOKEN LANGUAGES

German	Native language
English	Full professional working proficiency
French	Professional working proficiency

PERSONAL PROFILE

Biographical Sketch	Born on 12.02.1990 Swiss citizenship Completed military service Driver's license (B)
Leisure Activities	Marathon runner Amateur video- and photographer Passionate cook and baker

REFERENCES

Prof. Martin Gijs Thesis director	+41 21 693 6734 martin.gijs@epfl.ch
Dr. Thomas Lehnert Thesis co-director	+41 21 693 6605 thomas.lehnert@epfl.ch

- Journal Papers [R. Krenger](#), T. Lehnert and M. A. M. Gijs, “Dynamic microfluidic nanocalorimetry system for measuring *Caenorhabditis elegans* metabolic heat“, *Lab on a Chip*, 2018, 18, 1641-1651
DOI: 10.1039/C8LC00238J
- [R. Krenger](#), J. T. Burri, T. Lehnert, B. J. Nelson and M. A. M. Gijs, “Force microscopy of *Caenorhabditis elegans* eggs”, manuscript in revision (*Nature Microsystems & Nanoengineering*)
- [R. Krenger](#), T. Lehnert, T. Mayr, M. A. M. Gijs, “Microfluidic *Caenorhabditis elegans* culture with integrated real-time detection of its oxygen consumption rate”, manuscript in preparation
- B. A. Bircher, [R. Krenger](#), T. Braun, “Automated high-throughput viscosity and density sensor using nanomechanical resonators“, *Sensors and Actuators B: Chemical*, 2016, 223, 784-790
DOI: 10.1016/J.SNB.2015.09.084
- B. A. Bircher, [R. Krenger](#), T. Braun, “Influence of squeeze-film damping on higher-mode microcantilever vibrations in liquid”, *EPJ Techniques and Instrumentation*, 2014, 1
DOI: 10.1140/EPJTI/S40485-014-0010-6
- Conference Contributions [R. Krenger](#), J. T. Burri, T. Lehnert, B. J. Nelson and M. A. M. Gijs, “Biomechanical study of living *Caenorhabditis elegans* embryos using cellular force microscopy”, Proc. of 23rd International Conference on Miniaturized Systems for Chemistry and Life Sciences (microTAS 2019), Basel, Switzerland, October 2019
- G. Huszka, [R. Krenger](#), M. A. M. Gijs, “In vivo imaging with microsphere-based super-resolution microscopy”, International Conference on Optical MEMS and Nanophotonics (OMN), Lausanne, Switzerland, July 2018
- [R. Krenger](#), R. Trouillon, T. Lehnert and M. A. M. Gijs, “Microfluidic differential nanocalorimetry system for measurement of mixing enthalpy and cellular heat“, Proc. of 21th International Conference on Miniaturized Systems for Chemistry and Life Sciences (microTAS 2017), Savannah, Georgia, US, November 2017
- [R. Krenger](#), R. Padovani, T. Lehnert and M. A. M. Gijs, “Nanocalorimetric device for analysis of mixing enthalpy in microliter segmented flow plugs“, Proc. of 20th International Conference on Miniaturized Systems for Chemistry and Life Sciences (microTAS 2016), Dublin, Ireland, October 2016

